NASA CONTRACTOR REPORT

NASA CR-413

LINEAR AERODYNAMIC LOADS ON CONE-CYLINDERS AT MACH NUMBERS FROM 0.7 TO 2.0

by Roger Lee Hamner and Alan D. Leff

Prepared under Contract No. NAS 8-11289 *by*
LOCKHEED MISSILES & SPACE COMPANY
Huntsville, Ala.
for George C. Marshall Space Flight Center

NATIONAL AERONAUTICS AND SPACE ADMINISTRATION • WASHINGTON, D. C. • MARCH 1966

NASA CR-413

LINEAR AERODYNAMIC LOADS ON CONE-CYLINDERS AT MACH NUMBERS FROM 0.7 TO 2.0

By Roger Lee Hamner and Alan D. Leff

Prepared under Contract No. NAS 8-11289 by
LOCKHEED MISSILES & SPACE COMPANY
Huntsville, Ala.

for George C. Marshall Space Flight Center

NATIONAL AERONAUTICS AND SPACE ADMINISTRATION

For sale by the Clearinghouse for Federal Scientific and Technical Information
Springfield, Virginia 22151 – Price $1.25

FOREWORD

This report presents the results of work performed by Lockheed Missiles & Space Company, Huntsville Research & Engineering Center, under Contract NAS8-11289, "Determination and Presentation of Experimentally Derived Load Distributions for Cone Cylinder Configurations."

This work was done for the Marshall Space Flight Center Aero-Astrodynamics Laboratory by the Aero-Thermodynamics Section of the HREC Aero-Mechanics Department.

SUMMARY

Data collected from the literature have been analyzed in combination with results of a wind tunnel test program to provide linear aerodynamic load distributions for cone-cylinder configurations in the high subsonic, transonic and low supersonic Mach number regimes. Cone semi-vertex angles from 10° to 40°, Mach numbers from 0.7 to 2.0 and cylinder lengths up to 6.0 calibers are covered.

A comprehensive set of design curves is presented which will enable the designer to determine aerodynamic loads in a Mach number range where adequate methods have not been available. Pressure coefficient, local normal force slope, normal force and pitching moment buildup slopes for the segments of a cone-cylinder were developed on a parametric basis for the area of interest. Slopes were evaluated graphically using optimum linear curve fits between -4° and $+4^{\circ}$ angles-of-attack. Comparisons of C_{N_α} and C_{M_α} from force and pressure tests are made which show very favorable correlation. Since the results presented were obtained from the assimilation of data from many independent sources, the correlated curves are considered superior to each individual set of data.

Several flow characteristics which significantly influence the included aerodynamic design curves are noted. Large normal force gradients and surface pressure variations occur on and immediately aft of the nose cone, but decay to small values farther downstream. The boundary layer separation at the cone-cylinder juncture for some combinations of cone-angle and Mach number has a pronounced effect on the cylinder load distributions. A near normal shock occurring on the cylinder in transonic flow is accompanied by a sudden surface pressure rise.

Taylor-Maccoll, method-of-characteristics and Stone's theory predictions are compared with experimental values of pressure coefficient and local normal force coefficient slope distributions, demonstrating the consistency of the design curves with results outside the Mach number range considered.

CONTENTS

	Page
FOREWORD	iii
SUMMARY	v
SYMBOLS	ix
FIGURE INDEX	xi
INTRODUCTION	1
OBJECTIVES	3
METHOD OF APPROACH	5
DISCUSSION OF RESULTS	7
Cones	9
Cylinders	10
CONCLUSIONS	13
REFERENCES	15
FIGURES	17
APPENDIX - Carpet Plot Explanation	73

SYMBOLS

C_M	Pitching moment coefficient, $M/q_\infty SD$
C_{M_α}	Pitching moment coefficient slope, $\frac{\partial C_M}{\partial \alpha}$, per radian
C_N	Normal force coefficient, $F_N/q_\infty S$
C_{N_α}	Normal force coefficient slope, $\frac{\partial C_N}{\partial \alpha}$, per radian
$C_{\acute{N}}$	Local normal force coefficient, $\frac{\partial C_N}{\partial (x/D)}$, per caliber
$C_{\acute{N}_\alpha}$	Local normal force coefficient slope, $\frac{\partial C_{\acute{N}}}{\partial \alpha}$, per radian caliber
C_P	Pressure coefficient, $(P - P_\infty)/q_\infty$
D	Base (reference) diameter
F_N	Normal force
L	Segment length
M	Pitching moment about mrp
M_c	Critical Mach number
M_∞	Freestream Mach number
mrp	Moment reference point (see Figure 1)
P	Static pressure
q	Dynamic pressure, $\rho V^2/2$
R_N	Reynolds number, $\rho \frac{V}{\mu}$, per foot
S	Reference area, $\pi D^2/4$
V	Velocity
x	Distance downstream of segment leading edge
α	Angle of attack, degrees
θ	Cone semi-vertex angle, degrees

μ	Coefficient of absolute viscosity
ρ	Density
ϕ	Radial angle, radians

Subscripts

∞	Freestream
1	Cone segment
2	Cylinder segment

LIST OF FIGURES

Figure		Page
1	Configuration Sketch	17
2	The Influence of Cone Angle on Critical Flow Separation Mach Number	18
3	Variation of Cone Surface Pressure Distributions with Semi-Vertex Angle for Zero Angle-of-Attack	
	(a) M = 0.7	19
	(b) M = 0.8	20
	(c) M = 0.9	21
	(d) M = 0.95	22
	(e) M = 1.0	23
	(f) M = 1.1	24
	(g) M = 1.2	25
	(h) M = 1.5	26
	(i) M = 2.0	27
4	The Effect of Semi-Vertex Angle on Local Normal Force Slope Distributions for Cones	
	(a) M = 0.7	28
	(b) M = 0.8	29
	(c) M = 0.9	30
	(d) M = 0.95	31
	(e) M = 1.0	32
	(f) M = 1.1	33
	(g) M = 1.2	34
	(h) M = 1.5	35
	(i) M = 2.0	36
5	Variation of Cylinder Surface Pressure Distributions with Cone Angle for Cone-Cylinders at Zero Angle-of-Attack.	
	(a) M = 0.7	37
	(b) M = 0.8	38
	(c) M = 0.9	39
	(d) M = 0.95	40
	(e) M = 1.0	41

Figure		Page
5 (Cont'd)		
	(f) M = 1.1	42
	(g) M = 1.2	43
	(h) M = 1.5	44
	(i) M = 2.0	45
6	The Effect of Cone Angle on Cylinder Local Normal Force Slope Distributions for Cone-Cylinders	
	(a) M = 0.7	46
	(b) M = 0.8	47
	(c) M = 0.9	48
	(d) M = 0.95	49
	(e) M = 1.0	50
	(f) M = 1.1	51
	(g) M = 1.2	52
	(h) M = 1.5	53
	(i) M = 2.0	54
7	The Effect of Cone Angle on Cylinder Normal Force Slope Buildup for Cone-Cylinders	
	(a) M = 0.7	55
	(b) M = 0.8	56
	(c) M = 0.9	57
	(d) M = 0.95	58
	(e) M = 1.0	59
	(f) M = 1.1	60
	(g) M = 1.2	61
	(h) M = 1.5	62
	(i) M = 2.0	63
8	The Effect of Cone Angle on Cylinder Pitching Moment Slope Buildup for Cone-Cylinders	
	(a) M = 0.7	64
	(b) M = 0.8	65
	(c) M = 0.9	66
	(d) M = 0.95	67
	(e) M = 1.0	68
	(f) M = 1.1	69
	(g) M = 1.2	70
	(h) M = 1.5	71
	(i) M = 2.0	72

INTRODUCTION

Large multi-stage vehicles commonly encounter critical aerodynamic loads during flight in the transonic flow regime. It is in this Mach number range that velocities are sufficiently high, yet altitudes are low enough that high dynamic pressures and maximum loads usually occur.

Generally, the analysis of transonic flow around composite bodies is a complex problem due to such phenomena as: (1) the unsteady nature of the flow, (2) an intricate system of near normal shock waves, (3) flow separation, and (4) the nonlinear character of loads with attitude changes. For this reason, the prediction of aerodynamic loads for Mach numbers near one has not been amenable to theoretical methods except in special cases.

The normal approach to transonic aerodynamic design problems has been to rely on wind tunnel test results. Consequently, a great deal of experimental aerodynamic information for transonic Mach numbers has been obtained over the years. For the most part, however, these data are for specific models under specific conditions and are useful only to the procurer. Research studies where appropriate parameters have been systematically varied are few and limited.

Since theoretical analyses are inadequate and experimental data are not readily available, the aerodynamic designer is faced with the task of predicting design loads for vehicles in an area where means are acutely lacking. It is highly desirable then, that design curves for basic shapes be available to the aerodynamicist to assist him in evaluating transonic aerodynamic loads on these bodies as well as for more complicated shapes. Establishment of a set of such curves is the purpose of the present study. Earlier attempts were made to construct design curves for cone-cylinder-frustum-cylinder shapes using test results collected from various references listed in References 1 and 2. A significant quantity of information was obtained and limited design curves constructed and published in Reference 3. The lack of data in certain areas plus the irregular spacing of points for a given parameter made it difficult to establish a comprehensively valid set of curves as intended.

The present study has been conducted to establish aerodynamic loads for cone-cylinder configurations in the high subsonic, transonic, and low supersonic (i.e., "trisonic") Mach number range. A series of force and pressure tests was conducted in the Marshall Space Flight Center 14-inch Trisonic Wind Tunnel to complement data available from the literature. Results of these tests were published in References 4 and 5.

By combining results from the above mentioned tests with pertinent data from various references, experimental design curves have been developed parametrically over a wide range of geometric and flow parameters. It is not the intent of the authors to advance the notion that these curves completely solve the trisonic aerodynamic problem for cone-cylinders. Several aspects of the topic such as unsteady (oscillating) flow, Reynolds number effects on flow separation, hysteresis effects, shock location, and nonlinear loads are not investigated here. Even though the solution submitted in this report is somewhat simplified, it can accurately predict loads for the majority of cases for cone-cylinders and may serve as a basis for more refined analyses.

OBJECTIVES

The purpose of the current study has been to define the trisonic aerodynamic loads for cone-cylinder configurations on a parametric basis. These loads include:

1. Pressure distributions at zero angle-of-attack
2. Local normal force slopes
3. Normal force slope buildups
4. Pitching moment slope buildups

Design curves were to be established in coefficient form.

Parameters which may have a significant effect upon these loads are:

1. Cone Angle: The semi-vertex angle, θ, is normally considered to be descriptive and will be used here. This is the most significant of the geometric parameters affecting loads on the cone and on the shoulder of the cylinder, as well as the overall flow field. Effects of θ varying from 10^{o} to 40^{o} are determined. (Geometric variables are shown in the model sketch, Figure 1.)

2. Cone-Axial Coordinate: Pressure and local normal force distributions for cones are necessarily described as being dependent upon axial distance, x, from its vertex. For convenience, it is non-dimensionalized by the cone length, L_1. x/L_1 will then assume values between 0 and 1.0.

3. Cylinder Length: Carryover loads and pressure variations are normally quite large near the cone-cylinder juncture, decaying to small values farther downstream. A near normal shock or system of shocks may occur on the cylinder which influences loads downstream of the shocks. The cylinder length or distance downstream of the juncture in calibers, x/D is used in describing axial variations up to a maximum value of 6.0.

4. Angle-of-Attack: For evaluating coefficient slopes, no data were observed for pitch angles greater than 10^{o}. Loading tends to be sharply nonlinear at steeper angles. Concern here is for the approximation of that portion of a coefficient versus α curve between $+4^{o}$ and -4^{o} angles-of-attack by a straight line.

5. Mach Number: To adequately cover the range where theoretical means are invalid, Mach numbers from 0.7 to 2.0 are considered.

6. Reynolds Number: For data used in this study, several sources are involved and the operating unit Reynolds numbers of each is merely accepted at face value. These are on the order of 3 to 10 x 10^{6} per foot. The influence of varying Reynolds number is, therefore, not investigated. However, the Reynolds number was sufficiently high such that a turbulent boundary existed near the cone-cylinder juncture in most cases.

7. Transient Flow: Unsteady phenomena such as shock oscillations, alternating boundary layer separation and attachment, aeroelastic flutter, hysteresis, and time lag responses are likely to occur under certain conditions. These flow properties are so complex as to be beyond the scope of this study.

It was planned that the results of the present study were to be based on wind tunnel test data. The test program conducted in conjunction with the project was designed to complement existing experimental results in providing a continuous spectrum of data for significant parameters.

It is important that design curves developed during this study be consistent with other results outside the Mach number range covered here. The most direct means of assuring such consistency is to show favorable comparisons with acceptable theories.

METHOD OF APPROACH

The data utilized in defining design curves for this study are from several sources, some being tabulated in reports and others being available on data cards. It was necessary to keypunch those tabulations, and perform a card format conversion for other data to permit processing with the appropriate programs. Basically, the procedure was to obtain body forces by the integration of surface pressure distributions over cone-cylinders for an angle-of-attack range. Angle-of-attack slopes could then be determined for coefficients of the forces. The correlation and presentation achieved was based on results in coefficient and coefficient slope form.

For a parametric study, the ideal method of data presentation appears to be the use of "carpet" plots. The aerodynamic loading curves are presented in this fashion. This graphical method is also useful in correlating results. A brief explanation of carpet plots is contained in Appendix A for the benefit of readers who may not be familiar with their use.

Where radial distributions were available, local normal forces were obtained by numerically integrating pressures around the body. A fifth degree polynomial curve fit of C_p was performed by computer to permit this procedure as described in detail by Reference 6.

For pressure distributions given at top and bottom centerlines only, Reference 7, an approximation scheme was programmed to estimate local normal forces from incremental pressures. The relation

$$\int_0^{\pi/2} \Delta C_p \, d(\sin\theta) \simeq K \; \Delta C_{p_{max}}$$

was used where $\Delta C_p = C_p(\text{lower}) - C_p(\text{upper})$ and $\Delta C_{p_{max}} = C_p|_{\phi=\pi} - C_p|_{\phi=0}$. K was determined experimentally to be $K \simeq 0.8$ from cases where radial distributions were provided. It may be noted that a cosine distribution yields $K = \pi/4$.

Coefficient slopes were evaluated graphically from angle-of-attack plots. Points for angles-of-attack up to 10^o were plotted and used in

defining each faired curve. The slope of a straight line which best approximates each curve between $\alpha = -4^{o}$ and $\alpha = +4^{o}$ was taken as the desired slope value.

Carpet plots of C_{N_α}' versus cone angle and axial coordinates for fixed values of Mach number were constructed. Correlation was accomplished by observing overall trends and cross-fairing of the data.

Separate sets of curves were constructed for both cones and cylinders. In this manner, the coordinates of cones would be made the same for all cone angles (in percent of total length) and cylinder axial distances are identical. In order for the integral of the C_{N_α}' distribution curve for a cone to represent the normal force slope, the curve must be integrated as a function of x/D rather than x/L_1 as presented (the local normal force coefficient value is in units of per caliber).

The trapezoidal rule was used to integrate local normal force slopes to obtain normal force and pitching moment slope buildups. Inputs to this integration routine were taken sufficiently close together to yield a good approximation of the area under each curve. These integrated buildups can then be compared directly with normal force and pitching moment slopes obtained from force tests.

Local normal force slopes from method-of-characteristics theory were provided by the Aero-Astrodynamics Laboratory of NASA/MSFC.

DISCUSSION OF RESULTS

Design curves have been developed from experimental results and are presented in Figures 3 through 8 from which linear aerodynamic loads for cone-cylinders may readily be assessed. To better understand the behavior of these curves, it will be well to first discuss some observed properties of transonic flow over configurations of this type.

It is well established that in transonic flow the boundary layer separates at the juncture of a cone-cylinder configuration for some cases and remains attached for others. Robertson and Chevalier discuss this observation in Reference 8. Whether the flow separates at the cylinder shoulder depends upon the cone-angle, Mach number, model attitude, and possibly other factors.

For zero angle-of-attack and fixed cone angle, there is an approximate critical Mach number above which flow is attached and below which the boundary layer separates at the juncture. Very close to this critical Mach number, alternating flow attachment and separation may occur, but such a phenomenon has not been explored in the present study. Reynolds number variations may have considerable effect upon the critical Mach number. However, this also is a problem worthy of a separate investigation and is not explored here.

The critical Mach number seems to follow a definite pattern, obviously depending on Mach number and cone angle from test results available. Several sets of pressure distributions indicate two distinct and opposite (one attached, the other separated) cases where Mach number and cone angle are identical. Where this occurs, that Mach number is interpreted to be critical for that cone angle. The cause of this apparent ambiguity is not defined. Possibly, it is a Reynolds number effect, a slight difference in cone-angle or Mach number, disturbances in the test section flow or even the influence of some other parameter not considered. Pressure distributions for other Mach numbers confirm that the flow is separated at lower Mach numbers and attached for high Mach numbers. (Conversely, a critical cone angle may be defined for fixed Mach number, whereby the flow is separated for higher cone angles and is attached for lower cone angles.)

Curves depicting the critical Mach number as a function of cone angle are shown in Figure 2. The curve representing the present study was obtained primarily from data acquired in the MSFC 14-inch Trisonic Tunnel (Reference 4) operating at Reynolds numbers (D = 1.75") from 5.3×10^6 to 6.8×10^6 and the Convair High-Speed Tunnel (Reference 9) operating at Reynolds number (D = 3.48") from 8×10^6 to 9×10^6 per foot. No boundary layer trip was used in either test. These curves will be useful in describing the discontinuities which appear in subsequent design curves.

The curve from Reference 8 was obtained by reading critical Mach number from the discontinuities of pressure coefficient for an orifice (located on the cylinder near the juncture) shown as a function of freestream Mach number. This test was conducted in the AEDC Trisonic Model Tunnel at Reynolds numbers from 4×10^6 to 5×10^6 for a 1.0 inch diameter model with no trip. Reference 8 also shows results with various boundary layer trips on the cone surfaces which indicate significant changes in the critical Mach number in the direction of the present study curve. Thus, a Reynolds number effect would appear to be present which could explain the differences in the curves at smaller angles.

Model pitch angle does have some effect upon boundary layer separation, but the basic flow behavior is similar to the $\alpha = 0$ case. On the windward side of the body, flow separation is retarded by a positive pitch angle while the opposite effect is seen on the leeward side. Since a radical pressure change accompanies flow separation, the unsymmetrical flow pattern produces large changes in the normal force distribution from the attached flow case.

Another flow characteristic worthy of mention at this point is the near normal shock occurring on the cylinder. This is discussed in detail in Reference 8 and curves of shock location varying with cone angle and Mach number are presented.

It has been convenient to consider each segment separately in correlating and presenting the results. Thus, the pressure coefficient and local normal force slope plots are broken down according to segments, with cone distributions being shown first. Normal force and pitching moment slope buildup curves begin at the leading edge of the cylinder as cone values, precluding the necessity of individual cone coefficient buildup plots.

Cones

The variation of cone surface pressure coefficient at zero angle-of-attack with cone angle and non-dimensionalized axial station for several Mach numbers is presented in Figure 3. The correlation shown was obtained by combining experimental results from References 5, 7, 9, 10, and 11.

For Mach numbers of one or less, pressures are high near the cone vertex and taper off to low values downstream, a trend typical of subsonic flow around cones. This type of distribution is expected since the flow over a cone is completely subsonic for these Mach numbers. The same trend is present for supersonic freestream Mach numbers where the cone surface Mach number is subsonic, particularly where the shock is unattached.

It is evident that the pressure distribution curves flatten out to a near constant value when flow around the cone becomes supersonic, as predicted by Taylor-Maccoll theory. Theoretical distributions from Reference 12 (Taylor-Maccoll) are indicated on graphs representing supersonic Mach numbers for cone angles at which a solution exists, i. e., the attached shock case. The agreement is good for cases where conical flow is supersonic. Where flow over the cone is subsonic, the low pressure downstream of the shoulder has a significant effect on the aft portion of the surface pressure distributions. Since this effect is not accounted for theoretically (a semi-infinite cone is assumed) discrepancies in this area are noted.

Figure 4 shows the effect of cone angle and Mach number on cone local normal force coefficient slope distributions. The experimental points indicated were derived from data obtained from References 5, 7, 9, and 10. Even the subsonic distributions are almost linear, but near the juncture the curves taper off, similar to the C_p curves, particularly for the steeper cone angles. For supersonic Mach numbers, Stone's theory from Reference 12 is compared with experimental curves for existing solutions. The comparisons are very good for most cone angles and Mach numbers except near the junctures where C_{N_α}' tends to diminish. For those cases where flow around the cone is subsonic, approaching the limit of the theory, agreement is poor.

Cylinders

Cylinder surface pressure distributions for zero angle-of-attack are depicted in Figure 5. Experimental pressure coefficient data were taken from References 5, 7, 8, 9, 10, and 13. With a few exceptions, the correlation of these data is very good, especially since these results represent tests conducted in several facilities.

The zero point on each distribution curve is coincident with the cone-cylinder juncture. Flow expanding around this corner produces a very low pressure immediately aft of the juncture, and farther downstream the pressure tends to decay back to freestream values. The most obvious feature of these plots is the discontinuity of constant station curves caused by boundary layer separation at the cone-cylinder juncture. The characteristic shapes of the pressure distribution curves for the separated and attached flows are different. The discontinuity can be predicted by referring back to Figure 2.

Another characteristic for attached flow cases for Mach numbers of 1.0 and less is the sudden pressure rise associated with the near normal shock on the cylinder. The shock locations for Mach numbers of 0.9, 0.95 and 1.0 from Reference 6 for 1.0 inch diameter models are indicated. The data from that reference show that the sudden pressure rise is coincident with the shock. The scatter in data points for Mach 1.0 and 1.1 is probably caused by variations in the near normal shock wave due to tunnel wall effects.

The effect of cone angle on cylinder local normal force coefficient slope distribution is indicated in Figure 6. These slopes were evaluated from integrated pressure distribution data from References 5, 7, 9, 10, 13, and 14.

For subsonic Mach numbers, $C_{N_\alpha}{}'$ is negative on the shoulder immediately aft of the junction, increasing to large positive values at about one caliber and then decaying to small values farther downstream. As Mach number is increased, the tendency is for the large negative local normal force near the shoulder to decrease and the downstream $C_{N_\alpha}{}'$ to change to negative values.

The discontinuity caused by flow separation is again apparent in Figure 6 for Mach numbers 0.9, 0.95, and 1.0, following the same pattern evidenced in C_p curves. For the attached case, the surface pressure near the junctures would be more sensitive to slight angle-of-attack changes, causing larger local normal forces than those occurring with separated flow.

In Figure 6B (M = 0.8), a discontinuity not shown may occur at the 20^o curve as indicated in Figure 2. If so, there are not sufficient data in that area to define it. The interpolated curve shown for 20^o compares well with force results when integrated, indicating that the suggested discontinuity, if it exists, is not pronounced. Constant station curves are therefore faired in smoothly for the full range of θ.

At M = 0.9, the 30^o curve is probably exaggerated due to unsymmetrical flow separation. Even at small pitch angles, the boundary layer is separated on the leeward side and attached on the windward side which causes a large unbalance of pressures in the downward direction very close to the juncture. The 15^o and 20^o curves exhibit abrupt dips at x/D of about 0.5, probably caused by the near normal shocks located near that station. No other similar cases occur where flow is attached because shock locations are in an area where C_{N_α}' values are small enough that any shock effect does not significantly affect data points shown. For separated flow, either no such well defined shocks exist or their effect is diffused in the separated region.

Method-of-characteristics C_{N_α}' distributions are shown for 10, 15, and 20^o curves at Mach 1.5 and 2.0. These compare quite well with experimental values for the first 1.5 to 2.0 calibers downstream of the juncture. The method-of-characteristics predictions tend to diverge below experimental points farther downstream. It is possible that the nonlinearity of C_{N_α}' versus α curves may account for indicated differences. A linear curve fit over the α range of $\pm 4^o$ determines experimental slopes while theoretical values are calculated at $\alpha = 0$.

The integrated normal force and pitching moment coefficient buildups are presented in Figures 7 and 8, respectively. No experimental data points for pressure results are shown since these were, for the most part, obtained from a numerical integration of the correlated C_{N_α}' curves. The cone values

(x/D = 0) for C_{N_α} and C_{M_α} (flagged solid symbols) were obtained from Reference 3, these configurations being simple cones without cylindrical afterbodies. The other solid symbols represent force test coefficient slopes for 2.5 and 5.0 caliber length cylindrical afterbodies from Reference 4. In some instances, pressure distributions (and hence C_{N_α}' distributions) are only defined for the first 2.0 to 3.0 calibers. For those, the C_{N_α} and C_{M_α} curves were extended to 6.0, their shapes being based on adjacent curves and force data. Care was taken that C_{N_α}', C_{N_α} and C_{M_α} curves were compatible in all cases.

The force and integrated pressure results appear to match very well from an overall viewpoint. Integrated pressure data are particularly close to force test results for pure cones and cone-cylinders with 2.5 caliber cylinder lengths. The larger discrepanices are for the 5.0 caliber cylinders.

An exception is the 40° cone-cylinder at M = 0.95, which shows a marked difference between force and pressure results. During the pressure test, the boundary layer was separated at the leading edge of the cylinder. Separation effects on cylinder C_p and C_{N_α}' distributions derived from pressure data can be observed in Figures 4d and 6d. The C_{N_α}' and C_{M_α}' values from force test data for the 40° cone line up very well with data for other cone angles verifying that flow was attached in that case. For a cone angle of 40°, the critical Mach number for flow separation is $M_c = 0.95$ (Figure 2). The discrepancy observed is attributed to flow attachment during the force test and separation in the pressure test.

CONCLUSIONS

From the results included herein, the following conclusions have been made:

1. The aerodynamic loading design curves presented show good comparisons of force and pressure data and hence, are a reliable source of aerodynamic loads information.

2. Method-of-characteristics, Taylor-Maccoll and Stone's theories generally compare favorably with experimental results in their range of validity which indicates that these design curves are compatible with other results outside the Mach number range included here.

3. Large normal force gradients and surface pressure variations occur on and near the nose, decaying to small values farther downstream.

4. Boundary layer separation at the cone-cylinder juncture follows a definite pattern in the Mach number range just below 1.0 being dependent on cone angle, Mach number, and possibly other factors. A critical Mach number, M_c, can be defined for a given cone angle for which the flow is attached at higher Mach numbers and separated at lower Mach numbers. Two curves showing M_c as a function of cone angle for the included test results are shown. Flow separation at the juncture has a radical effect on the aerodynamic loads on the cylinder.

5. A near normal shock, which may occur transonically on the cylinder when the flow remains attached, is accompanied by a sudden surface pressure rise in its vicinity.

Since the results presented in this report were obtained from the assimilation of data from many independent sources, the correlated curves are considered to be much more reliable than each individual set of data. First, the large volume of data involved was applied over a broad area requiring continuity of results over the range of each parameter. Second, the method of correlation permitted the advantage of two parametric variations simultaneously.

A comprehensive set of aerodynamic loads design curves for cone-cylinder configurations have been developed and documented herein. These curves will enable the designer to ascertain the aerodynamic load distributions and total loads for cones and cone-cylinders for any configuration within a broad range of geometric parameters in a Mach number range where adequate methods were previously unavailable. Certainly, there are refinements which could be made to the present analysis as well as related areas of endeavor. Among these are hysteresis effects, non-linearities (cross-flow), Reynolds numbers effects, shock oscillations and critical Mach number (or cone angle), any of which may be investigated in further detail. It is intended that in subsequent studies such as those suggested above, the present results might be used as a starting point for establishing a course of study.

REFERENCES

1. Hamner, Roger L., A Report Bibliography for the Trisonic Aerodynamics of Cone-Cylinder-Flare-Cylinder Type Bodies, LMSC/HREC AO33441, Lockheed Missiles and Space Company, Huntsville Research & Engineering Center, Huntsville, Alabama, 19 February 1964.

2. Evans, George R., Aerodynamic Characteristics of Bodies of Revolution Without Fins: An Annotated Bibliography, Report 8-4-63-13, Lockheed Missiles & Space Company, Sunnyvale, California, July 1963.

3. Benefield, J. W., R. L. Hamner, R. J. Hauser and A. D. Leff, A Correlation of Transonic and Supersonic Aerodynamic Characteristics for Cones, Cylinders and Flares, TM 54/01-42, Lockheed Missiles & Space Company, Huntsville Research & Engineering Center, Huntsville, Alabama, 30 January 1964, CONFIDENTIAL.

4. Hauser, R. J., Experimental Investigation of the Static Stability Characteristics of a Family of Cone-Cylinder Configurations at Mach Numbers from 0.7 to 2.0, TM 54/20-4, Lockheed Missiles & Space Company, Huntsville Research & Engineering Center, Huntsville, Alabama, (to be published).

5. Hauser, R. J., Experimental Pressure and Normal Force Distribution Data for a Family of Cone-Cylinder Configurations at Test Mach Numbers from 0.7 to 2.0, TM 54/20-5, Lockheed Missiles & Space Company, Huntsville Research & Engineering Center, Huntsville, Alabama, (to be published).

6. Benefield, John W., A Revised Program for the Integration of Pressure Distribution Data for Bodies of Revolution, TM 54/40-133, Lockheed Missiles & Space Company, Sunnyvale, California, February 1963.

7. Dye, F. E., Jr., Pressure Distribution Tests for Basic Conical Flow Research, OAL Report 160, Convair Division of General Dynamics, Daingerfield, Texas, February 1950.

8. Robertson, J. E. and H. L. Chevalier, Characteristics of Steady-State Pressures on the Cylindrical Portion of Cone-Cylinder Bodies at Transonic Speeds, AEDC-TDR-63-104, Arnold Engineering Development Center, Arnold Air Force Station, Tennessee, August 1963.

9. Erickson, E. W. and E. D. Dowling, Transonic Pressure Tests on a Series of 3.480 Inch Diameter Cone-Cylinder Models in the Convair High Speed Wind Tunnel, HST-TR-021-0, Convair Division of General Dynamics, San Diego, California, 14 April 1961.

10. Reese, H. Bates, Jr., Results of an Experimental Investigation to Determine the Aerodynamic Loadings on Three Saturn Payload Shapes, TN-AE-64-16, Chrysler Corporation, New Orleans, Louisiana, 1 March 1964.

11. Goethert, Bernard H., Transonic Wind Tunnel Testing, Permagon Press, New York, New York, 1961.

12. Ames Research Staff, Equations, Tables and Charts for Compressible Flow, Report 1135, National Advisory Committee for Aeronautics, Moffett Field, California, 1953.

13. Wright, J. M., Jr., Final Data Report, Saturn V/RIFT Wind Tunnel Pressure Test P-61, Document D5-11245, The Boeing Company, Seattle, Washington, May 1963.

14. Pearson, A. O., Surface Pressure Distributions on 0.0628-Scale Models of Proposed Project Fire Space Vehicles at Mach Numbers from 0.25 to 4.63, TN-D-1961, National Aeronautics and Space Administration, Washington, D.C., September 1963.

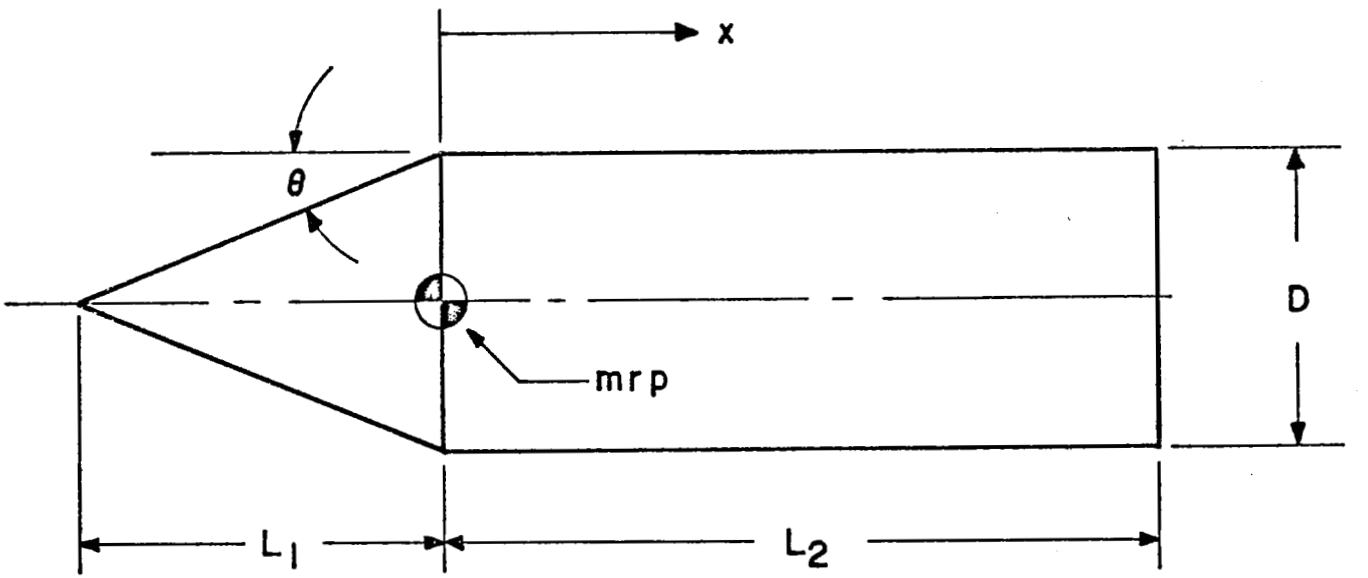

Figure 1 - Configuration Sketch

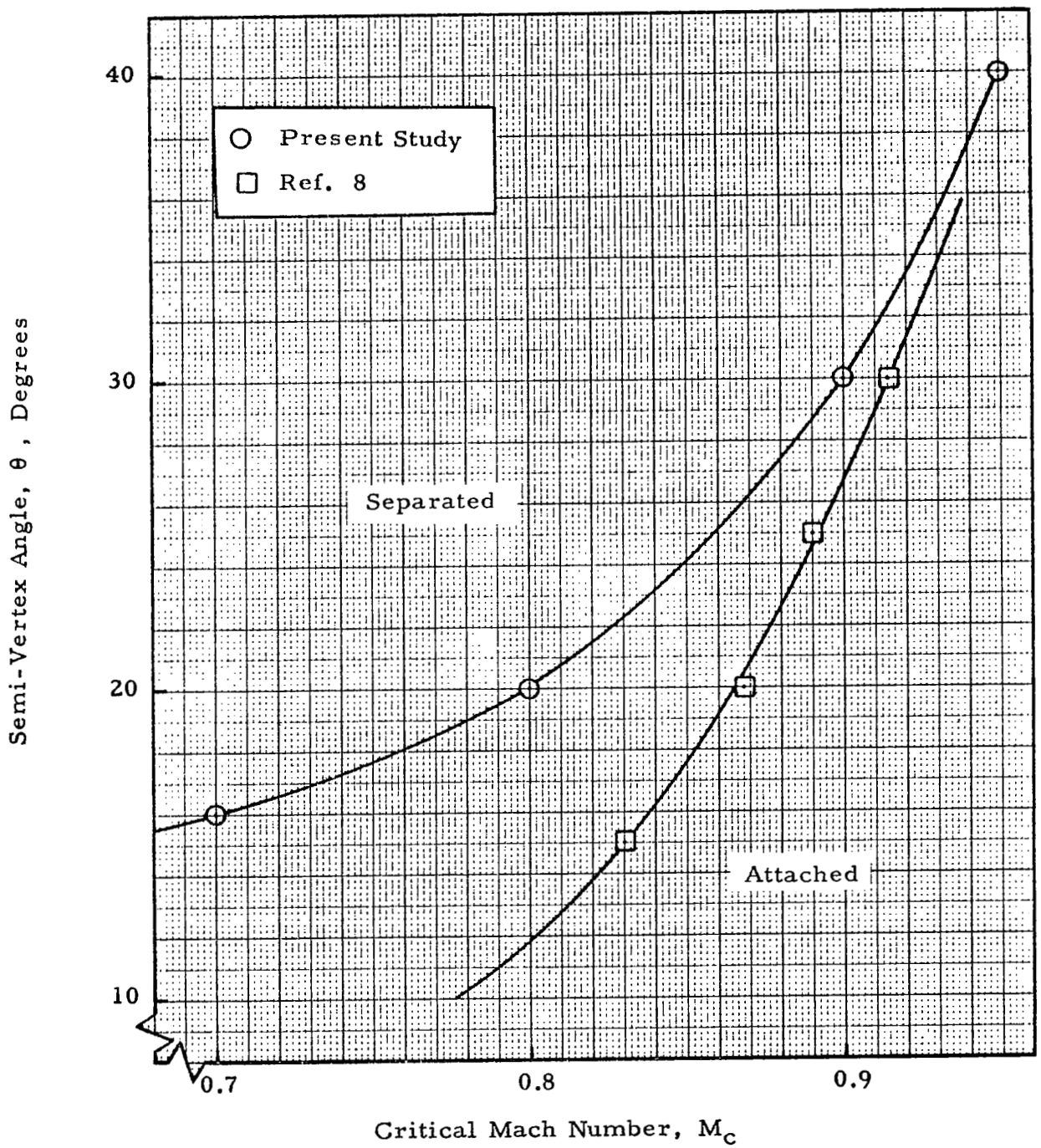

Figure 2 - The Influence of Cone Angle on Critical Flow Separation Mach Number

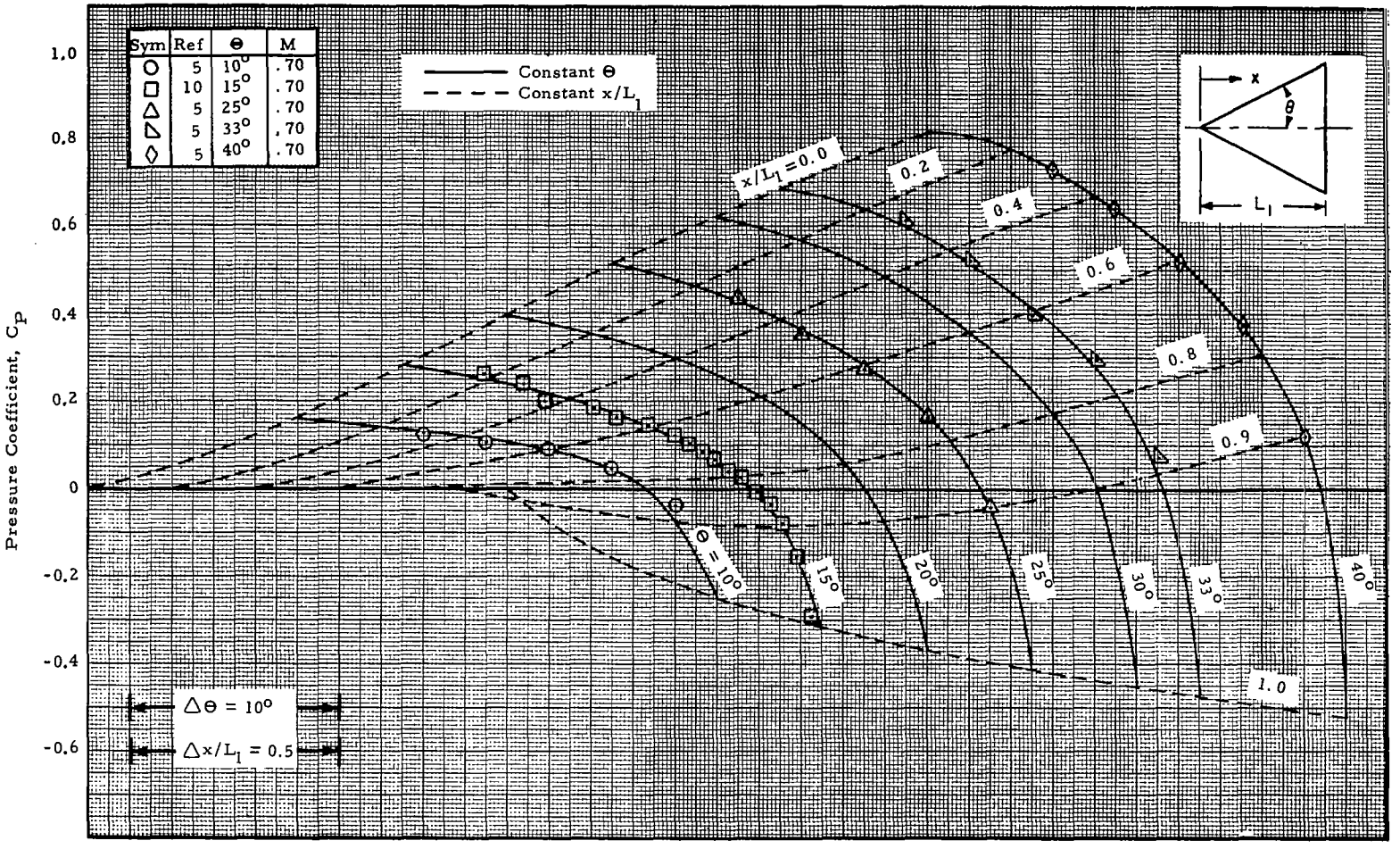

(a) M = 0.7

Figure 3 - Variation of Cone Surface Pressure Distributions with Semi-Vertex Angle for Zero Angle-of-Attack

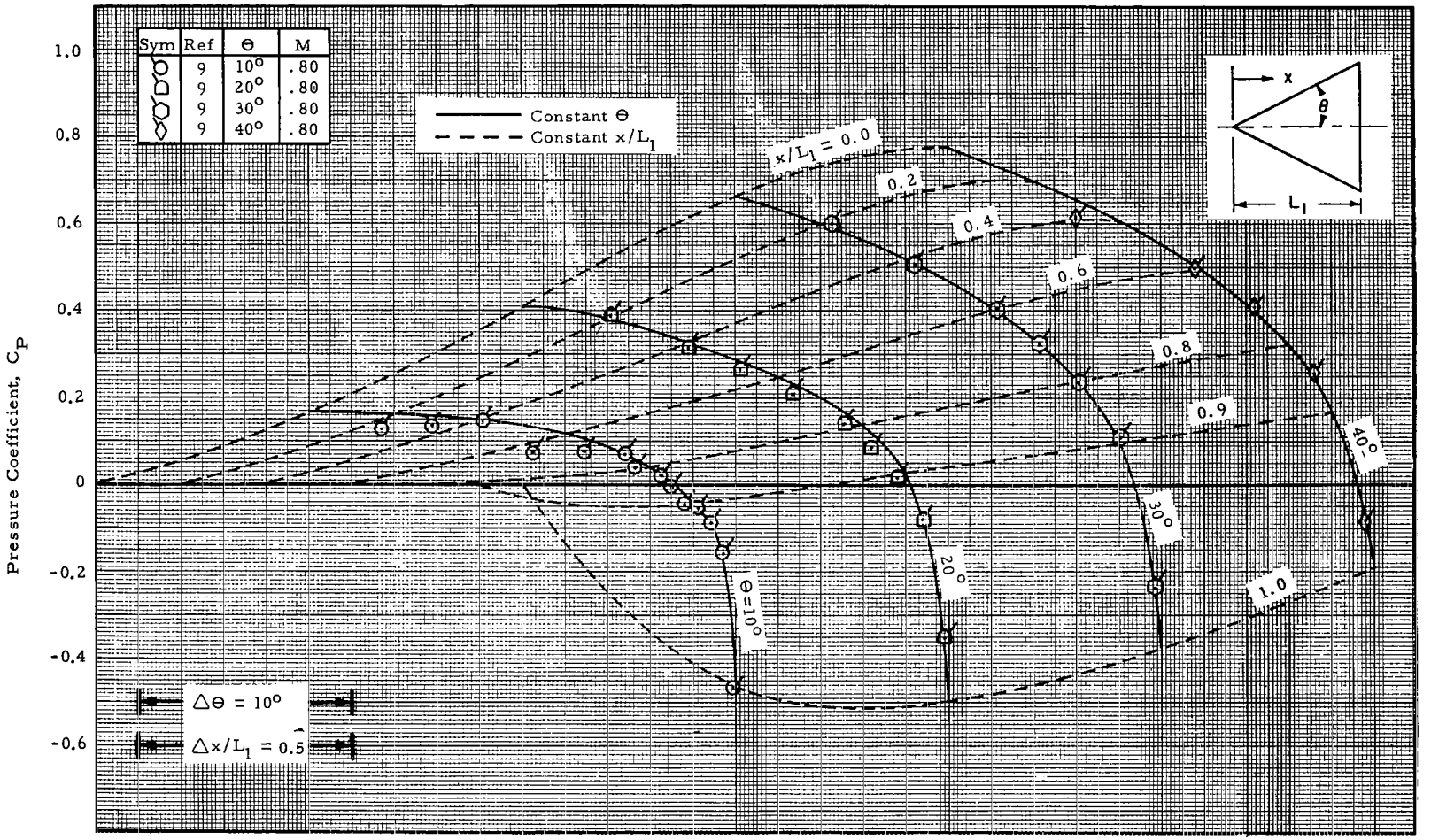

(b) M = 0.8

Figure 3 - Variation of Cone Surface Pressure Distributions with Semi-Vertex Angle for Zero Angle-of-Attack (Cont'd)

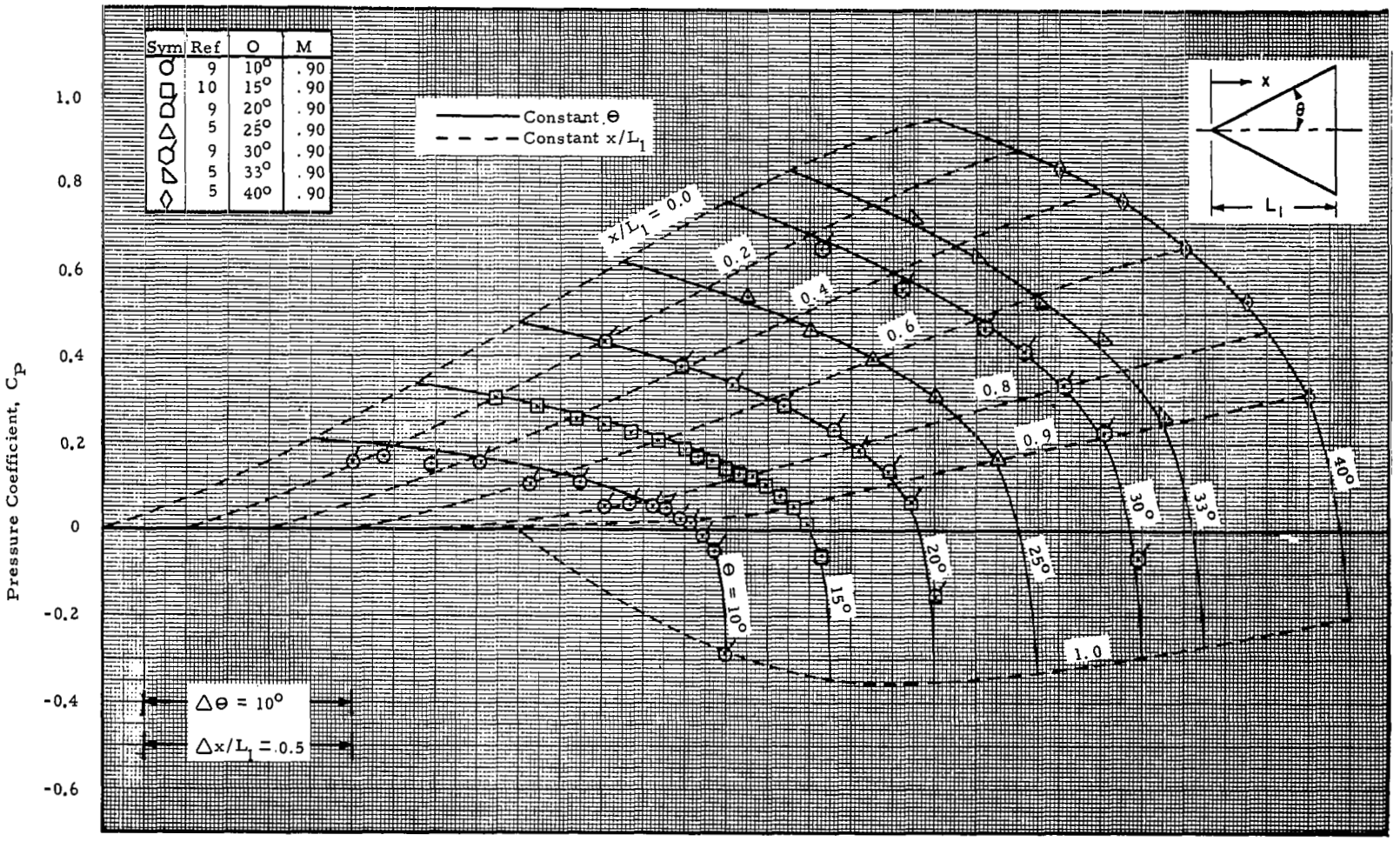

(c) M = 0.9

Figure 3 - Variation of Cone Surface Pressure Distributions with Semi-Vertex Angle for Zero Angle-of-Attack (Cont'd)

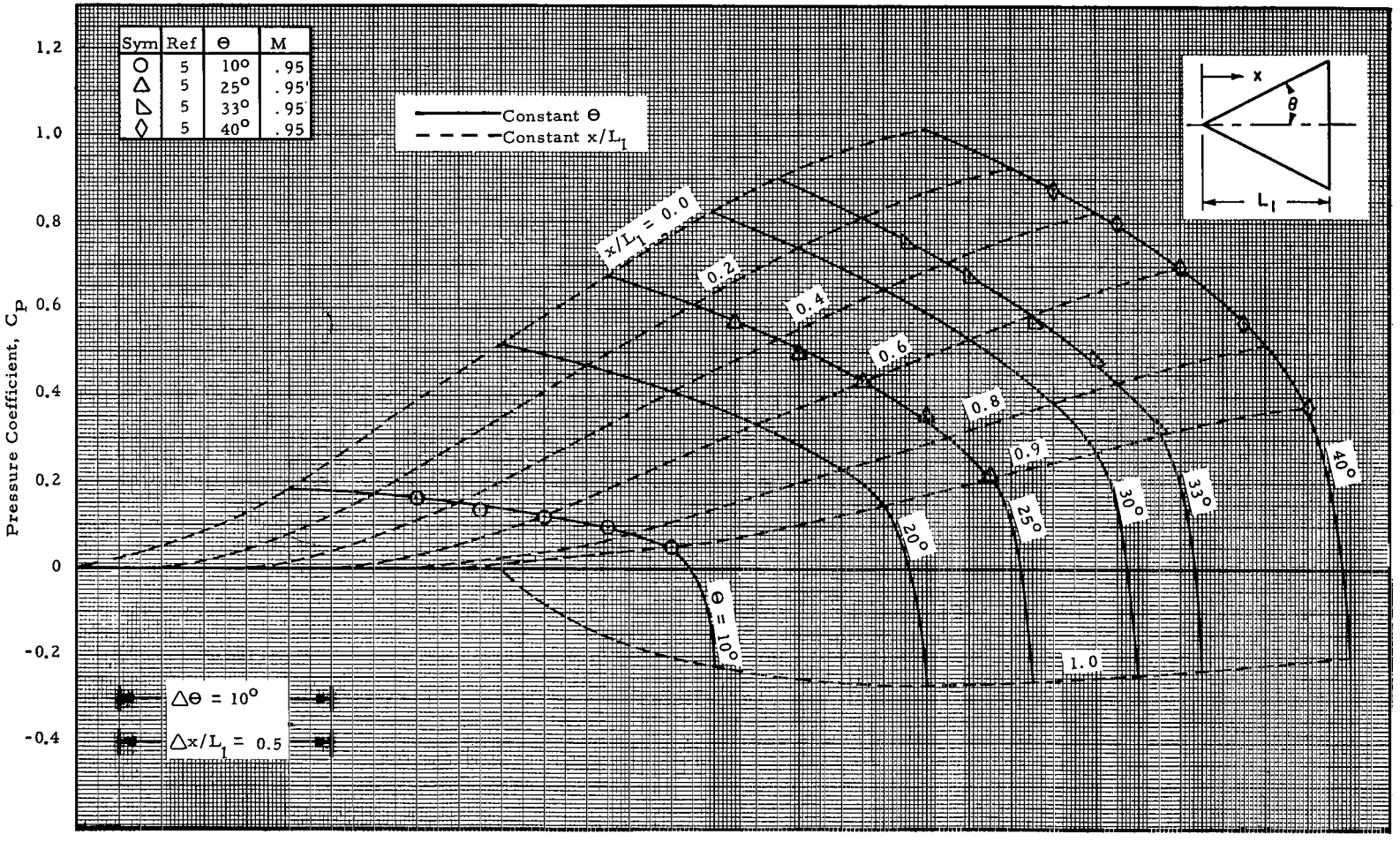

(d) M = 0.95

Figure 3 - Variation of Cone Surface Pressure Distributions with Semi-Vertex Angle for Zero Angle-of-Attack (Cont'd)

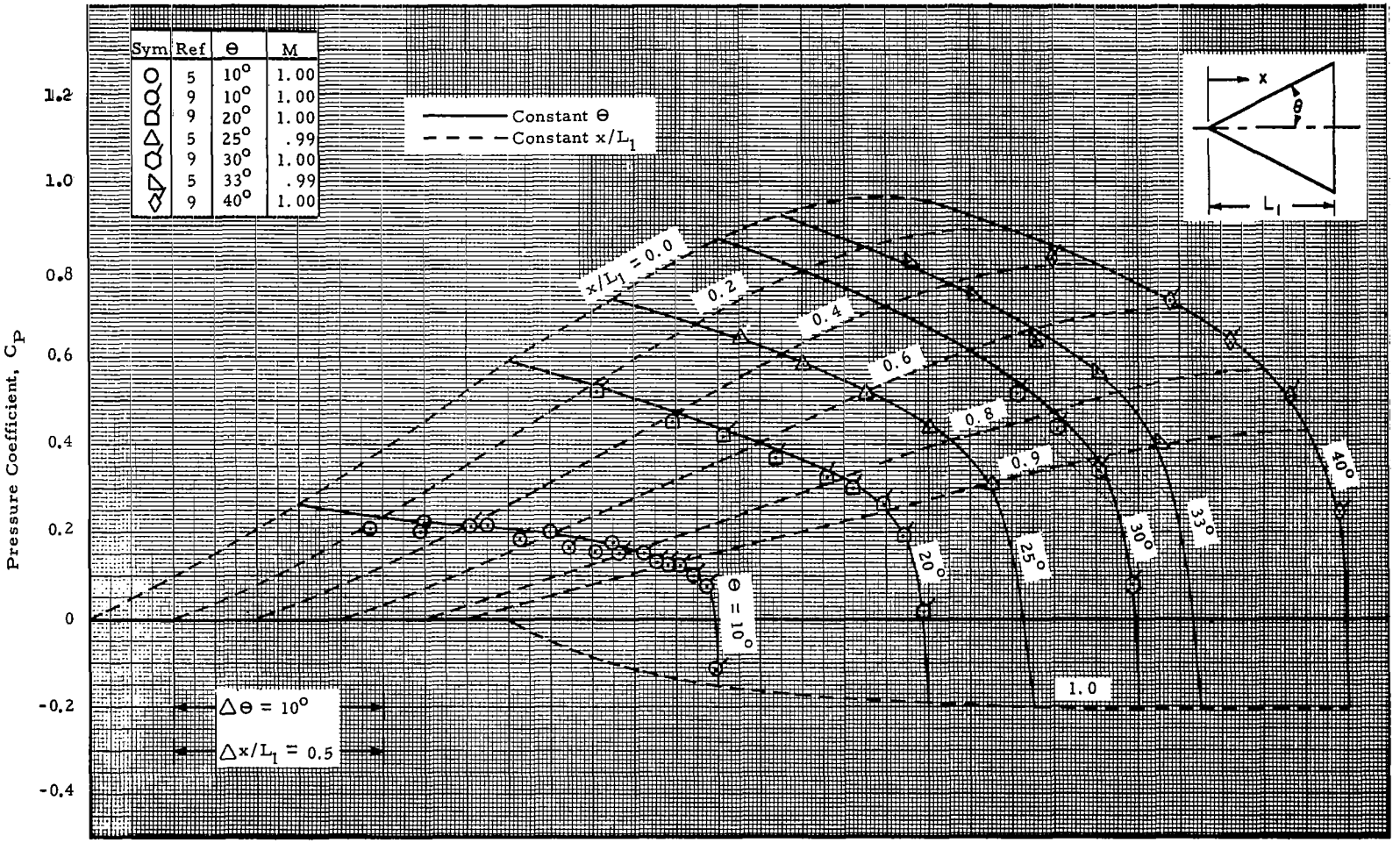

(e) M = 1.0

Figure 3 - Variation of Cone Surface Pressure Distributions with Semi-Vertex Angle for Zero Angle-of-Attack (Cont'd)

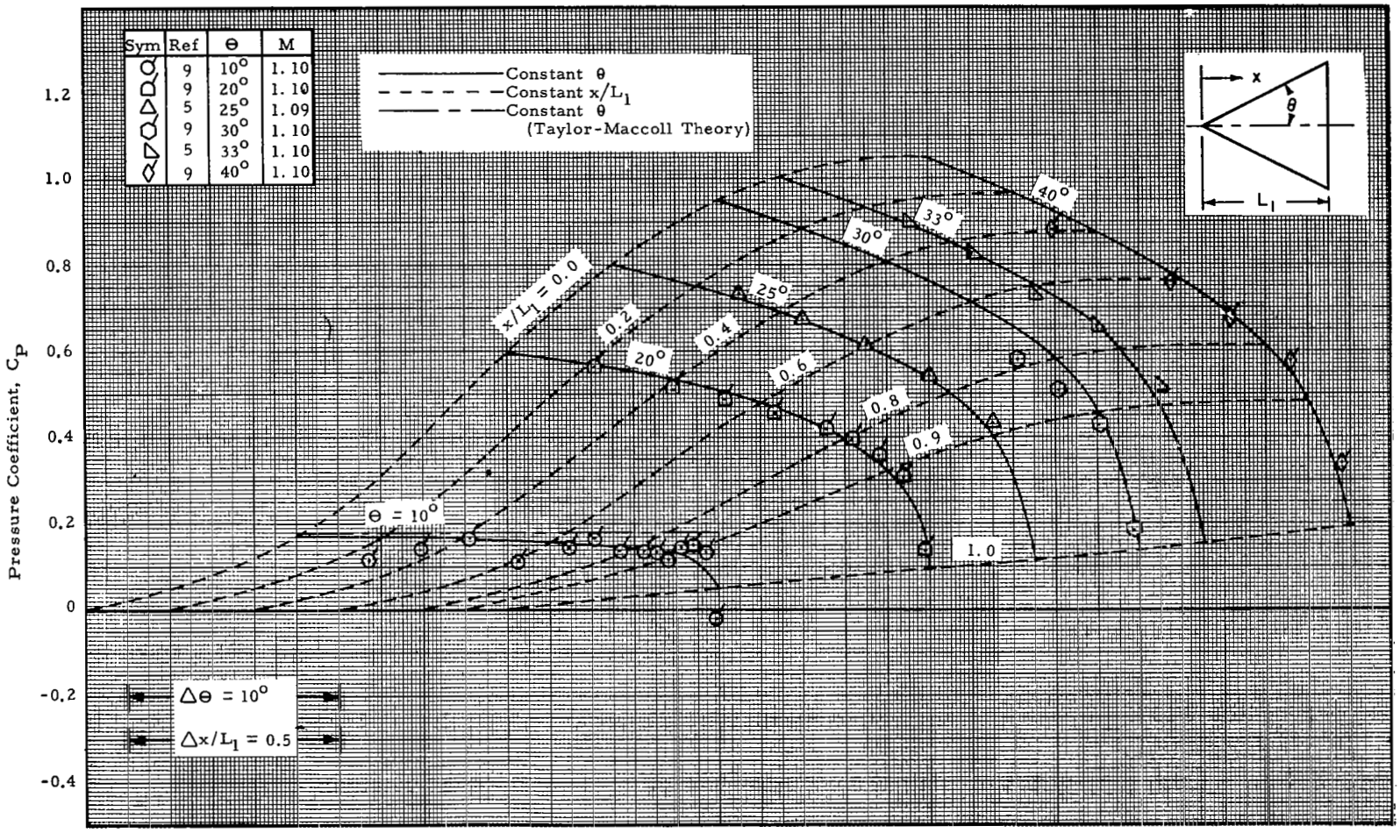

(f) M = 1.1

Figure 3 - Variation of Cone Surface Pressure Distributions with Semi-Vertex Angle for Zero Angle-of-Attack (Cont'd)

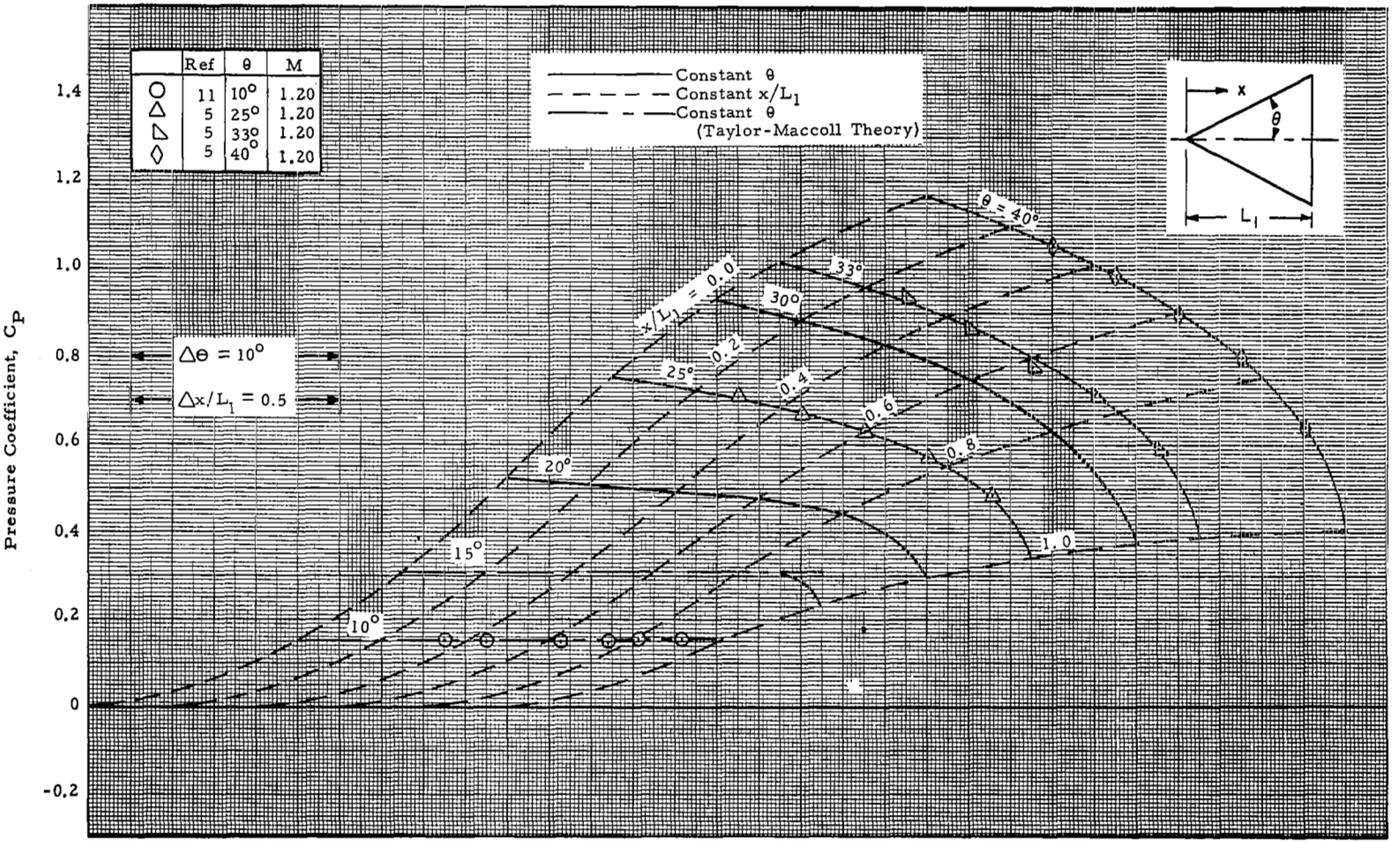

Figure 3 - Variation of Cone Surface Pressure Distributions with Semi-Vertex Angle for Zero Angle-of-Attack (Cont'd)

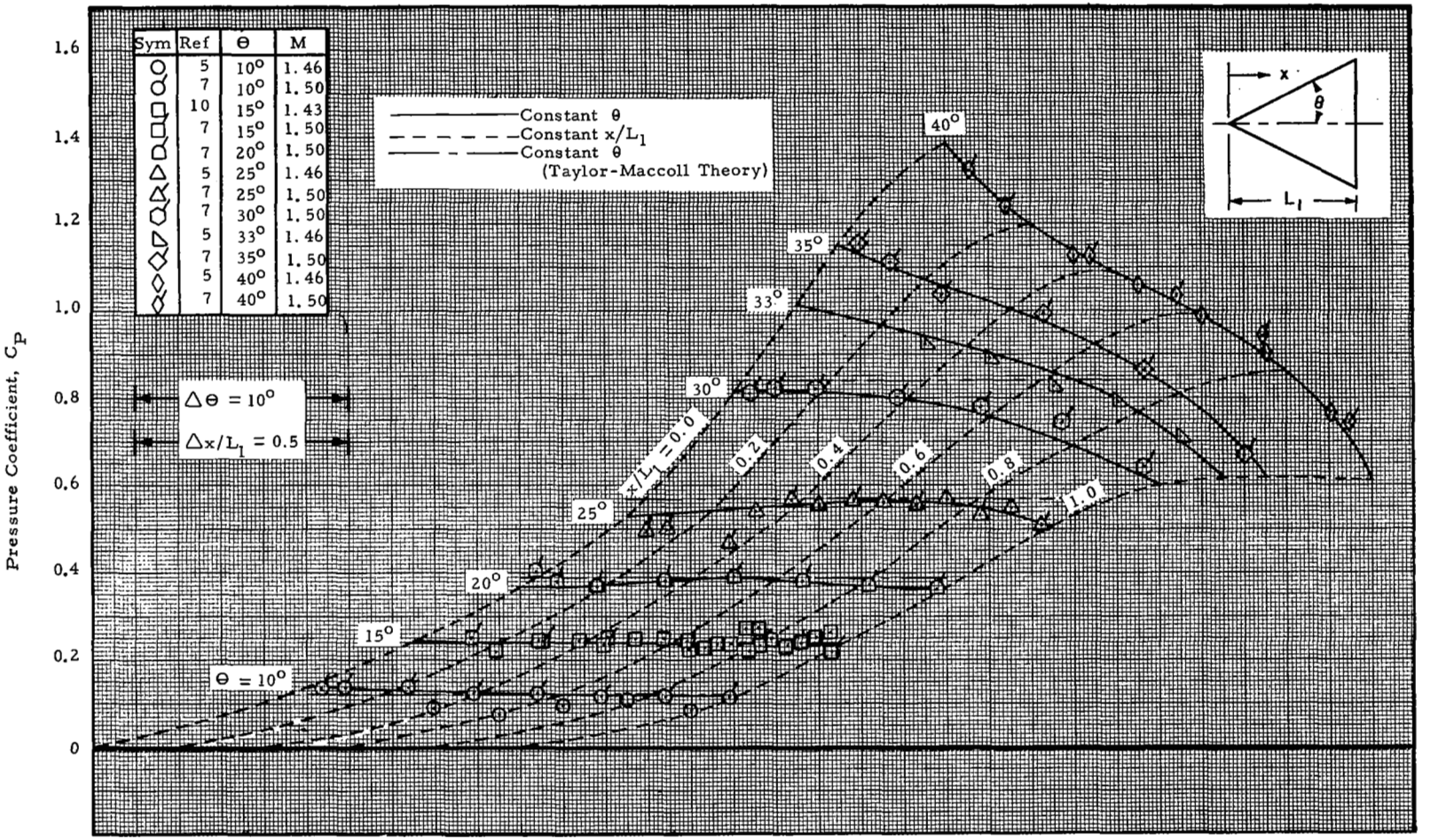

(h) M = 1.5

Figure 3 - Variation of Cone Surface Pressure Distributions with Semi-Vertex Angle for Zero Angle-of-Attack (Cont'd)

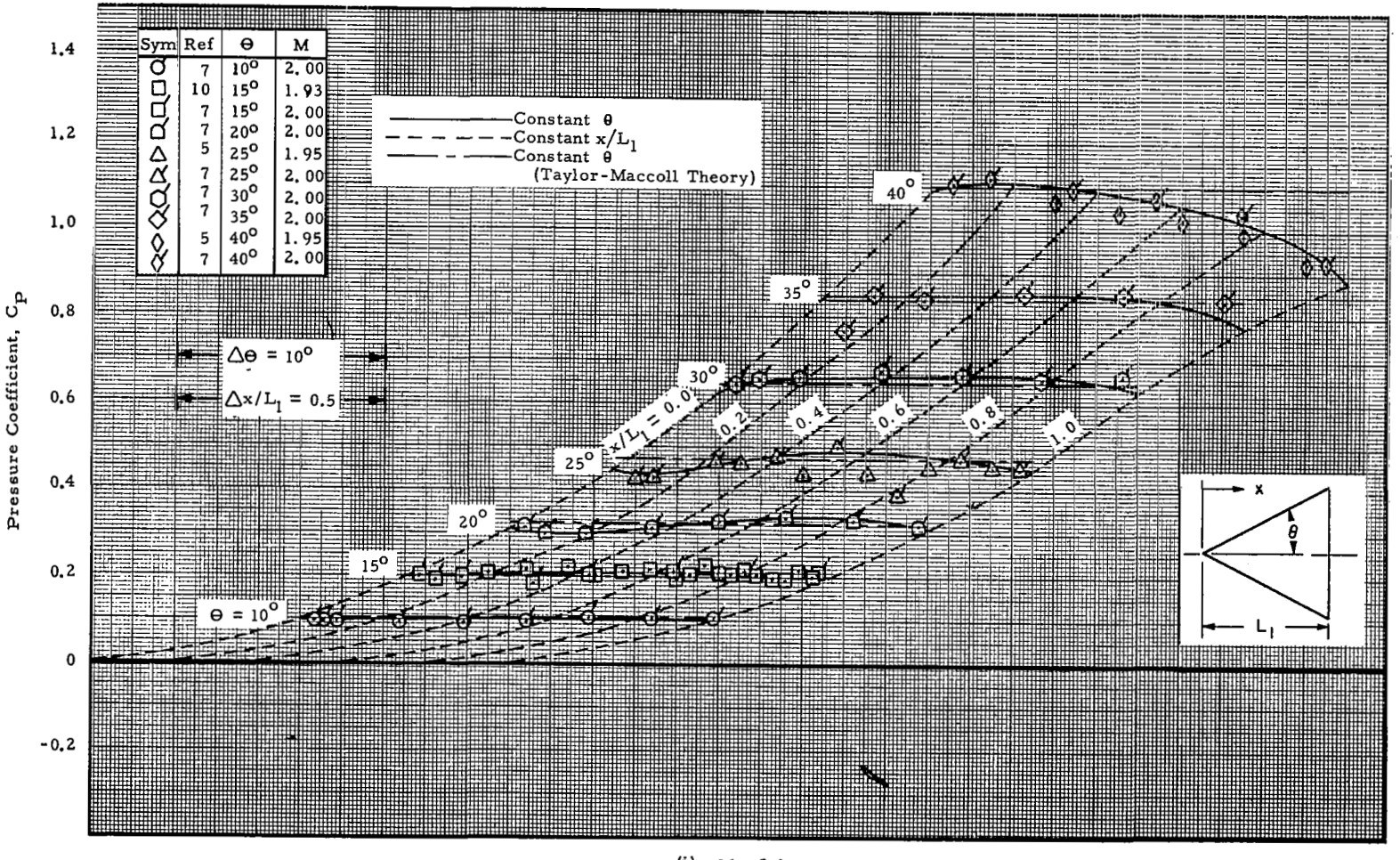

(i) M = 2.0

Figure 3 - Variation of Cone Surface Pressure Distributions with Semi-Vertex Angle for Zero Angle-of-Attack (Concluded)

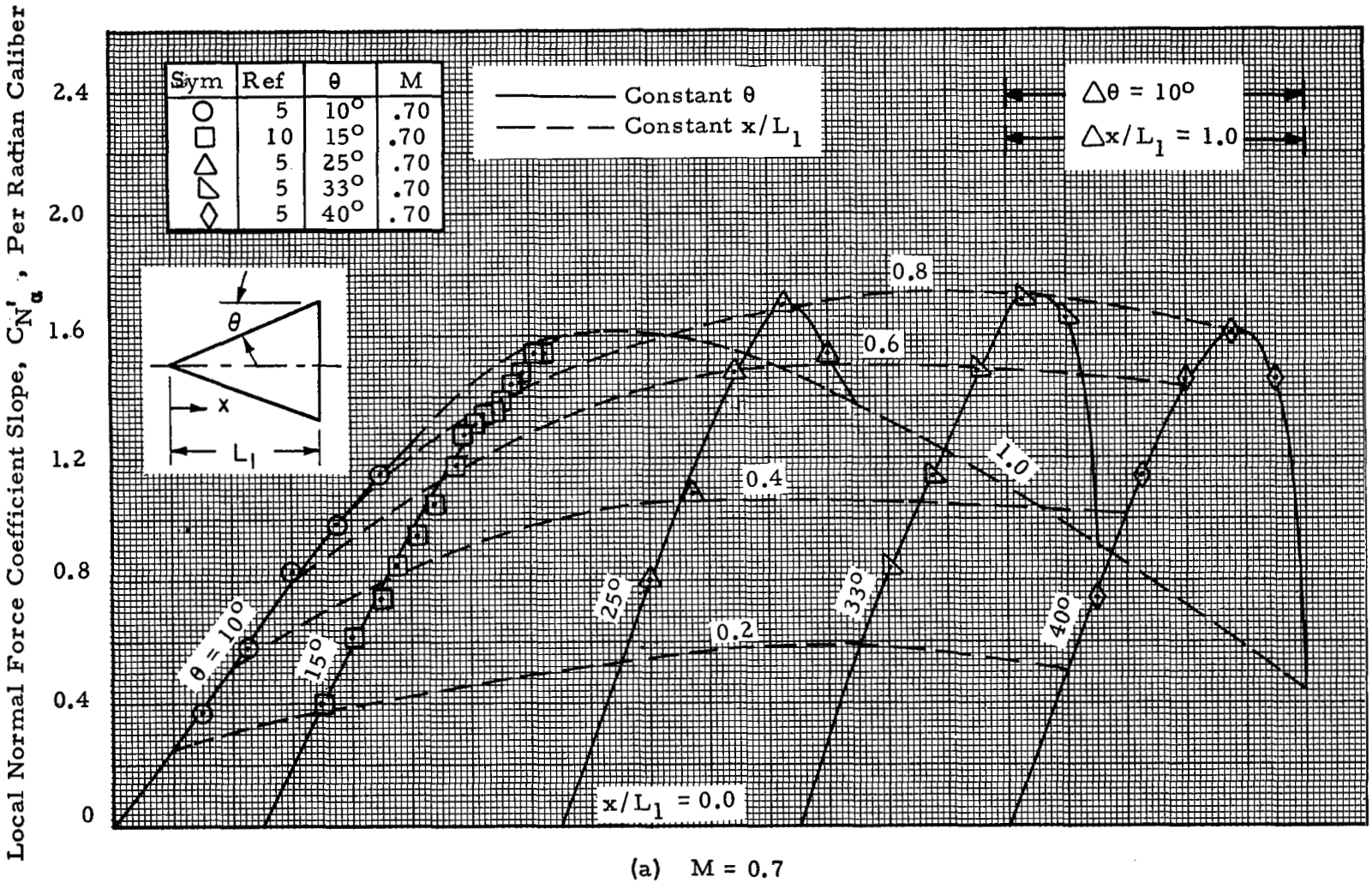

(a) M = 0.7

Figure 4 - The Effect of Semi-Vertex Angle on Local Normal Force Slope Distributions for Cones

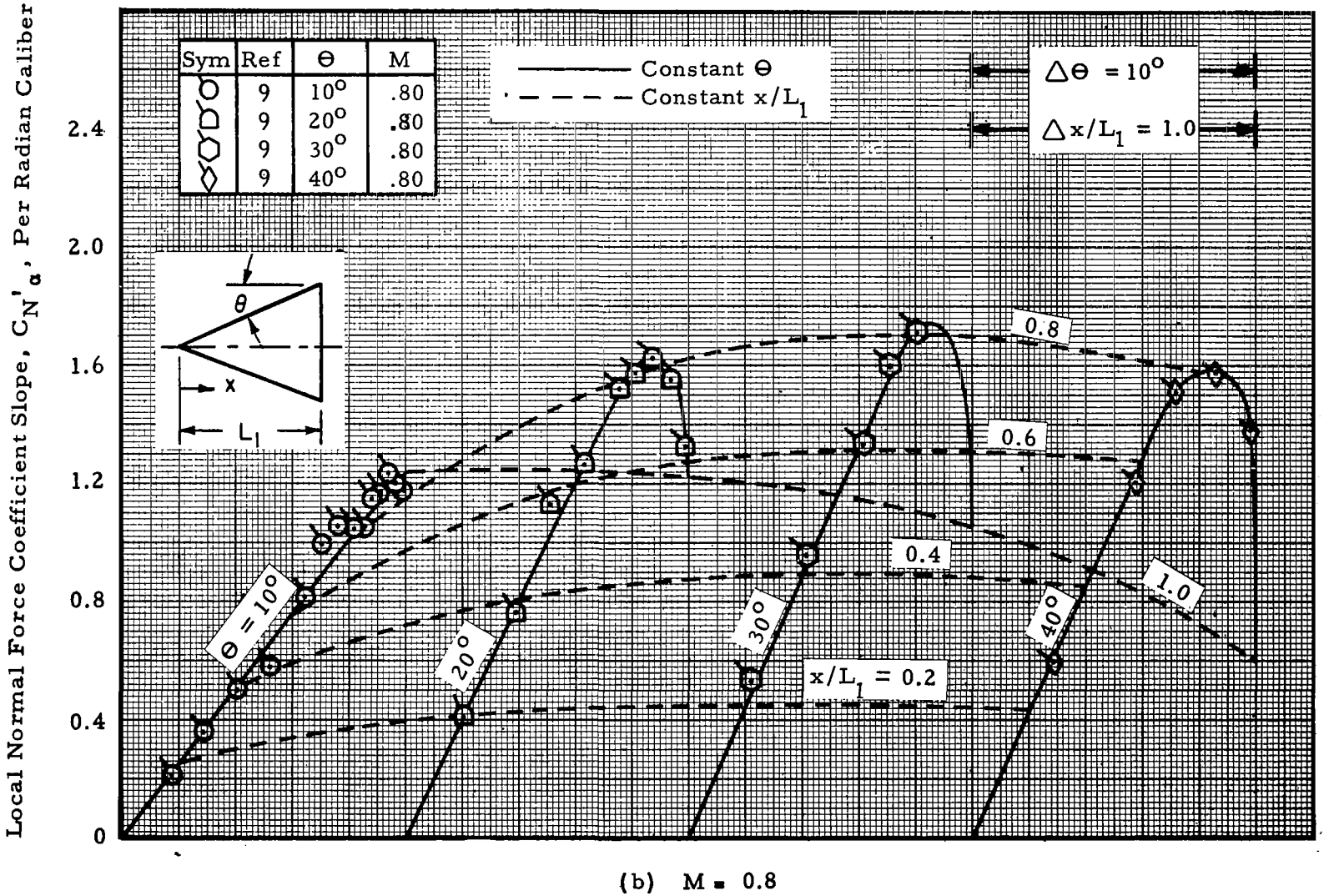

(b) M = 0.8

Figure 4 - The Effect of Semi-Vertex Angle on Local Normal Force Slope Distributions for Cones (Cont'd)

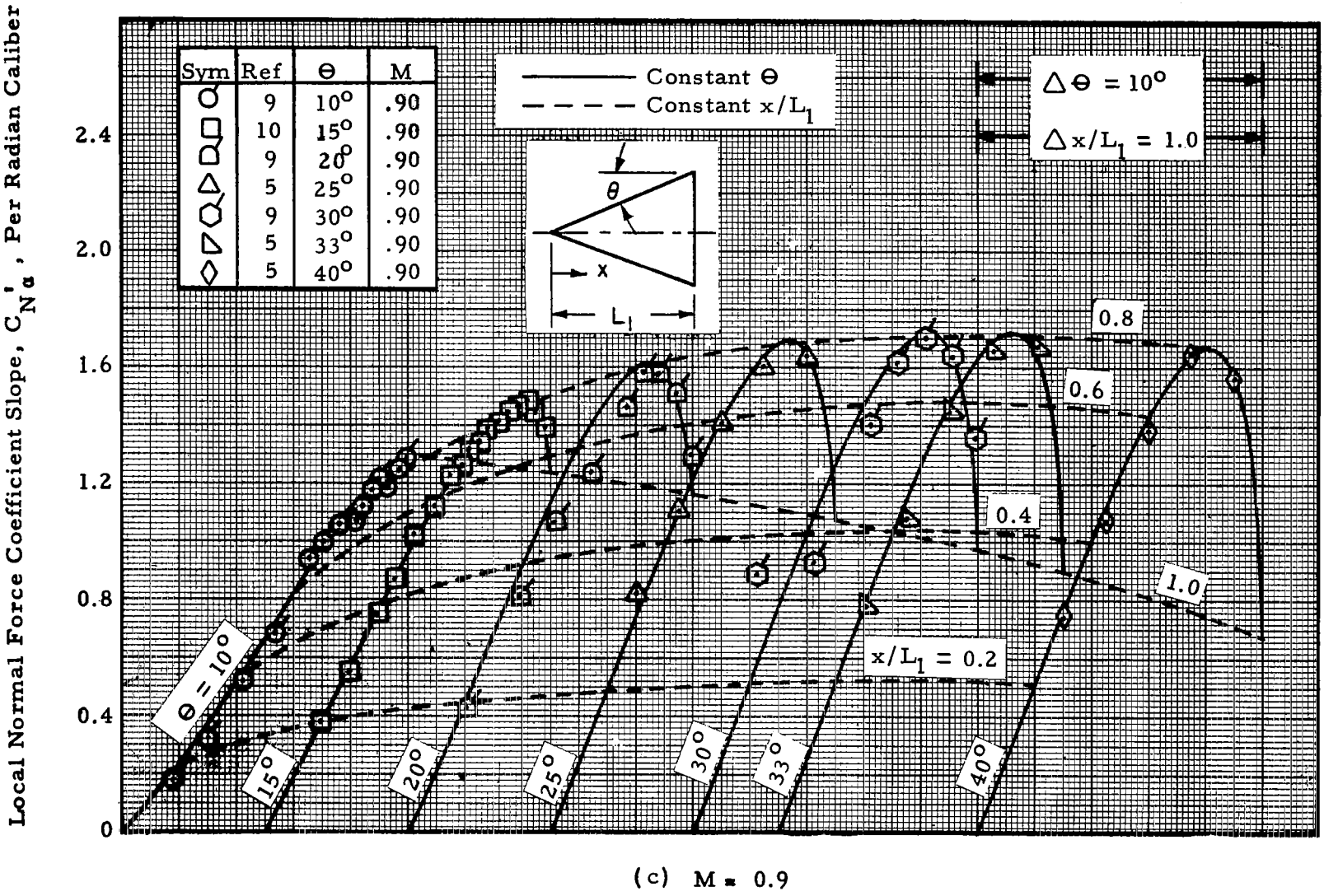

(c) M = 0.9

Figure 4 - The Effect of Semi-Vertex Angle on Local Normal Force Slope Distributions for Cones (Cont'd)

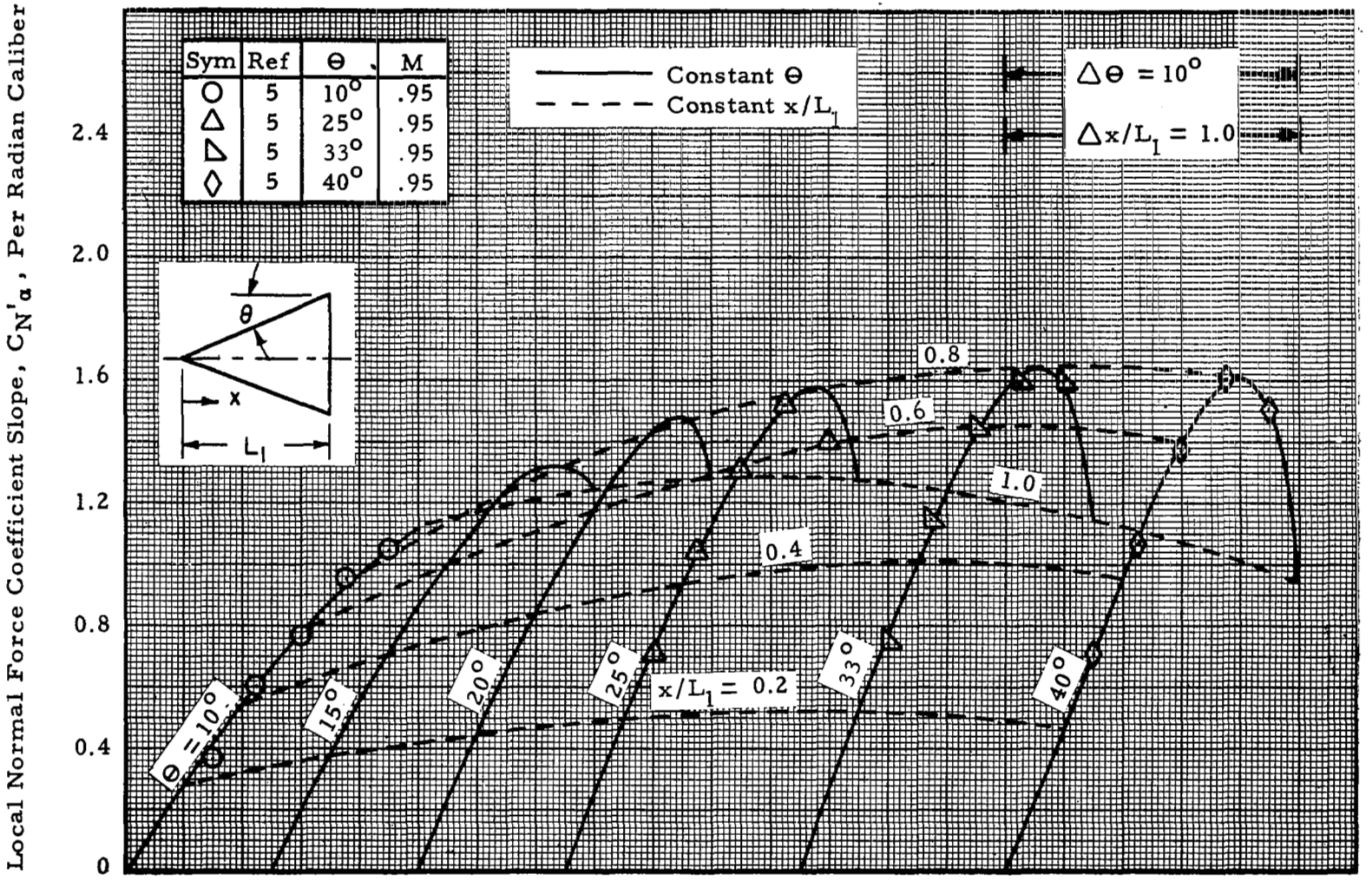

(d) M = 0.95

Figure 4 - The Effect of Semi-Vertex Angle on Local Normal Force Slope Distributions for Cones (Cont'd)

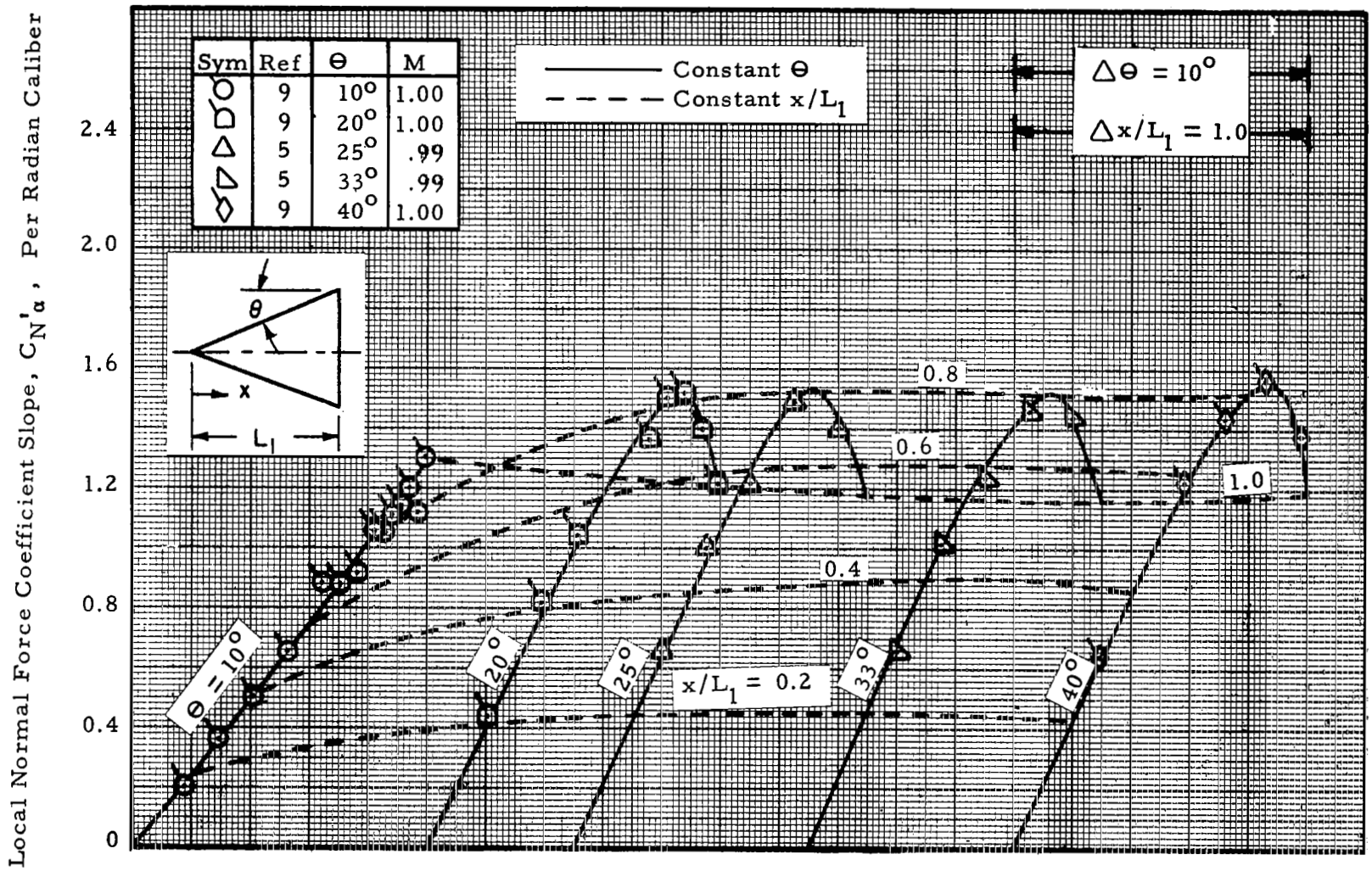

(e) M = 1.0

Figure 4 - The Effect of Semi-Vertex Angle on Local Normal Force Slope Distributions for Cones (Cont'd)

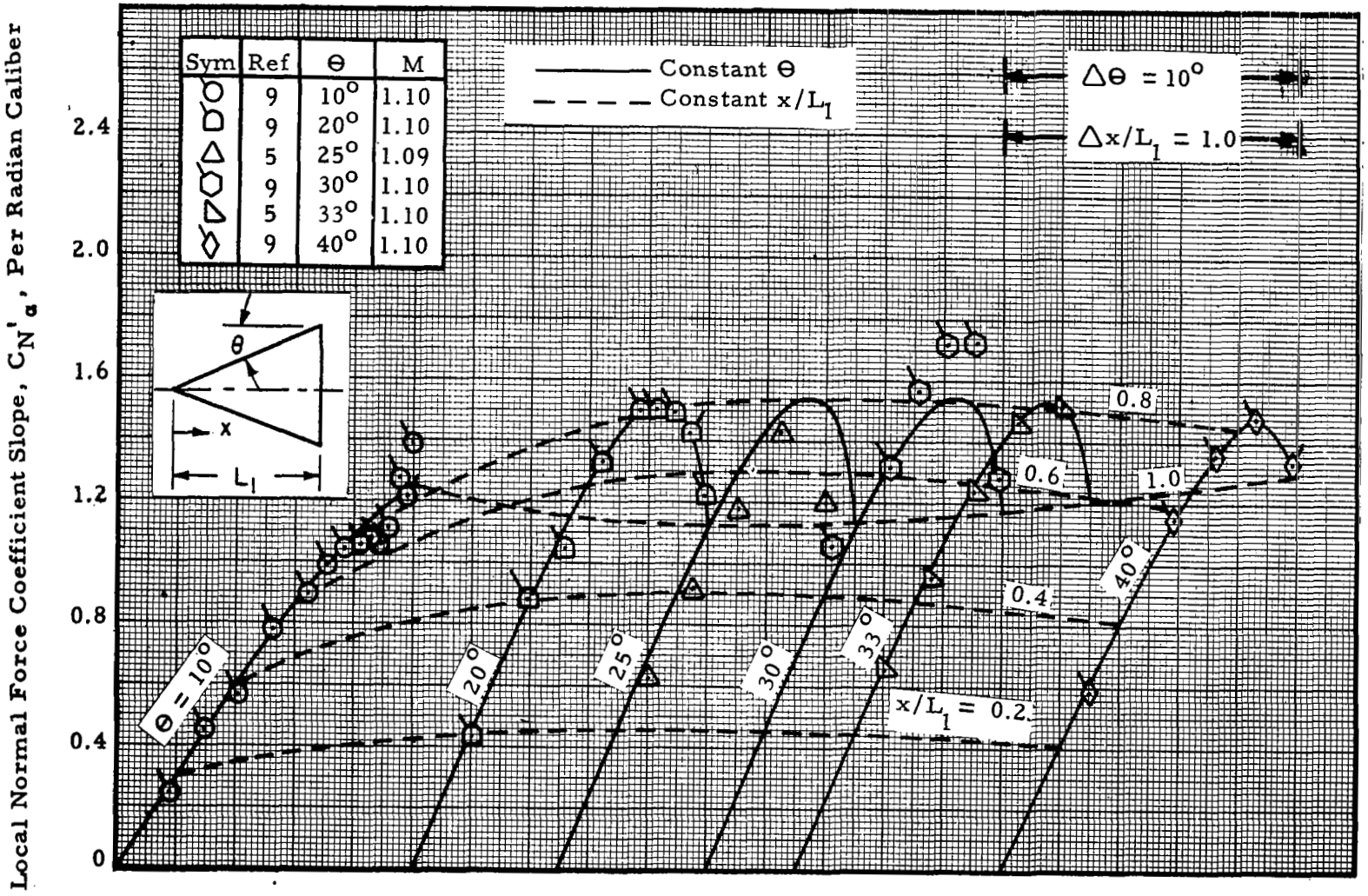

(f) M = 1.1

Figure 4 - The Effect of Semi-Vertex Angle on Local Normal Force Slope Distributions for Cones (Cont'd)

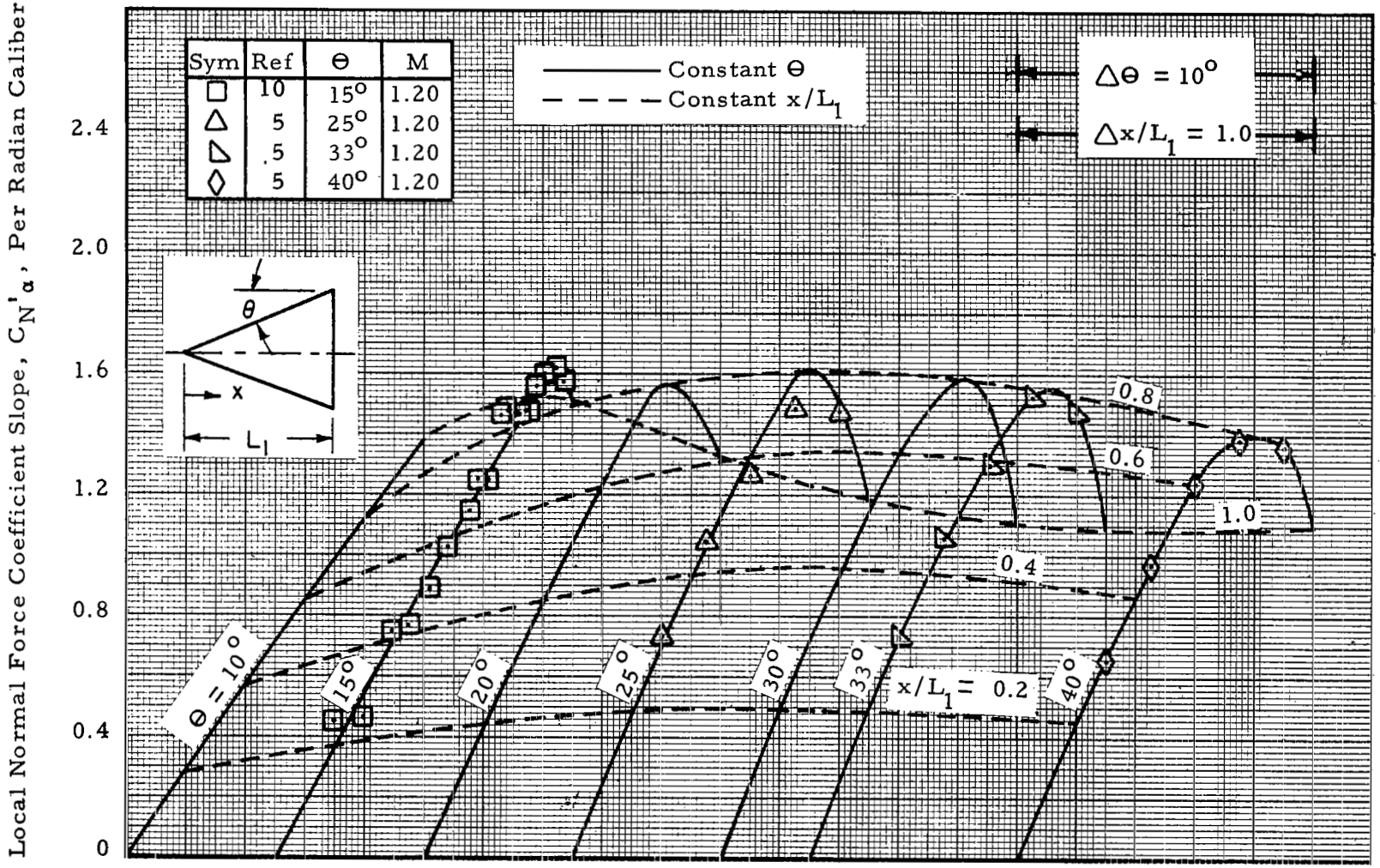

(g) M = 1.2

Figure 4 - The Effect of Semi-Vertex Angle on Local Normal Force Slope Distributions for Cones (Cont'd)

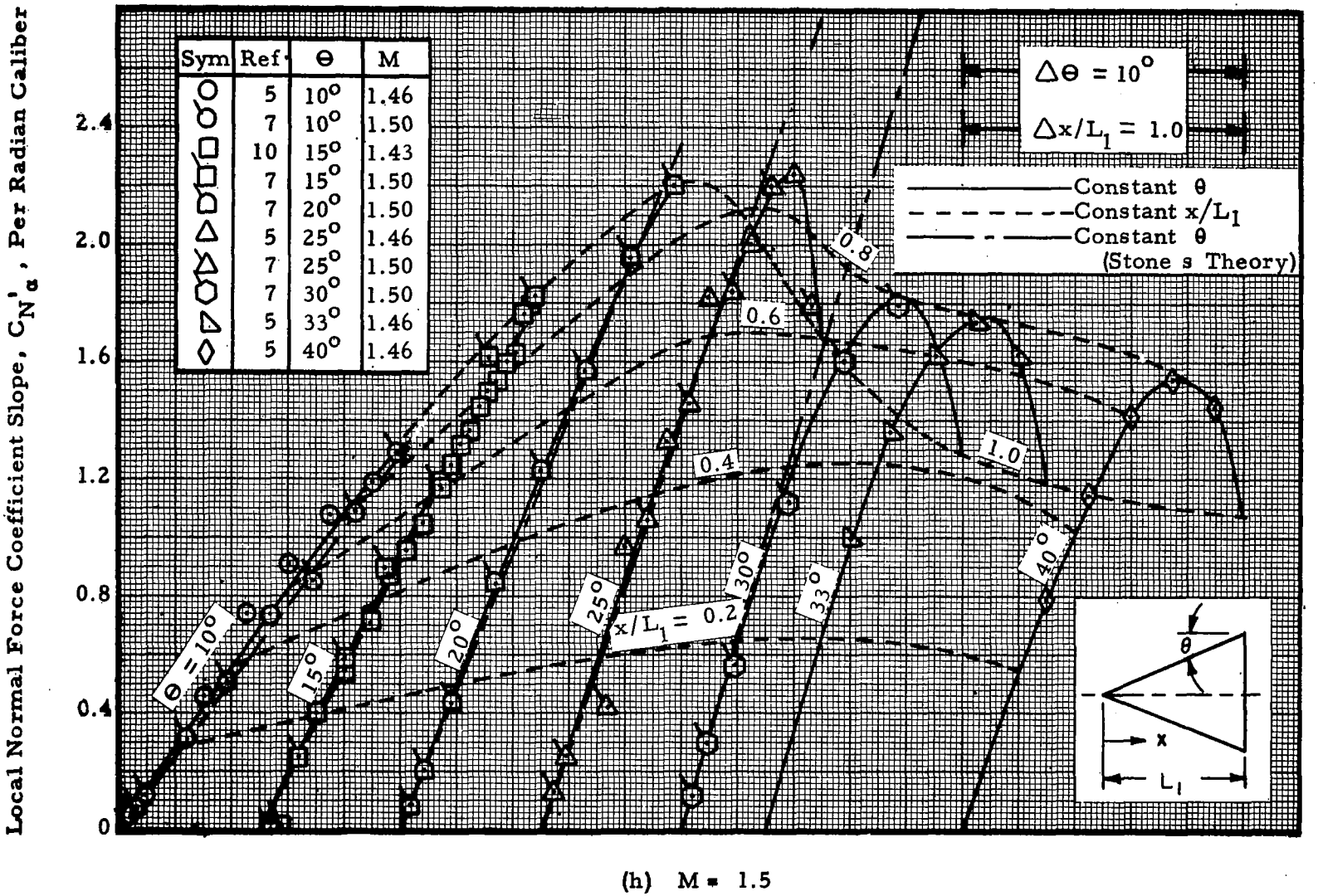

(h) M = 1.5

Figure 4 - The Effect of Semi-Vertex Angle on Local Normal Force Slope Distributions for Cones

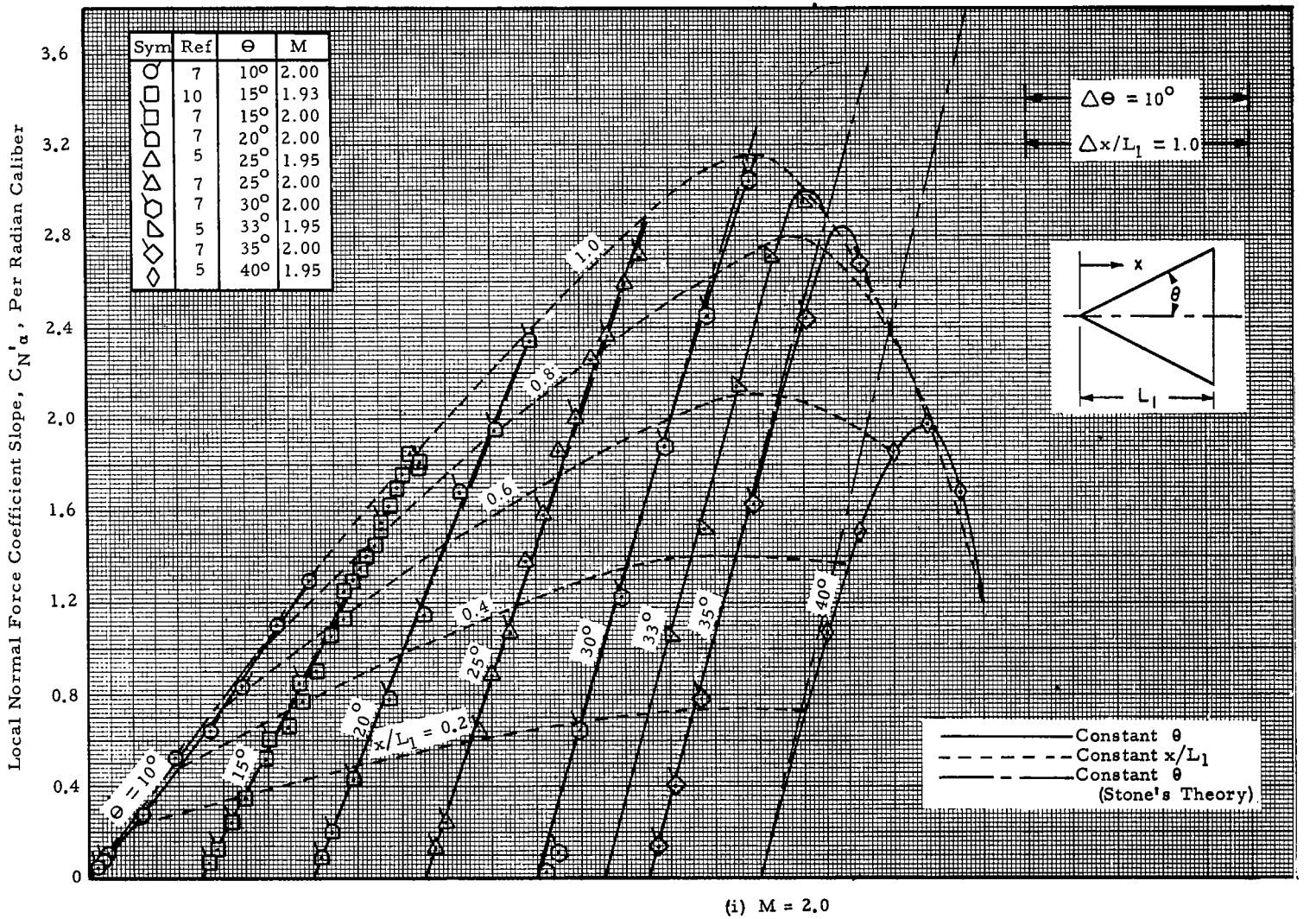

(i) M = 2.0

Figure 4 - The Effect of Semi-Vertex Angle on Local Normal Force Slope Distributions for Cones (Concluded)

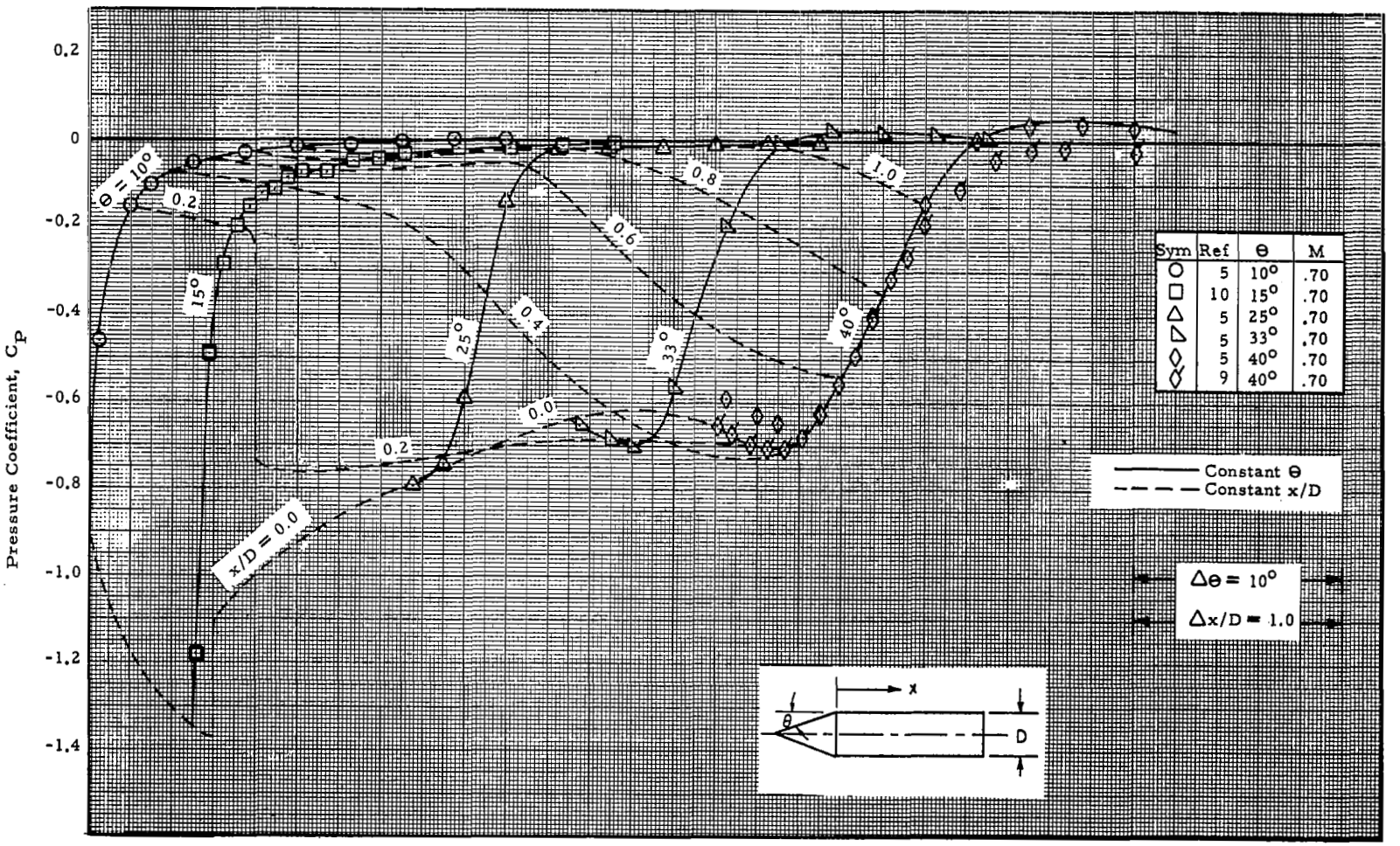

(a) M = 0.7

Figure 5 - Variation of Cylinder Surface Pressure Distributions with Cone Angle for Cone-Cylinders at Zero Angle-of-Attack

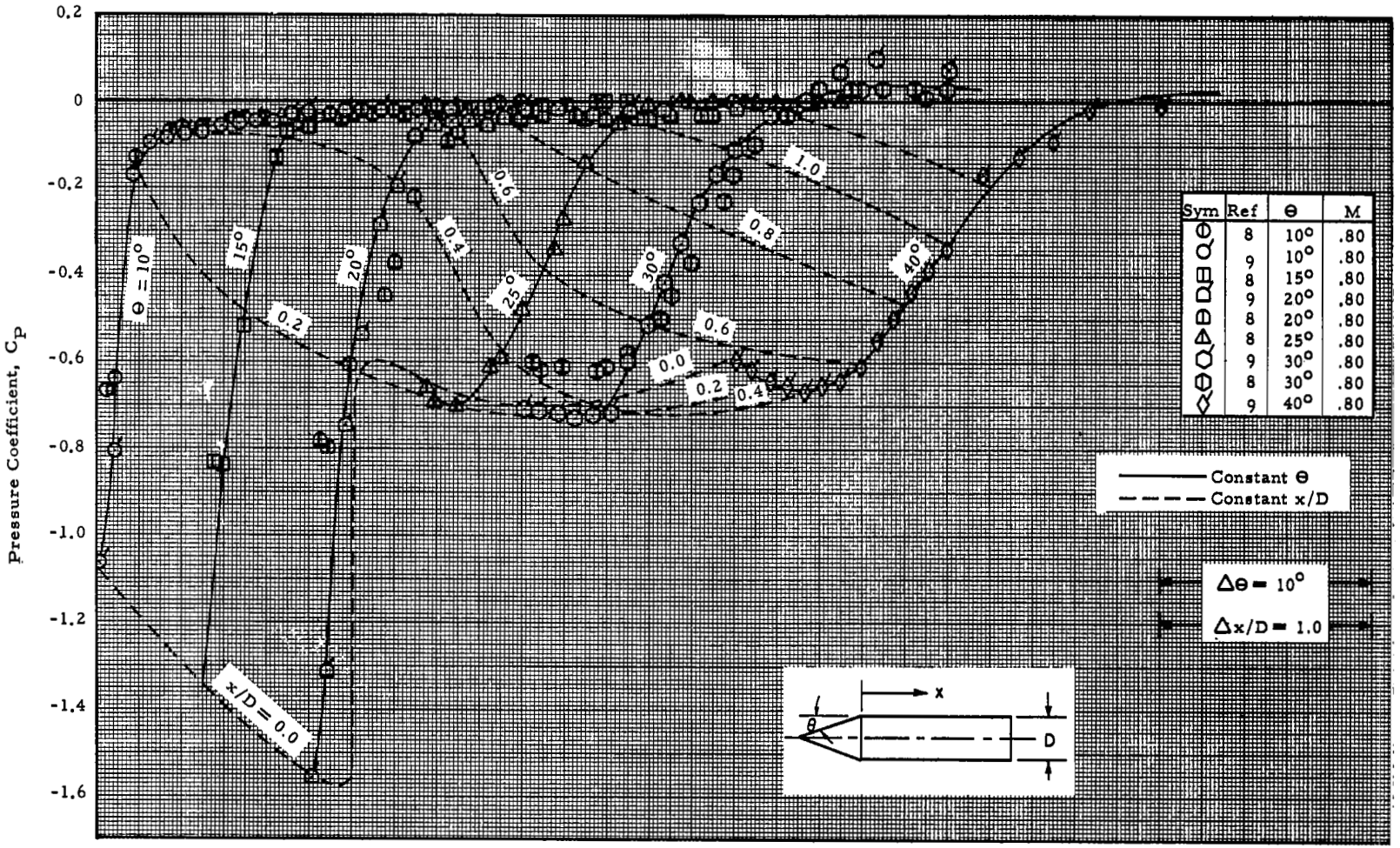

(b) M = 0.8

Figure 5- Variation of Cylinder Surface Pressure Distributions with Cone Angle for Cone-Cylinders at Zero Angle-of-Attack (Cont'd)

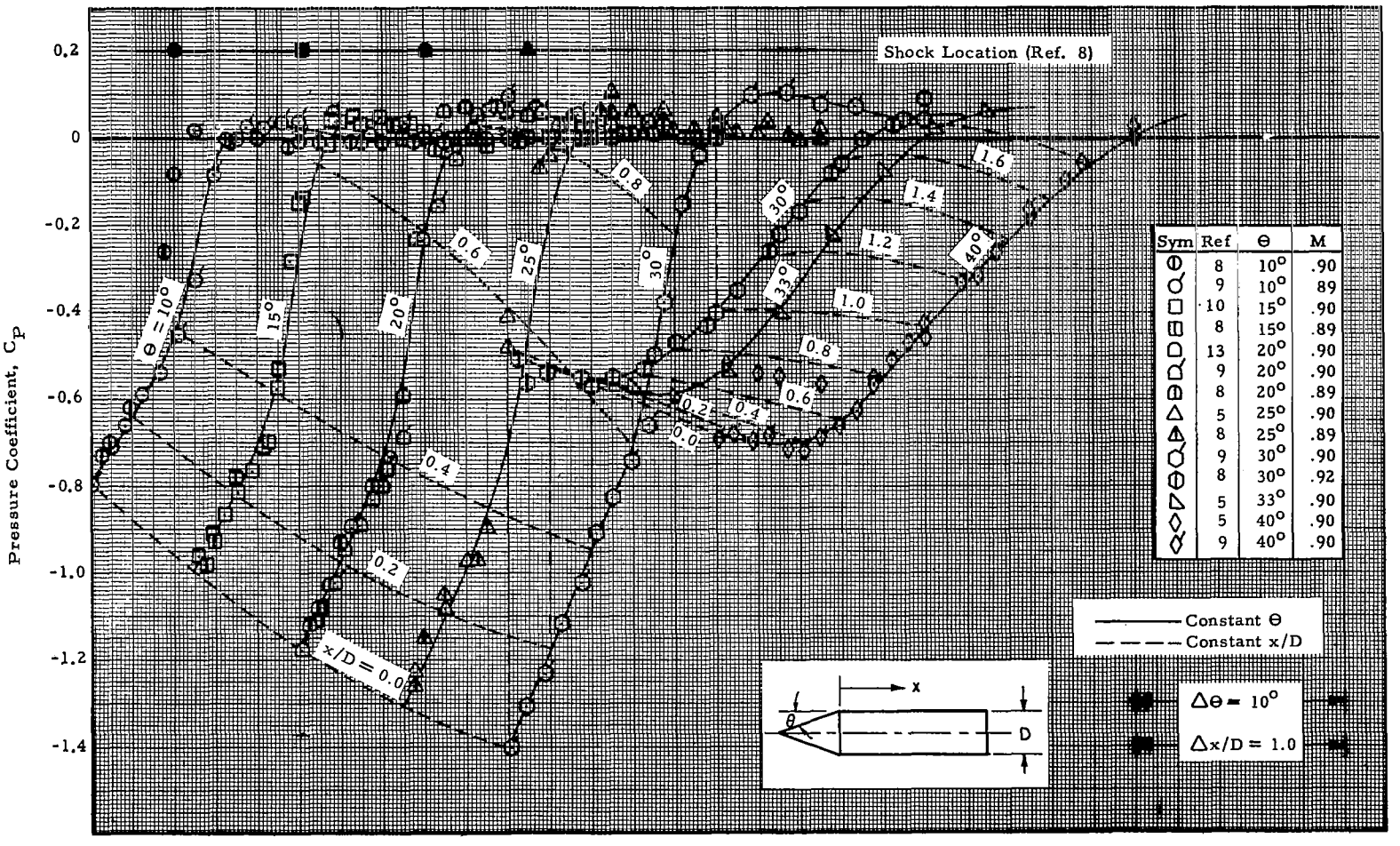

(c) M = 0.9

Figure 5 - Variation of Cylinder Surface Pressure Distributions with Cone Angle for Cone-Cylinders at Zero Angle-of-Attack (Cont'd)

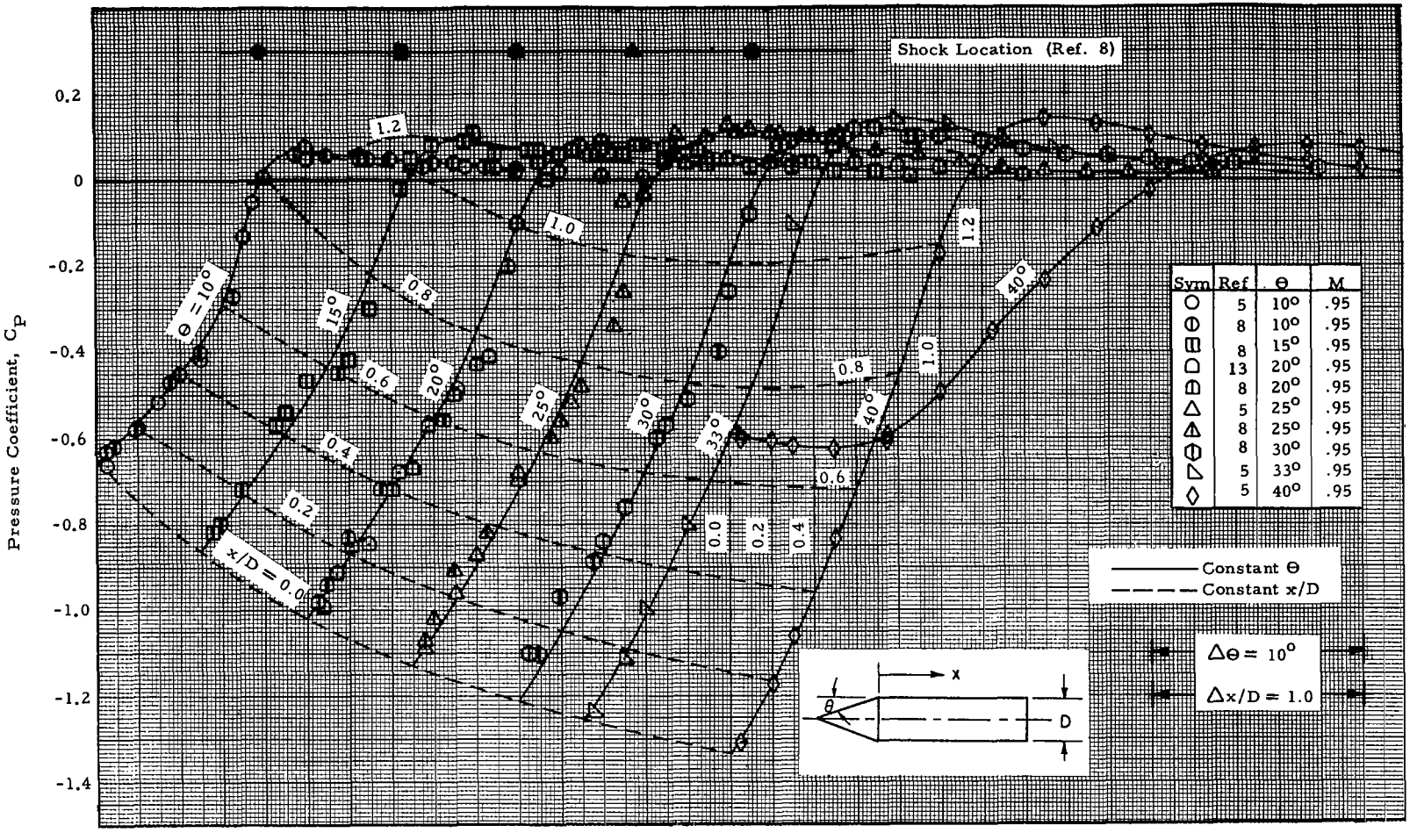

(d) M = 0.95

Figure 5 - Variation of Cylinder Surface Pressure Distributions with Cone Angle for Cone-Cylinders at Zero Angle-of-Attack (Cont'd)

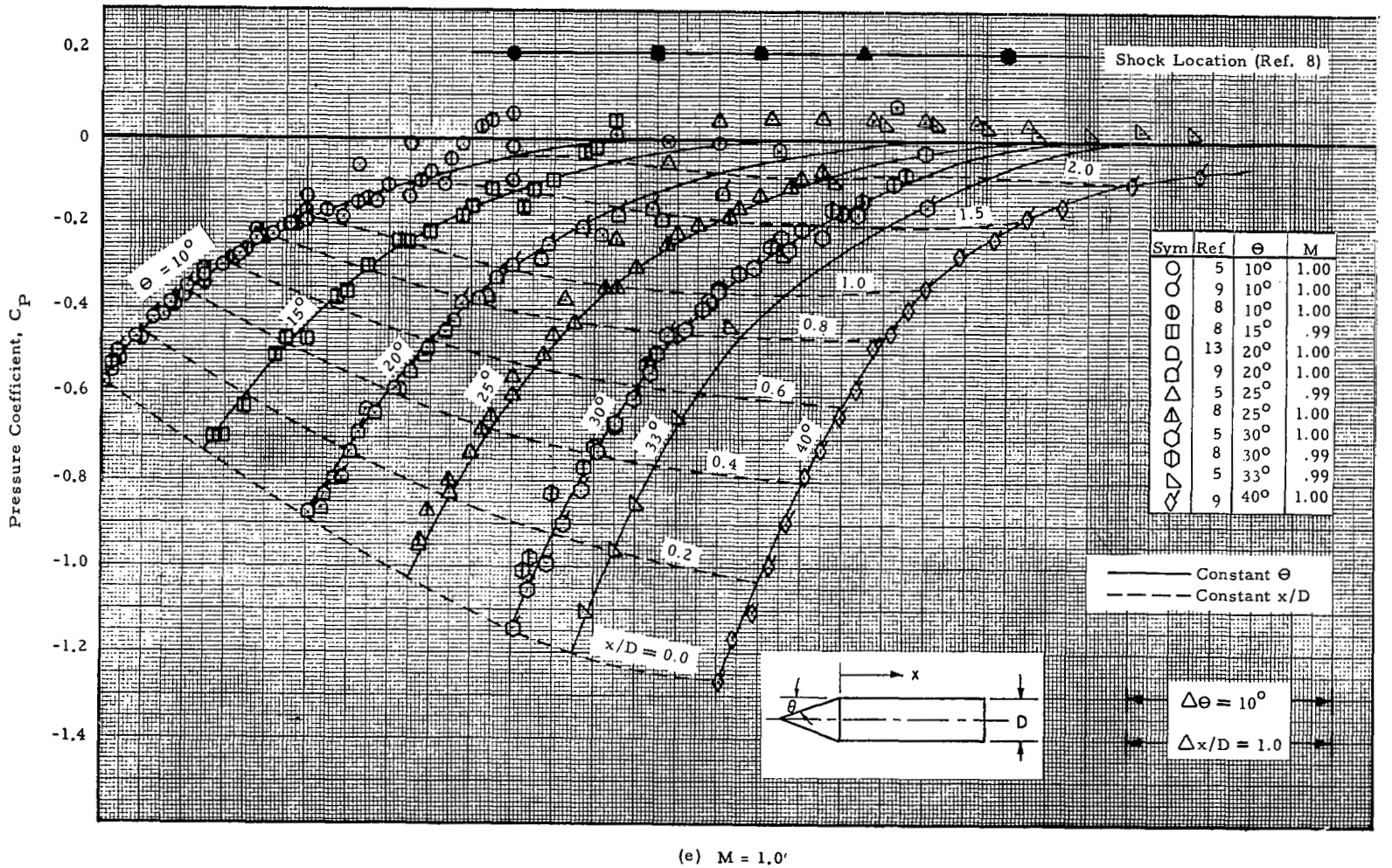

(e) M = 1.0

Figure 5 - Variation of Cylinder Surface Pressure Distributions with Cone Angle for Cone-Cylinders at Zero Angle-of-Attack (Cont'd)

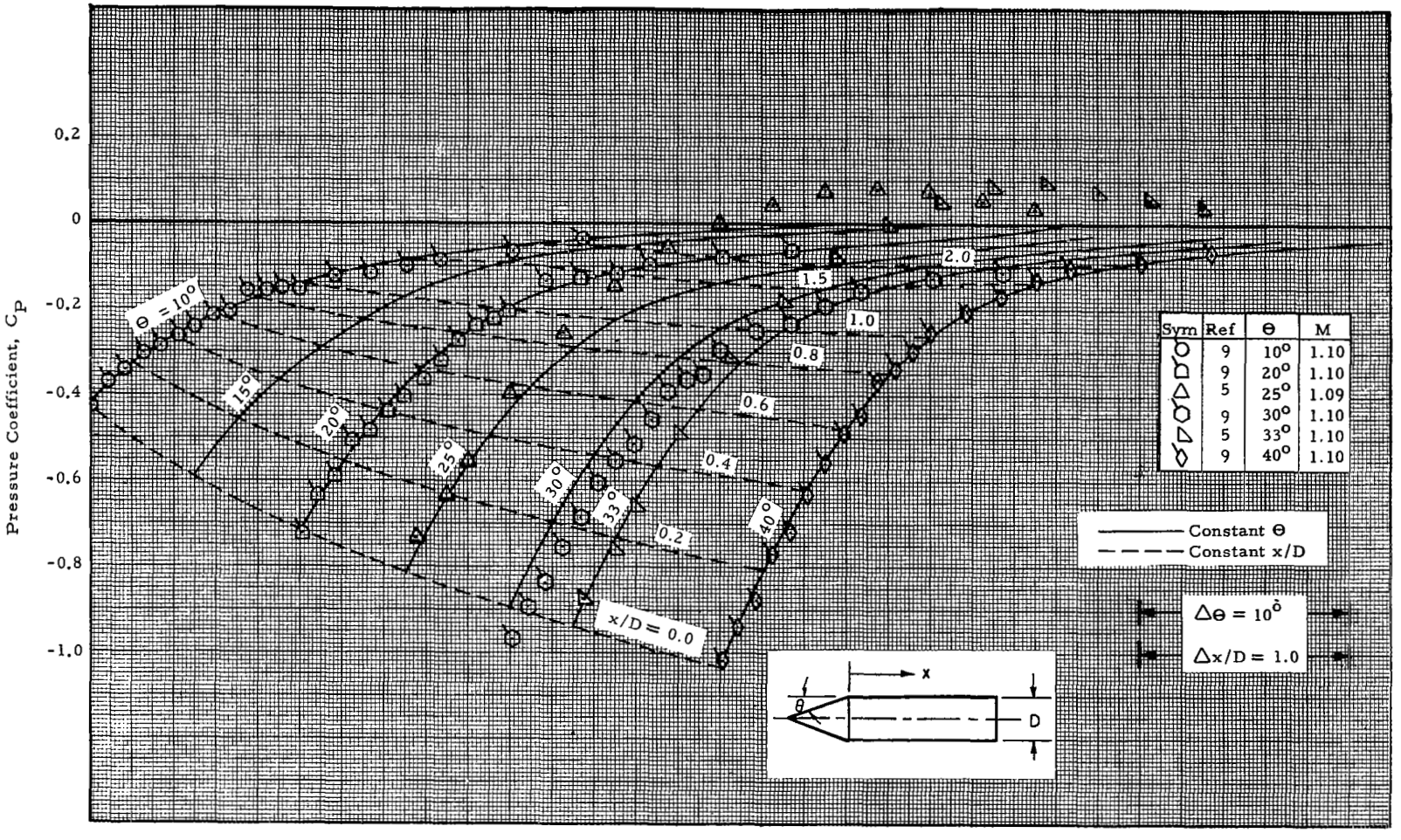

(f) M = 1.1

Figure 5 - Variation of Cylinder Surface Pressure Distributions with Cone Angle for Cone-Cylinders at Zero Angle-of-Attack (Cont'd)

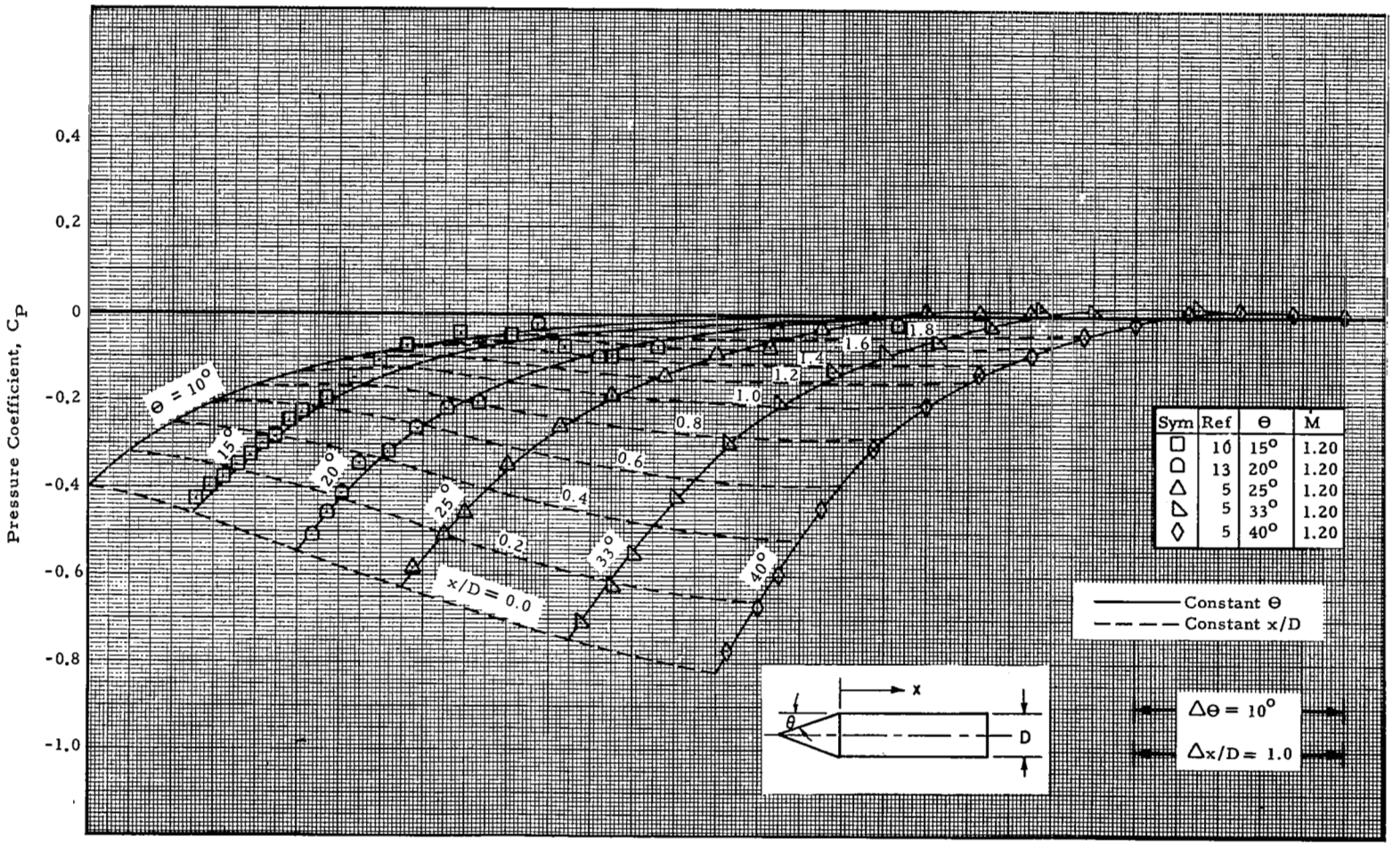

(g) M = 1.2

Figure 5 - Variation of Cylinder Surface Pressure Distributions with Cone Angle for Cone-Cylinders at Zero Angle-of-Attack (Cont'd)

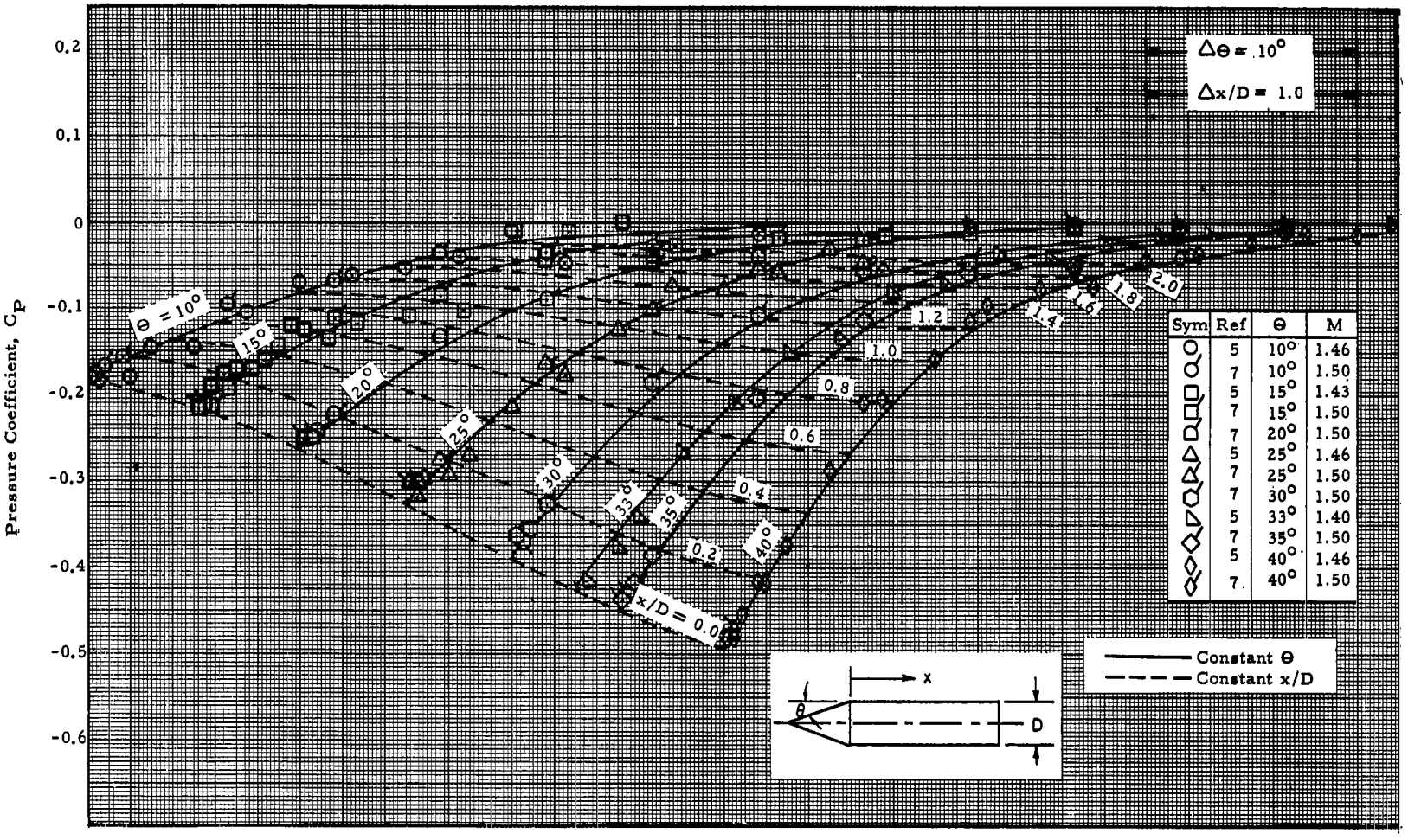

(h) M = 1.5

Figure 5 - Variation of Cylinder Surface Pressure Distributions with Cone Angle for Cone-Cylinders at Zero Angle-of-Attack (Cont'd)

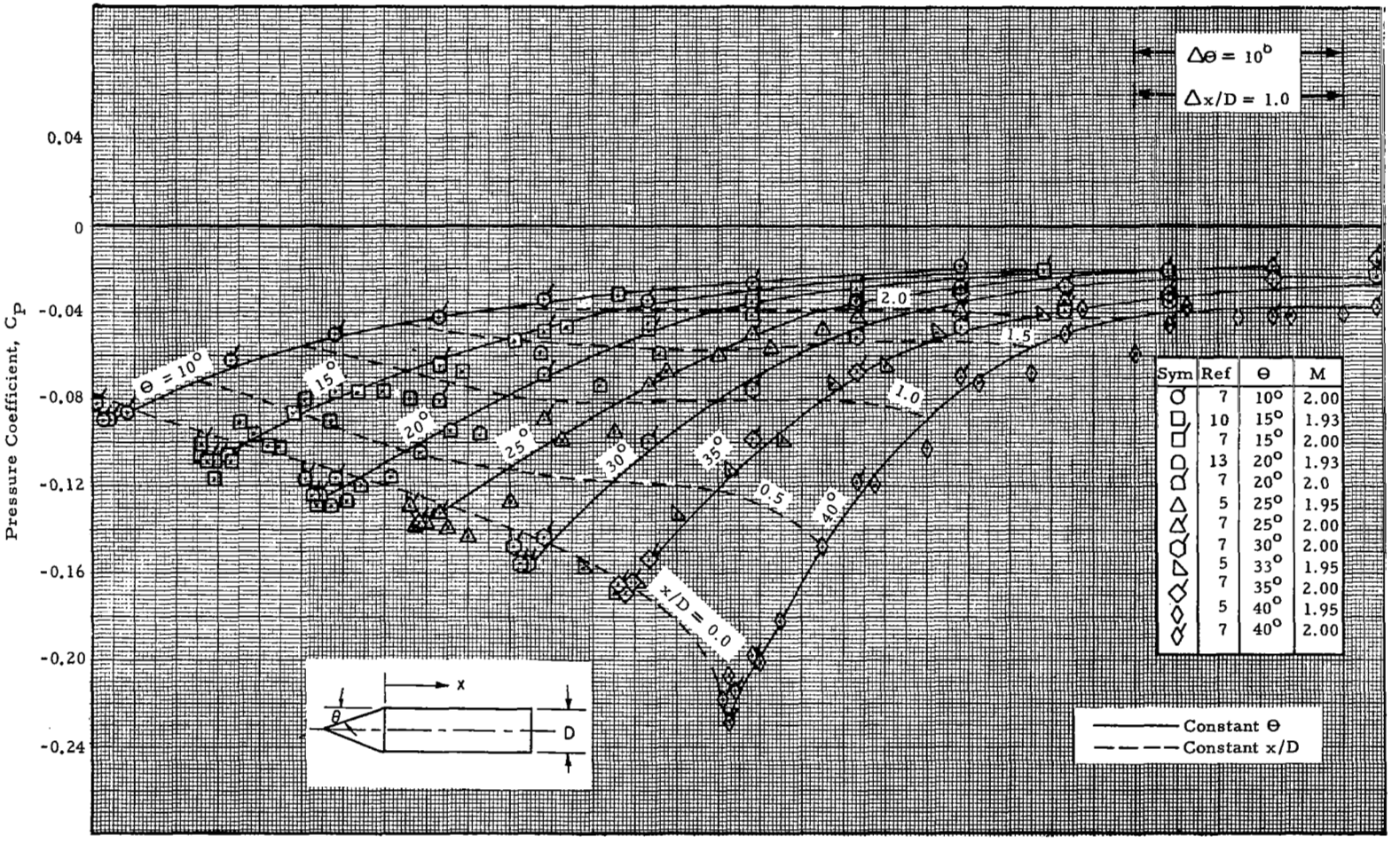

(i) M = 2.0

Figure 5 - Variation of Cylinder Surface Pressure Distributions with Cone Angle for Cone-Cylinders at Zero Angle-of-Attack (Concluded)

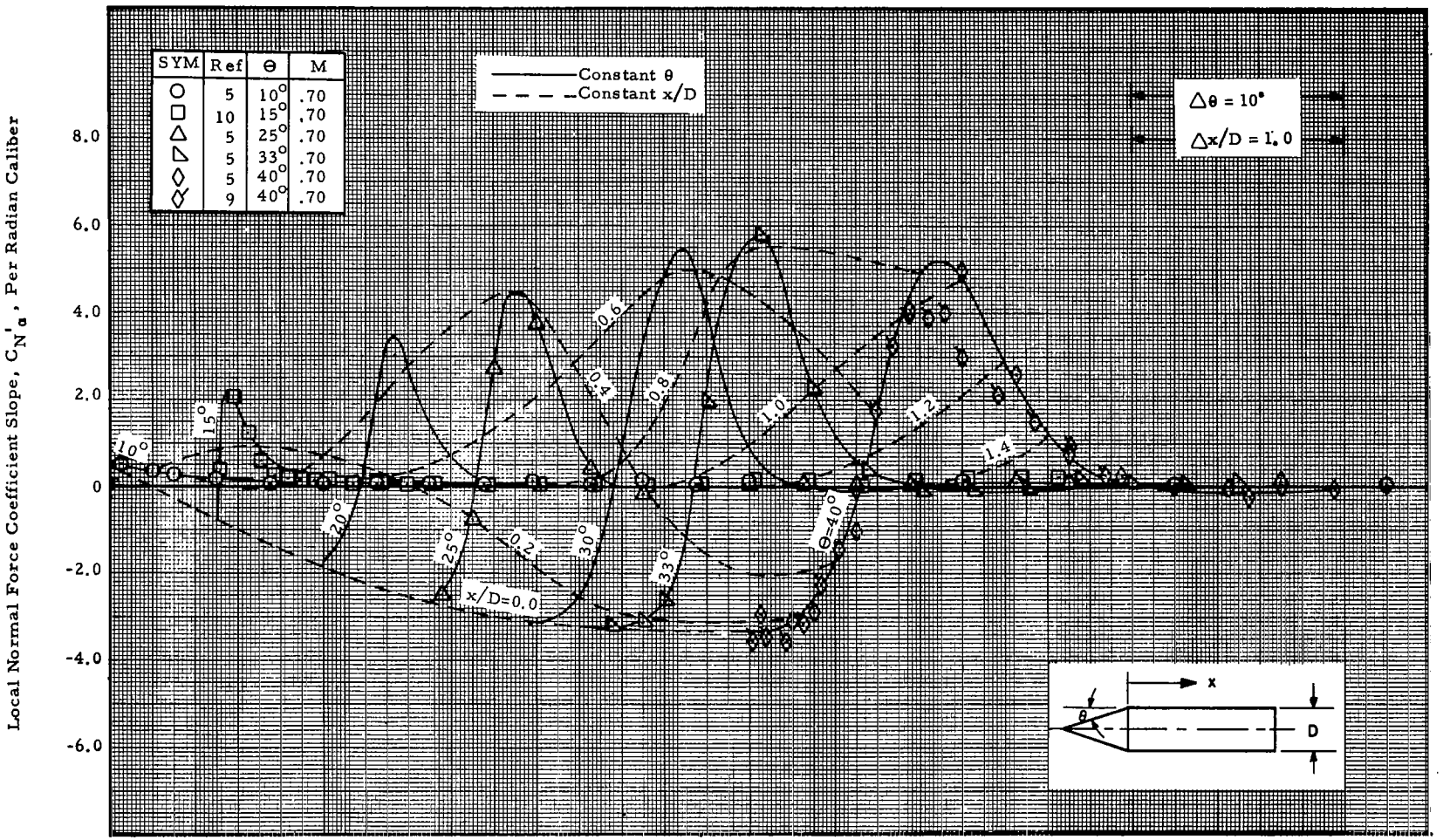

(a) M = 0.7

Figure 6 - The Effect of Cone Angle on Cylinder Local Normal Force Slope Distributions for Cone-Cylinders

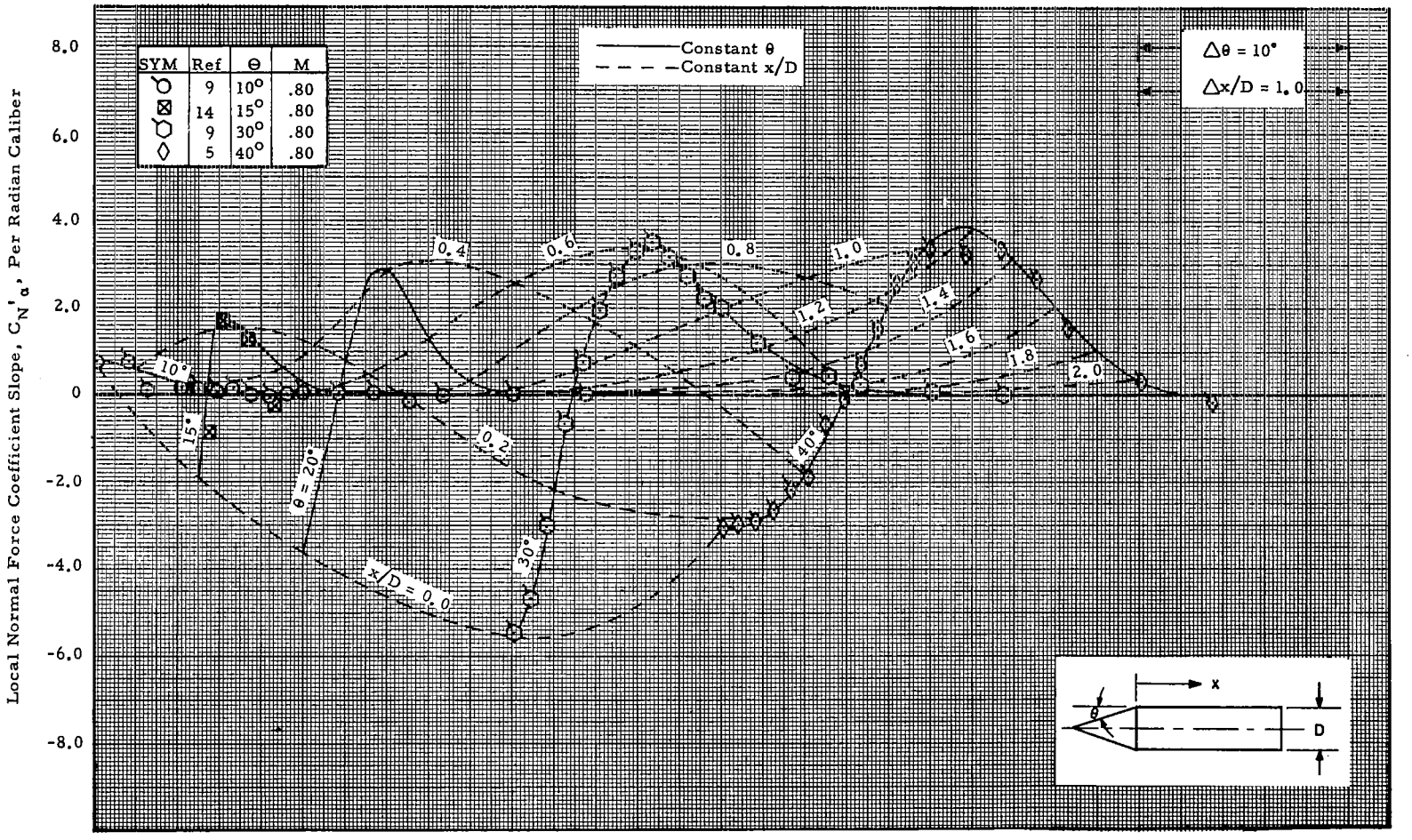

(b) M = 0.8

Figure 6 - The Effect of Cone Angle on Local Normal Force Slope Distributions for Cone-Cylinders (Cont'd)

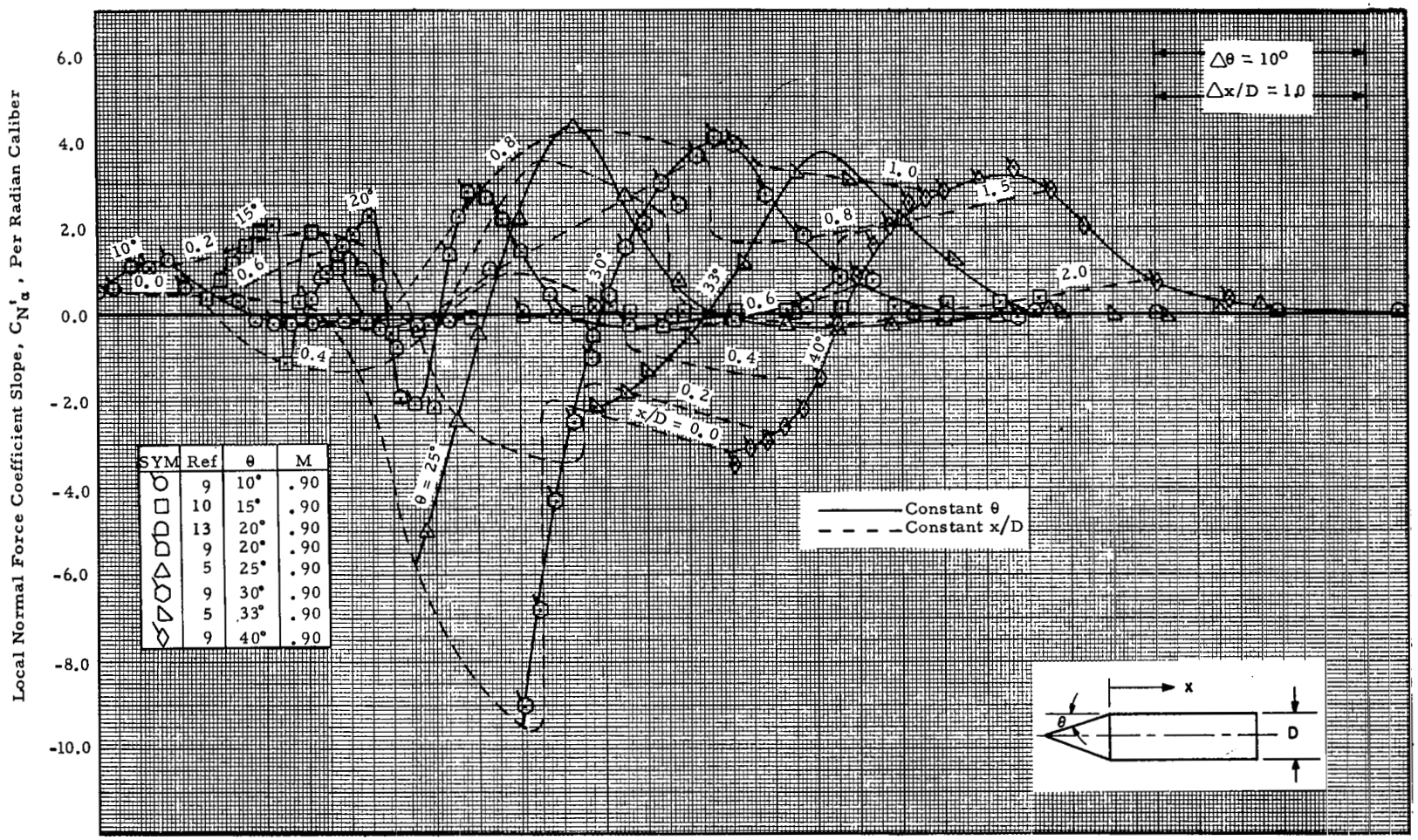

(c) M = 0.9

Figure 6 - The Effect of Cone Angle on Cylinder Local Normal Force Slope Distributions for Cone-Cylinders (Cont'd)

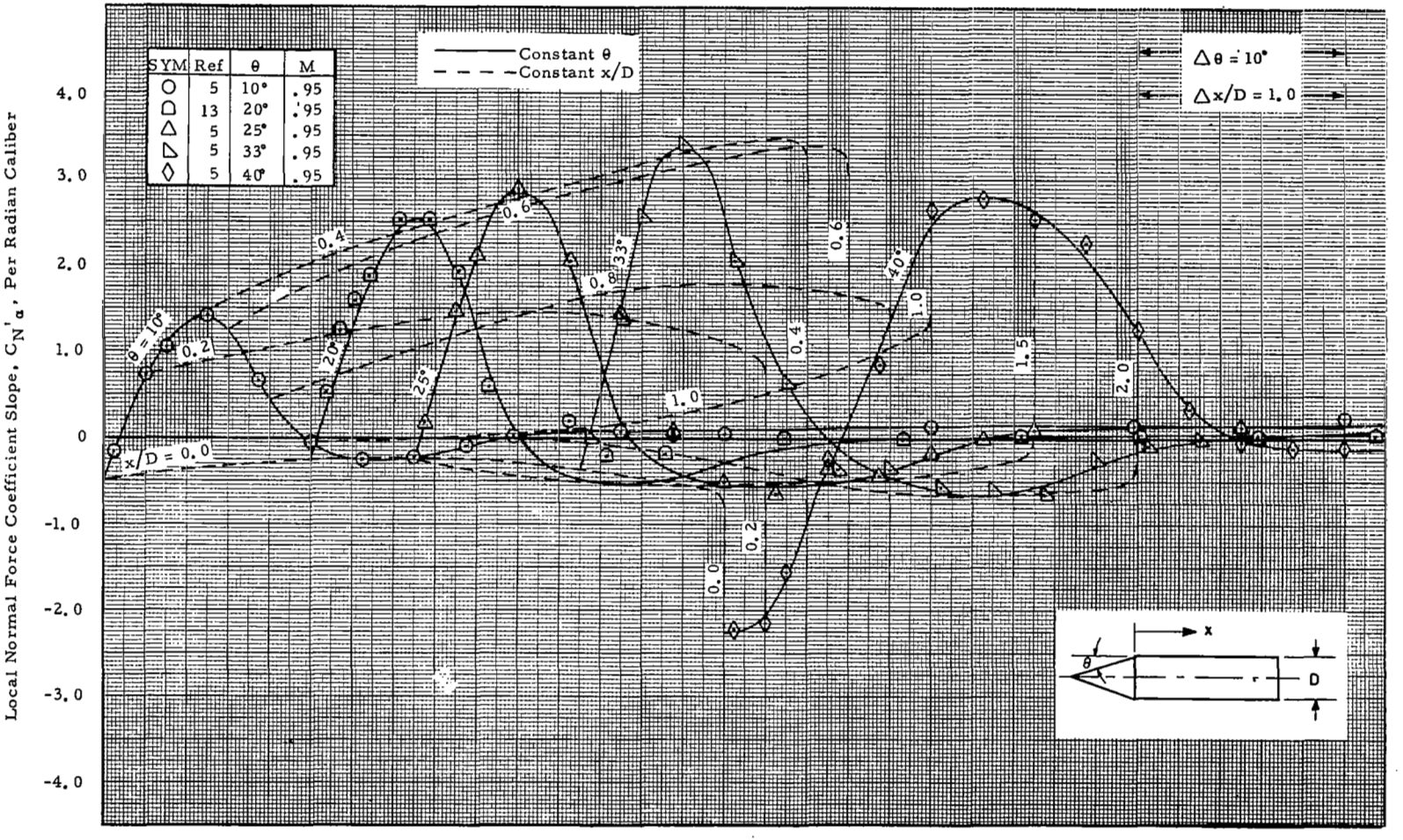

(d) M = 0.95

Figure 6 - The Effect of Cone Angle on Cylinder Local Normal Force Slope Distributions for Cone-Cylinders (Cont'd)

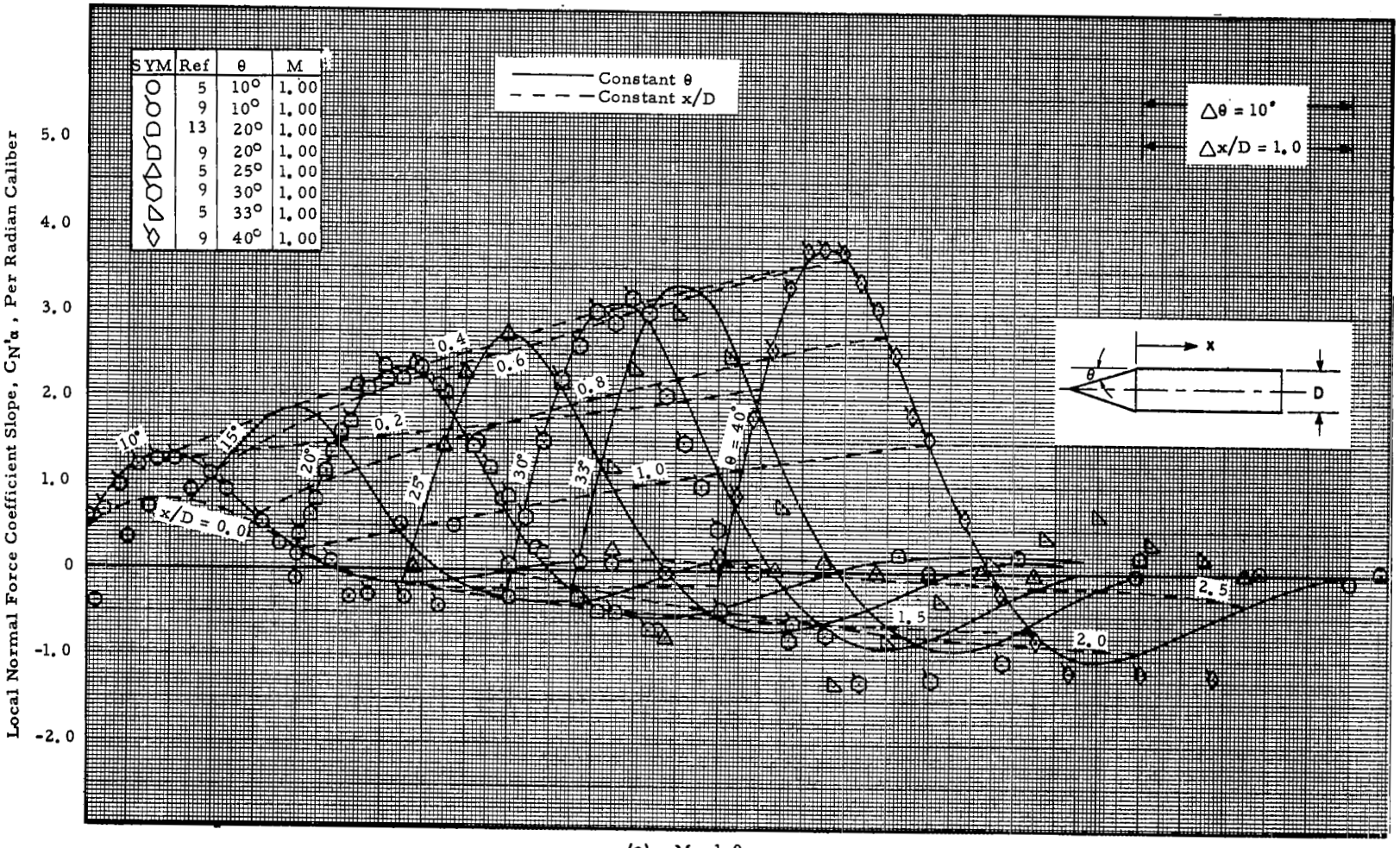

(e) M = 1.0

Figure 6 - The Effect of Cone Angle on Cylinder Local Normal Force Slope Distributions for Cone-Cylinders (Cont'd)

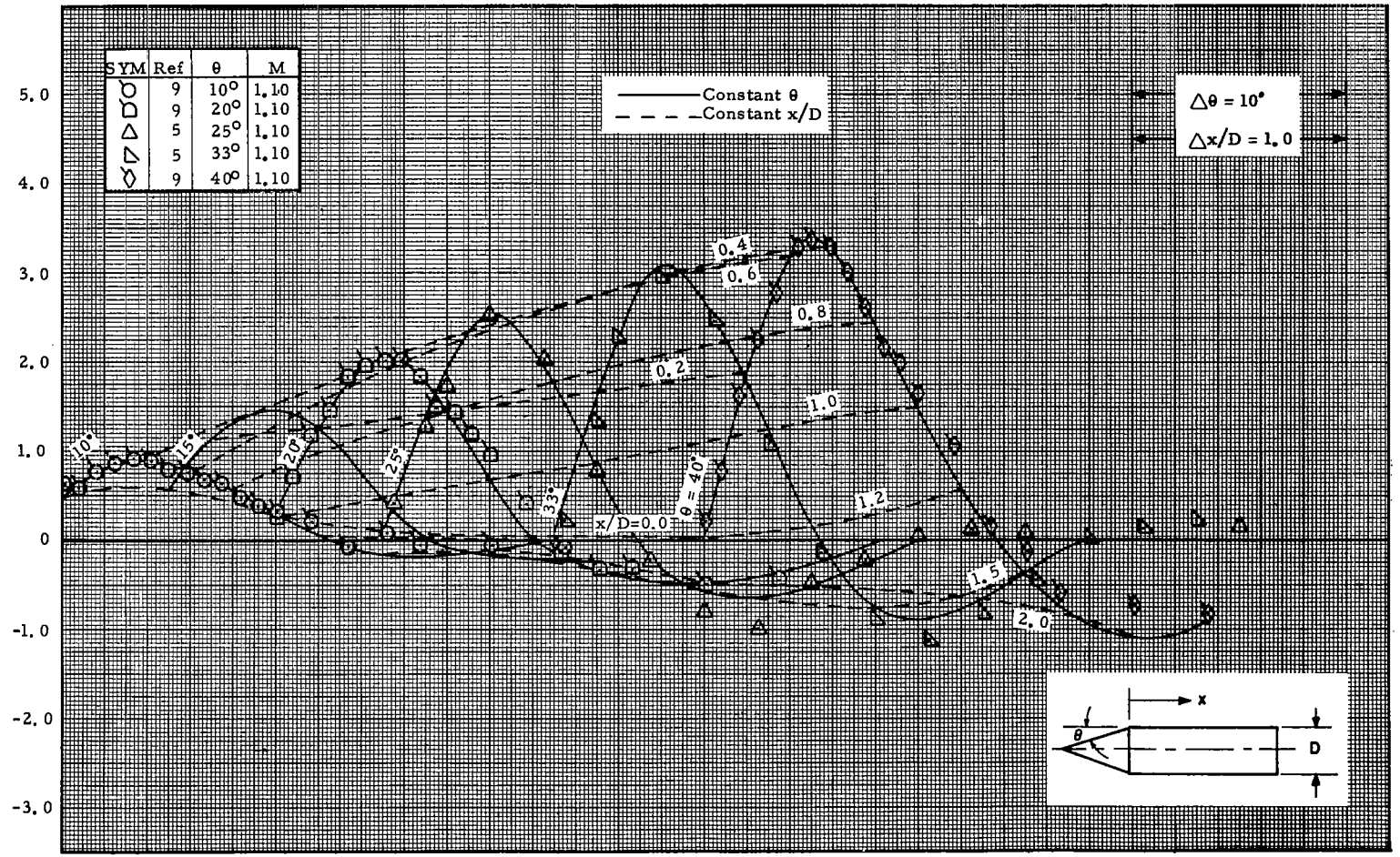

(f) M = 1.1

Figure 6 - The Effect of Cone Angle on Cylinder Local Normal Force Slope Distributions for Cone Cylinders (Cont'd)

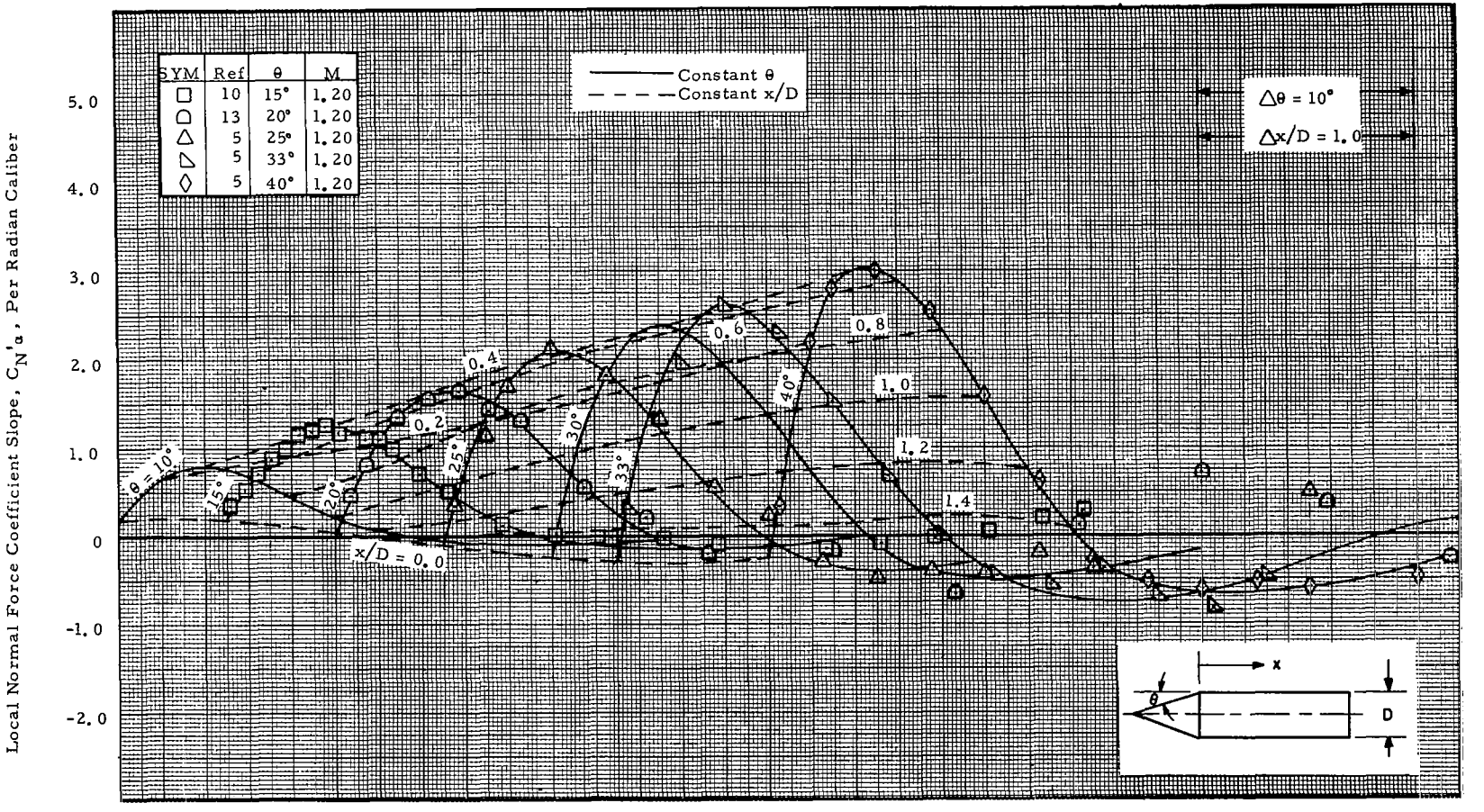

(g) M = 1.2

Figure 6 - The Effect of Cone Angle on Cylinder Local Normal Force Slope Distributions for Cone-Cylinders (Cont'd)

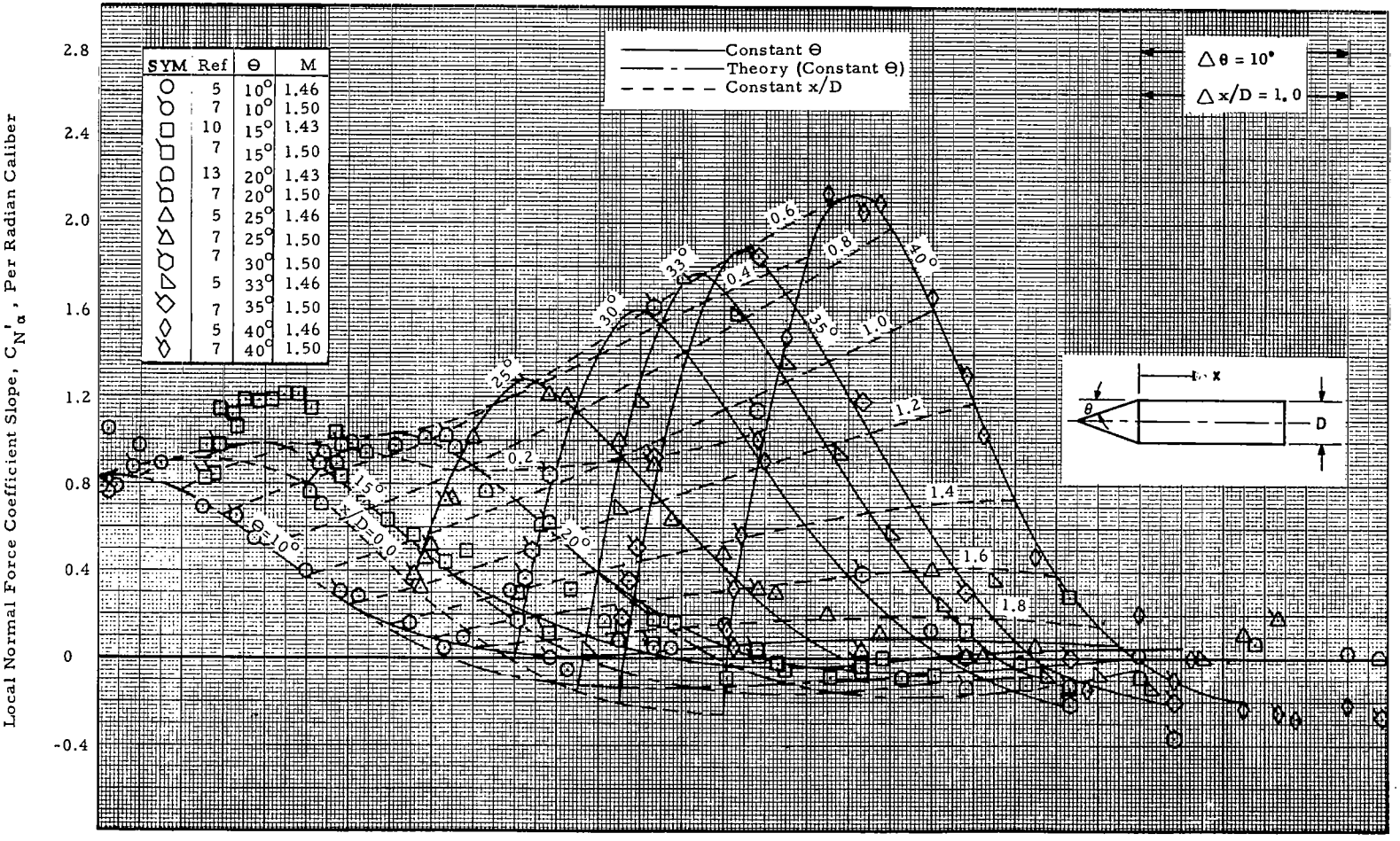

(h) M = 1.5

Figure 6 - The Effect of Cone Angle on Cylinder Local Normal Force Slope Distributions for Cone-Cylinders (Cont'd)

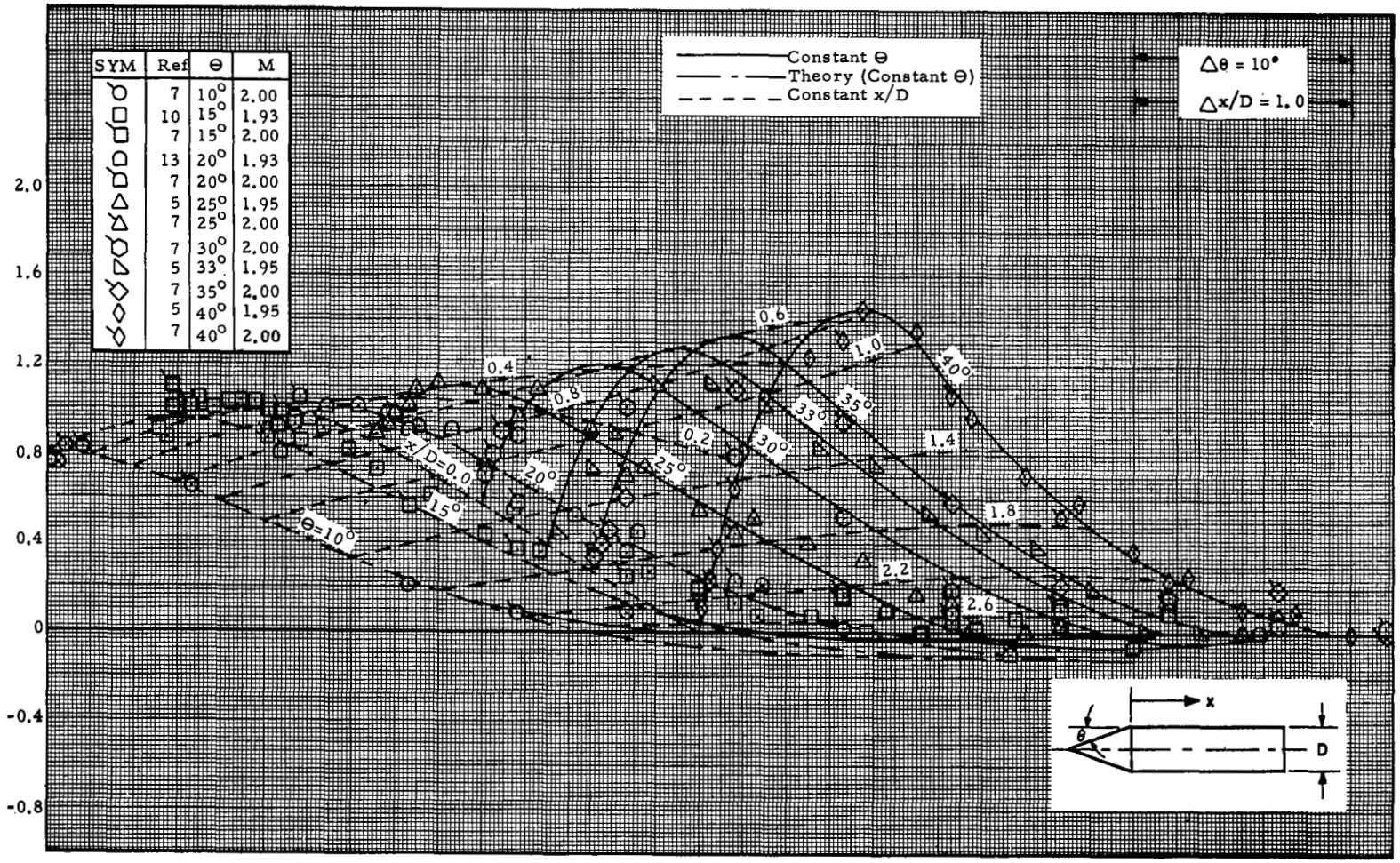

(i) M = 2.0

Figure 6 - The Effect of Cone Angle on Cylinder Local Normal Force Slope Distributions for Cone-Cylinders (Concluded)

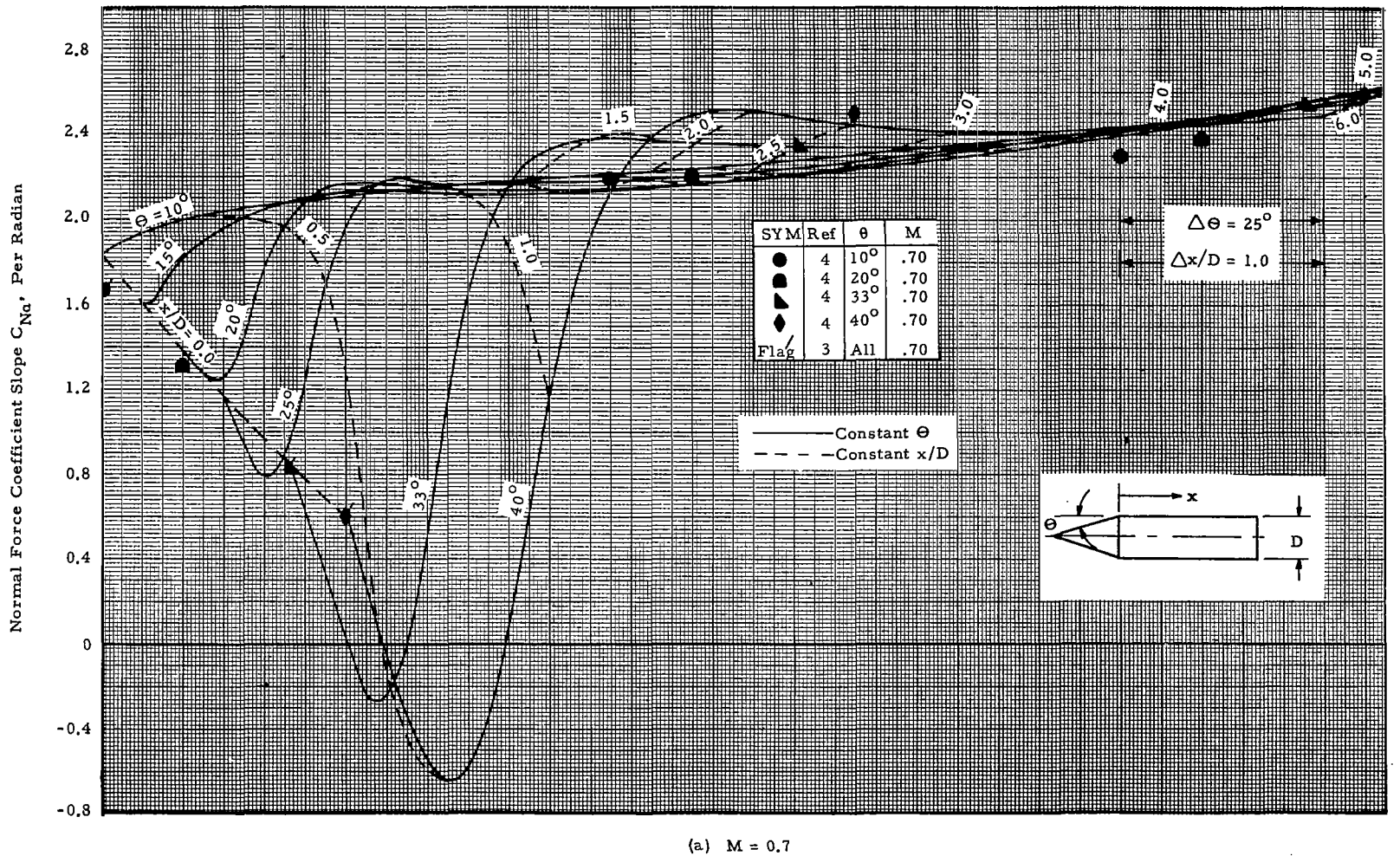

(a) M = 0.7

Figure 7 - The Effects of Cone Angle on Cylinder Normal Force Slope Buildup for Cone Cylinders

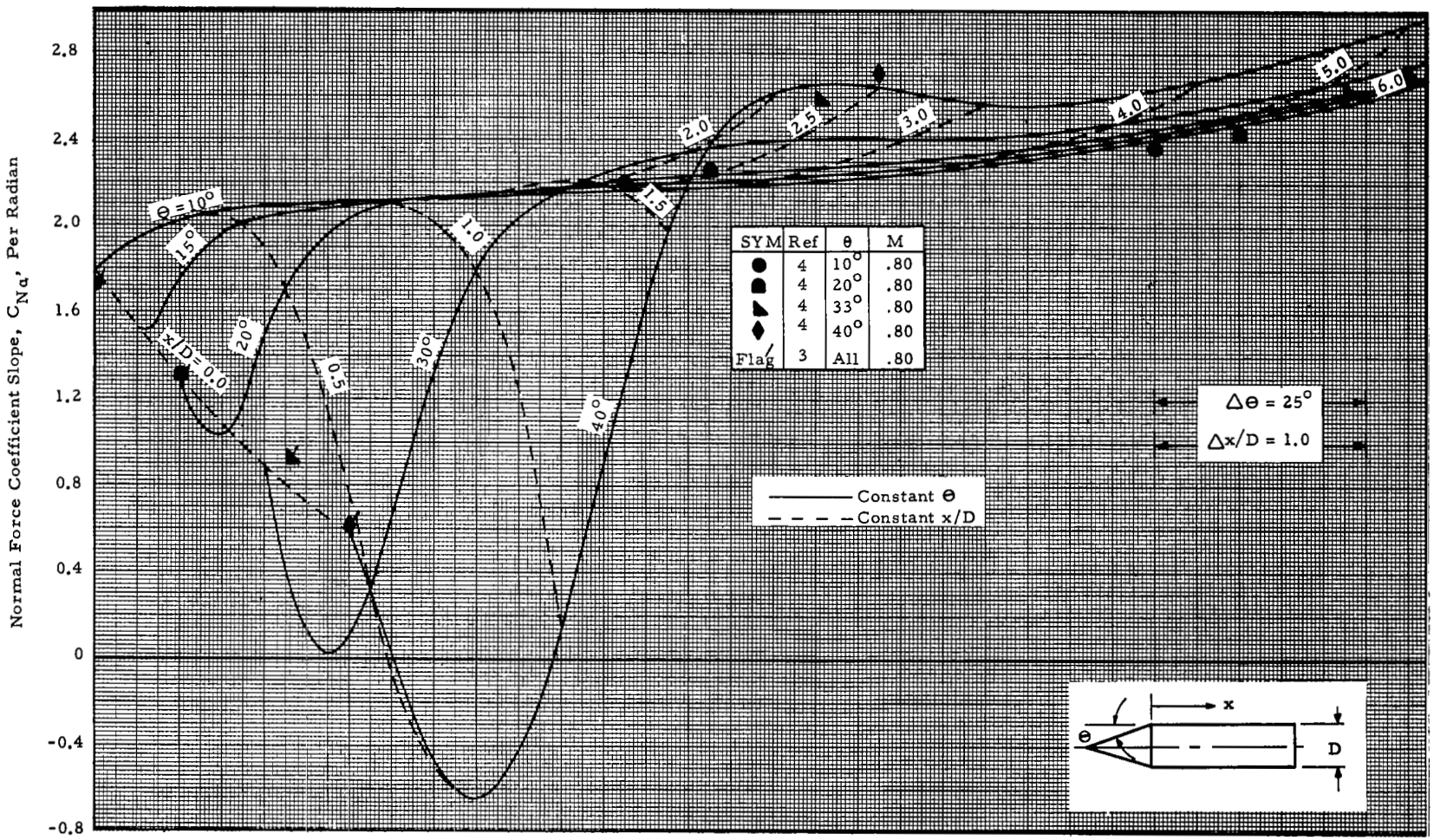

(b) $M \bar{\square} 0.8$

Figure 7 - The Effect of Cone Angle on Cylinder Normal Force Slope Buildup for Cone-Cylinders (Cont'd)

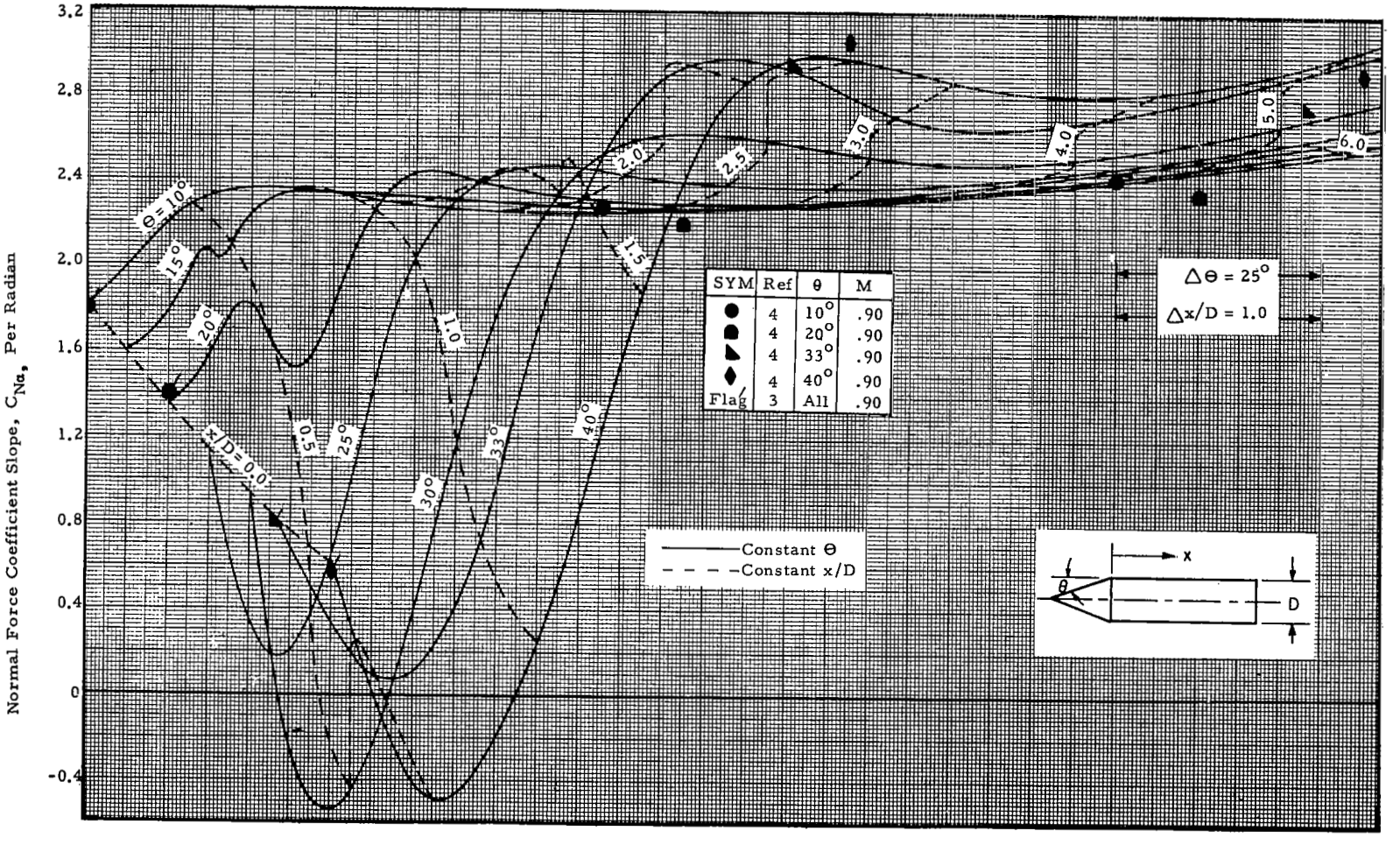

(c) M = 0.9

Figure 7 - The Effects of Cone Angle on Cylinder Normal Force Buildup for Cone-Cylinders (Cont'd)

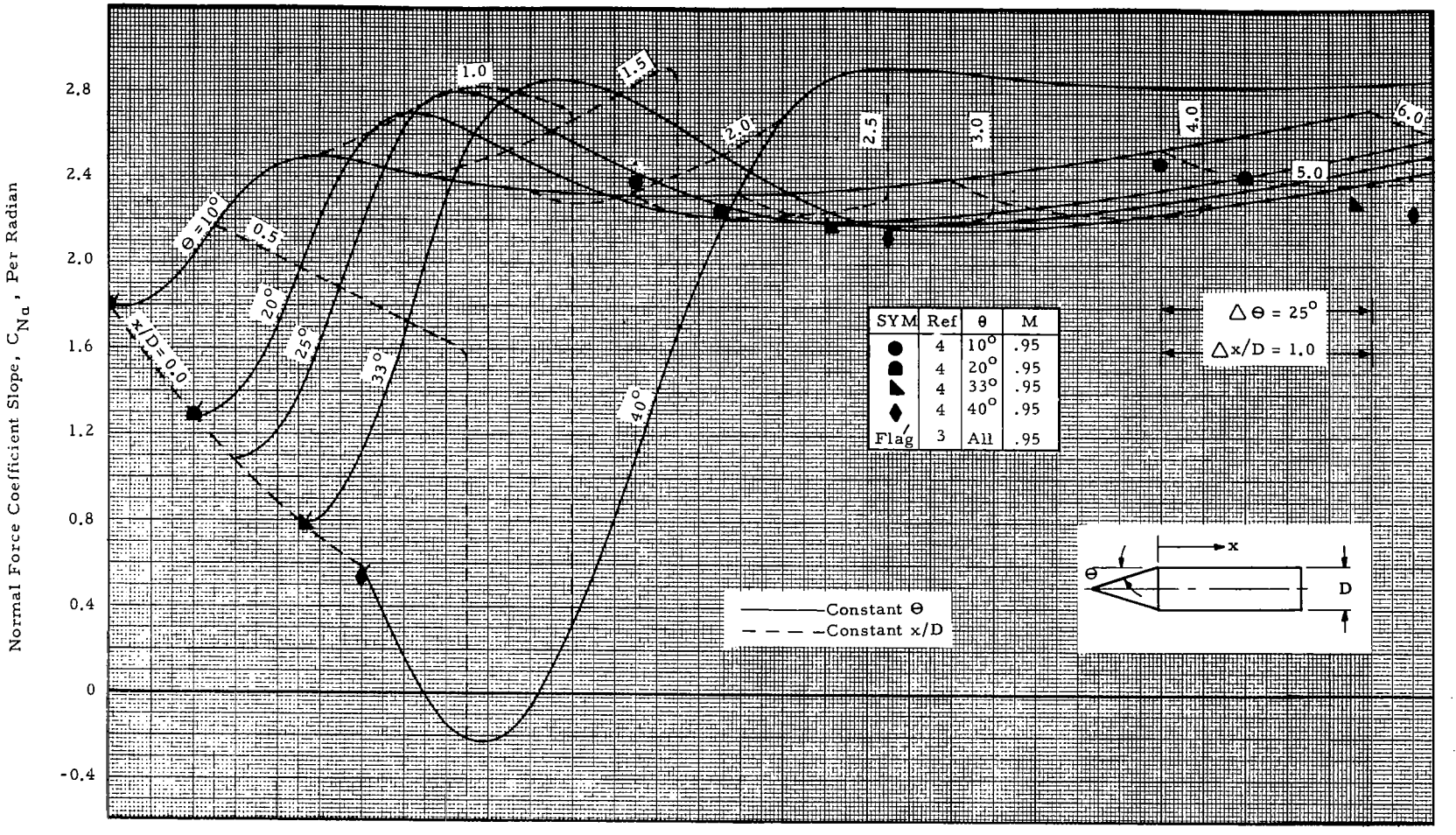

(d) M = 0.95

Figure 7 - The Effects of Cone Angle on Cylinder Normal Force Slope Buildup for Cone Cylinders (Cont'd)

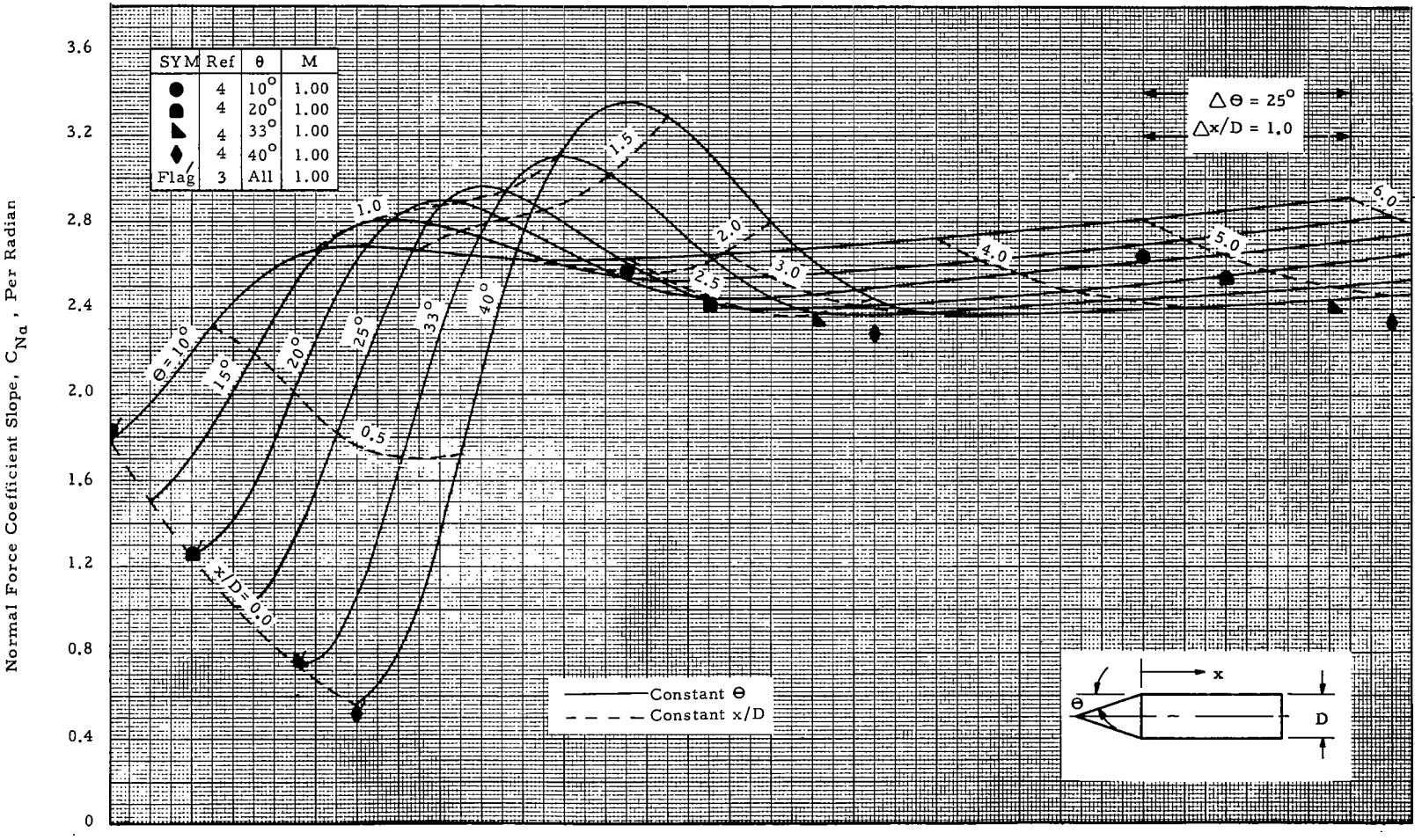

(e) M = 1.0

Figure 7 - The Effects of Cone Angle on Cylinder Normal Force Slope Buildup for Cone Cylinders (Cont'd)

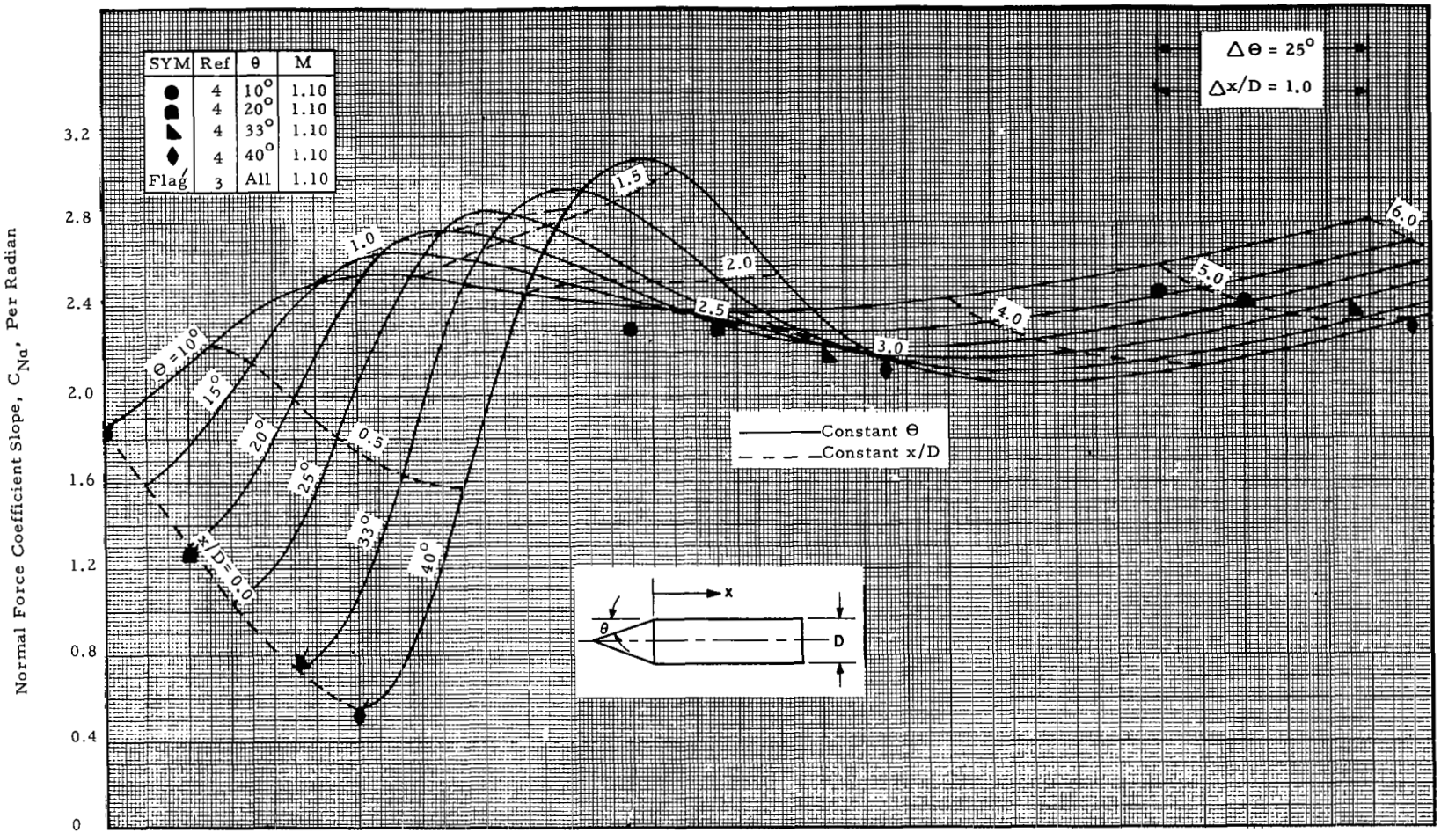

(f) M = 1.1

Figure 7 - The Effects of Cone Angle on Cylinder Normal Force Slope Buildup for Cone Cylinders (Cont'd)

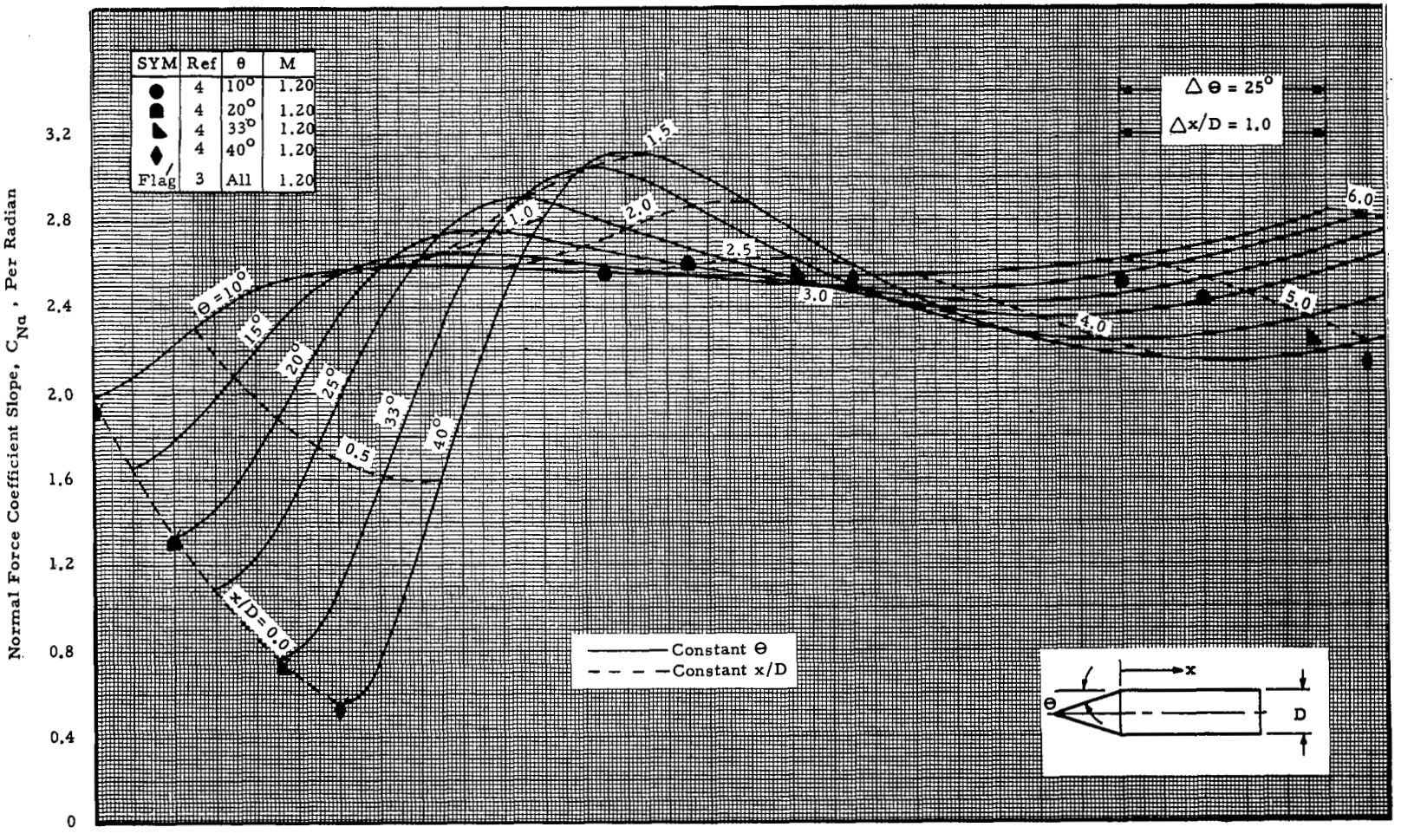

(g) M = 1.2

Figure 7 - The Effects of Cone Angle on Cylinder Normal Force Slope Buildup for Cone Cylinders (Cont'd)

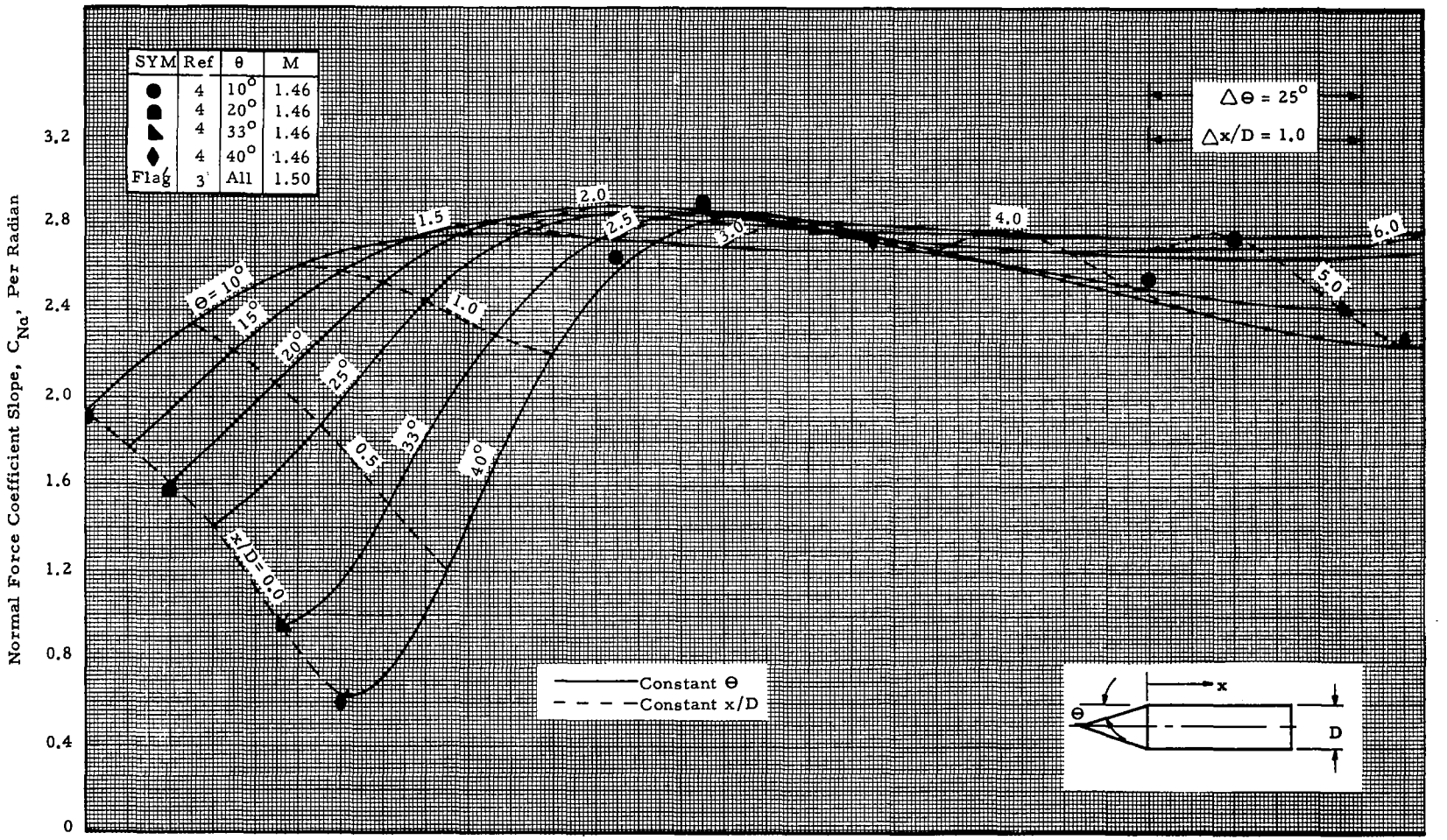

(h) M = 1.5

Figure 7 - The Effects of Cone Angle on Cylinder Normal Force Slope Buildup for Cone Cylinders (Cont'd)

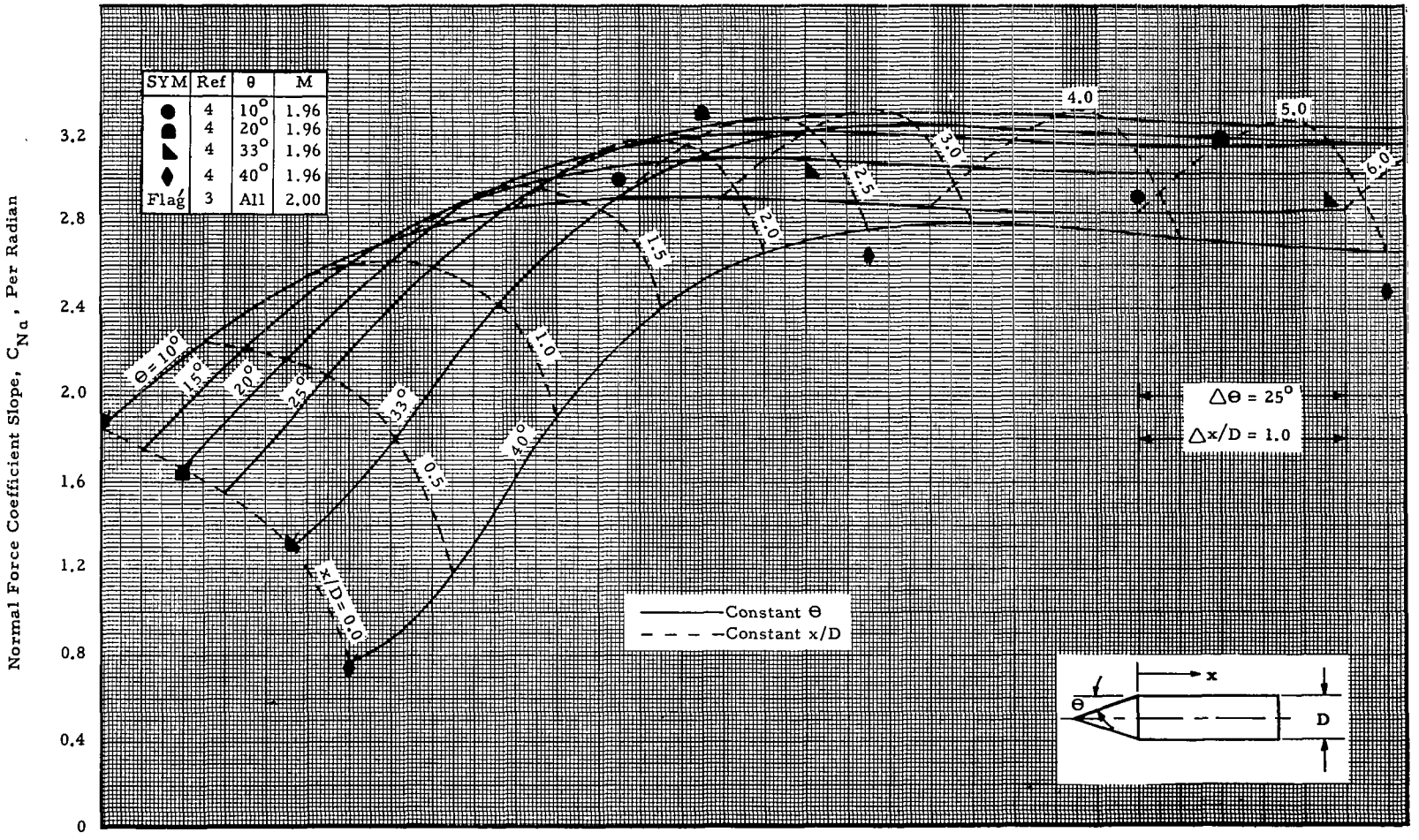

(i) M = 2.0

Figure 7 - The Effects of Cone Angle on Cylinder Normal Force Slope Buildup for Cone Cylinder (Concluded)

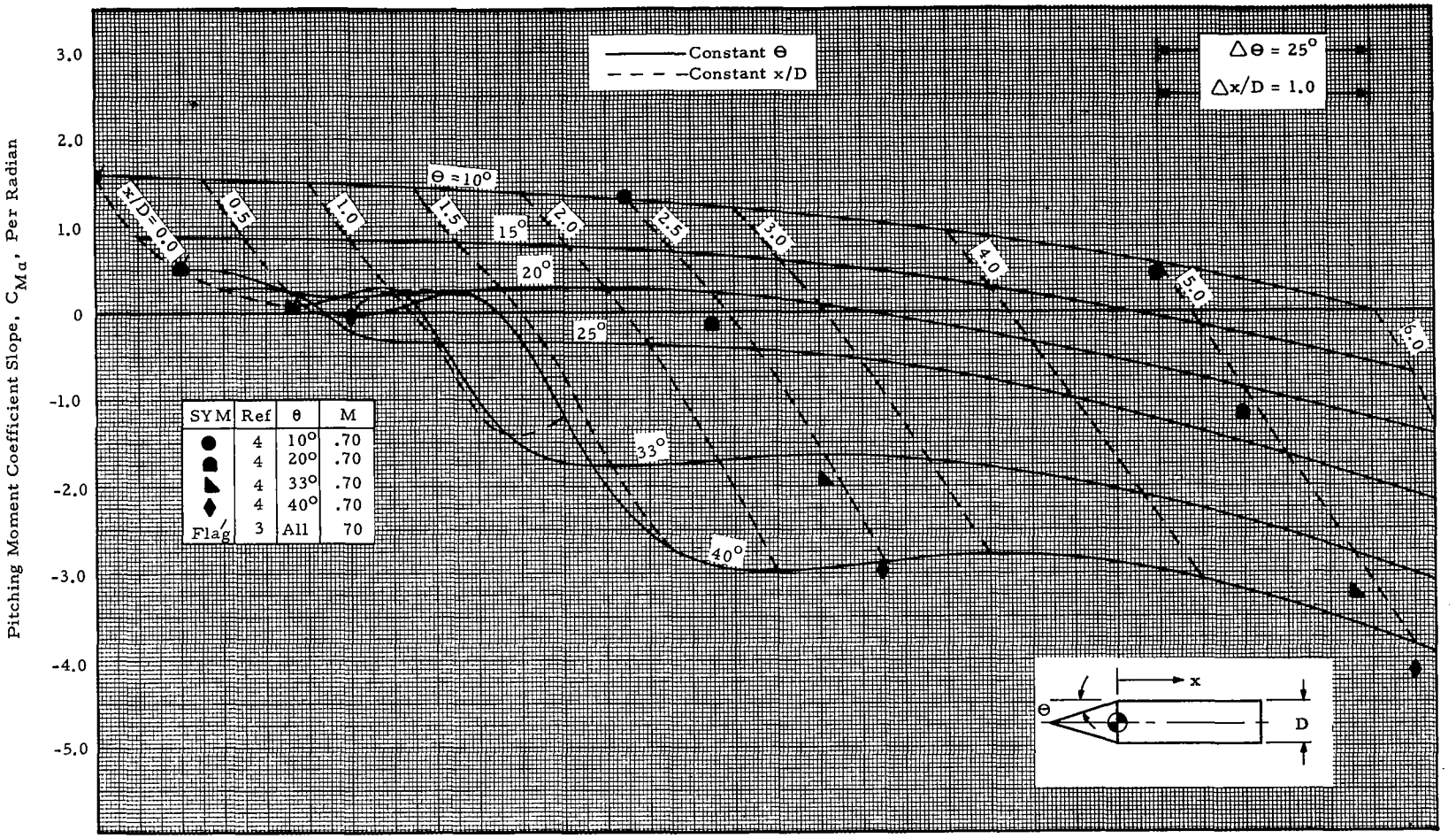

(a) M = 0.7

Figure 8 - The Effects of Cone Angle on Cylinder Pitching Moment Slope Buildup for Cone-Cylinders

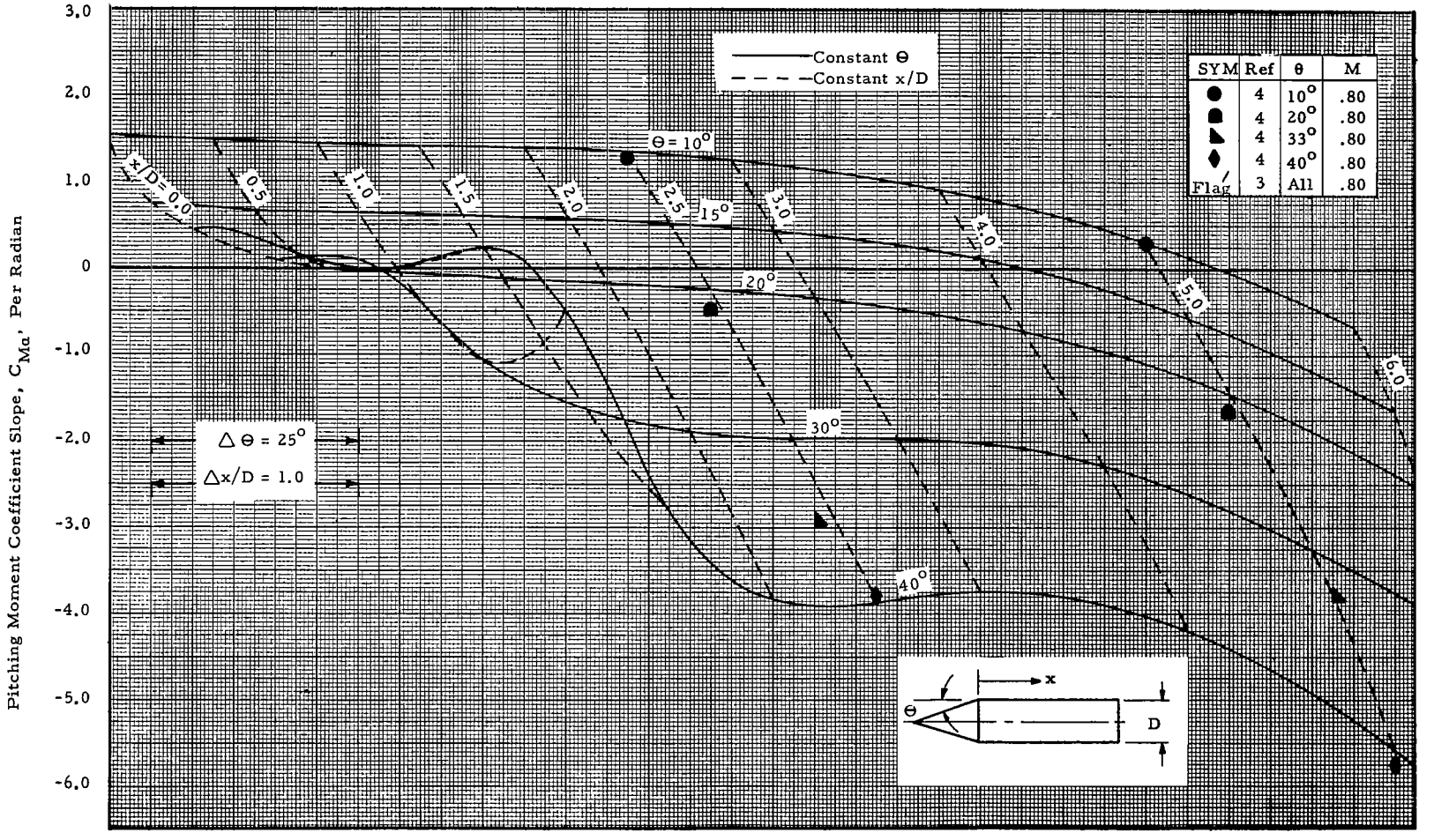

(b) M = 0.8

Figure 8 - The Effect of Cone Angle on Cylinder Pitching Moment Slope Buildup for Cone-Cylinders (Cont'd)

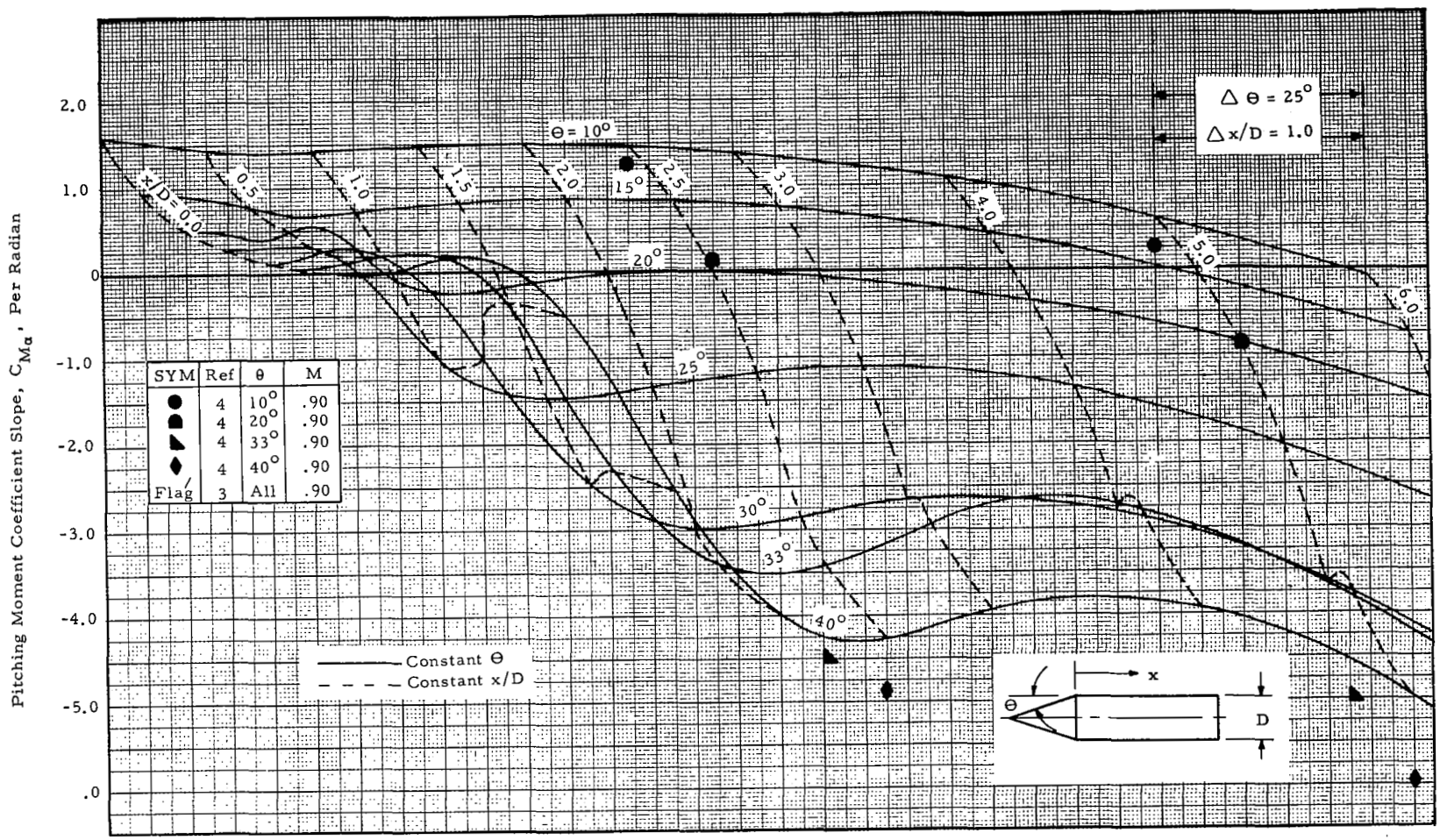

(c) M = 0.9

Figure 8 - The Effects of Cone Angle on Cylinder Pitching Moment Slope Buildup for Cone-Cylinders (Cont'd)

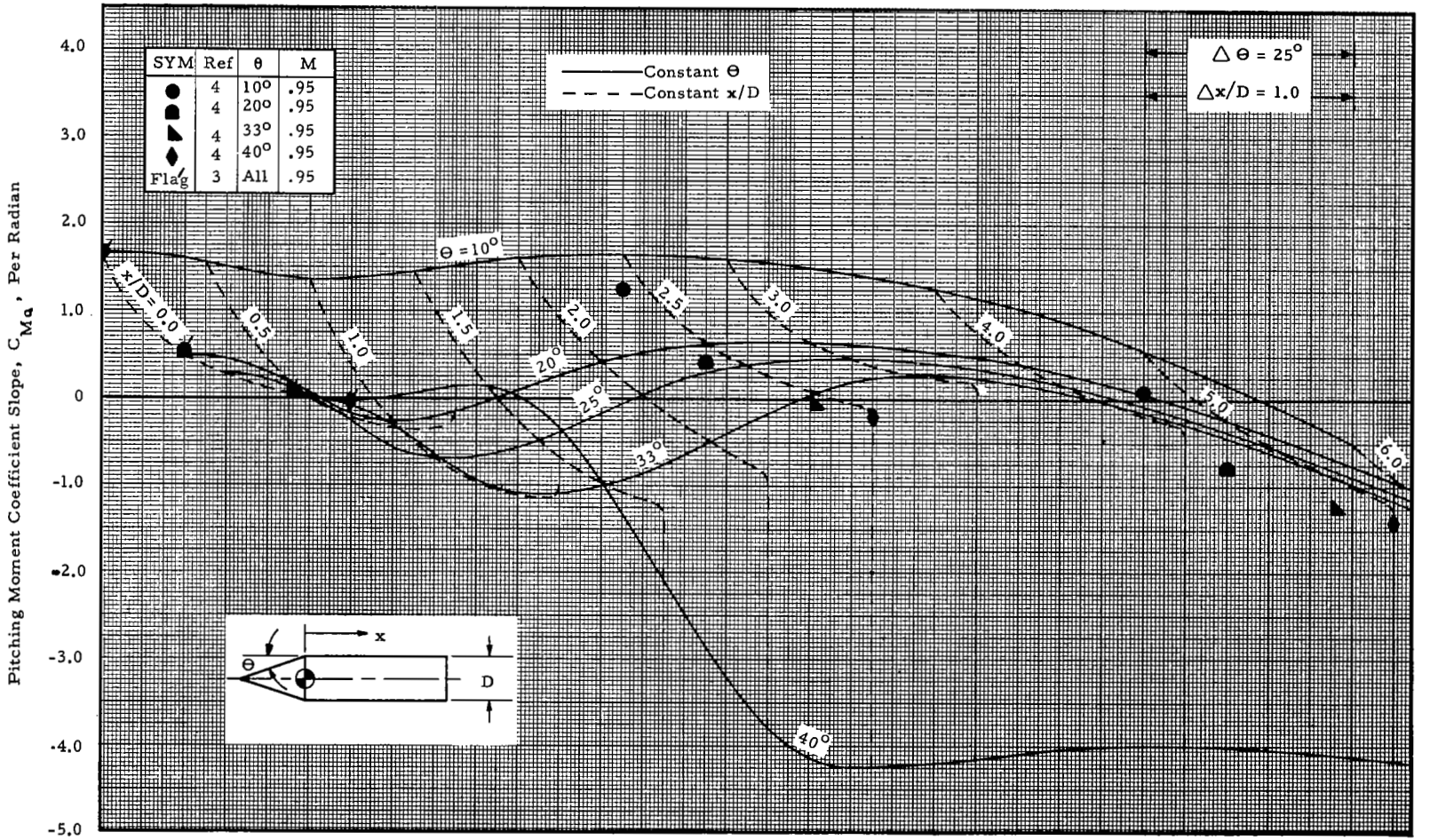

(d) M = 0.95

Figure 8 - The Effect of Cone Angle on Cylinder Pitching Moment Slope Buildup for Cone-Cylinders (Cont'd)

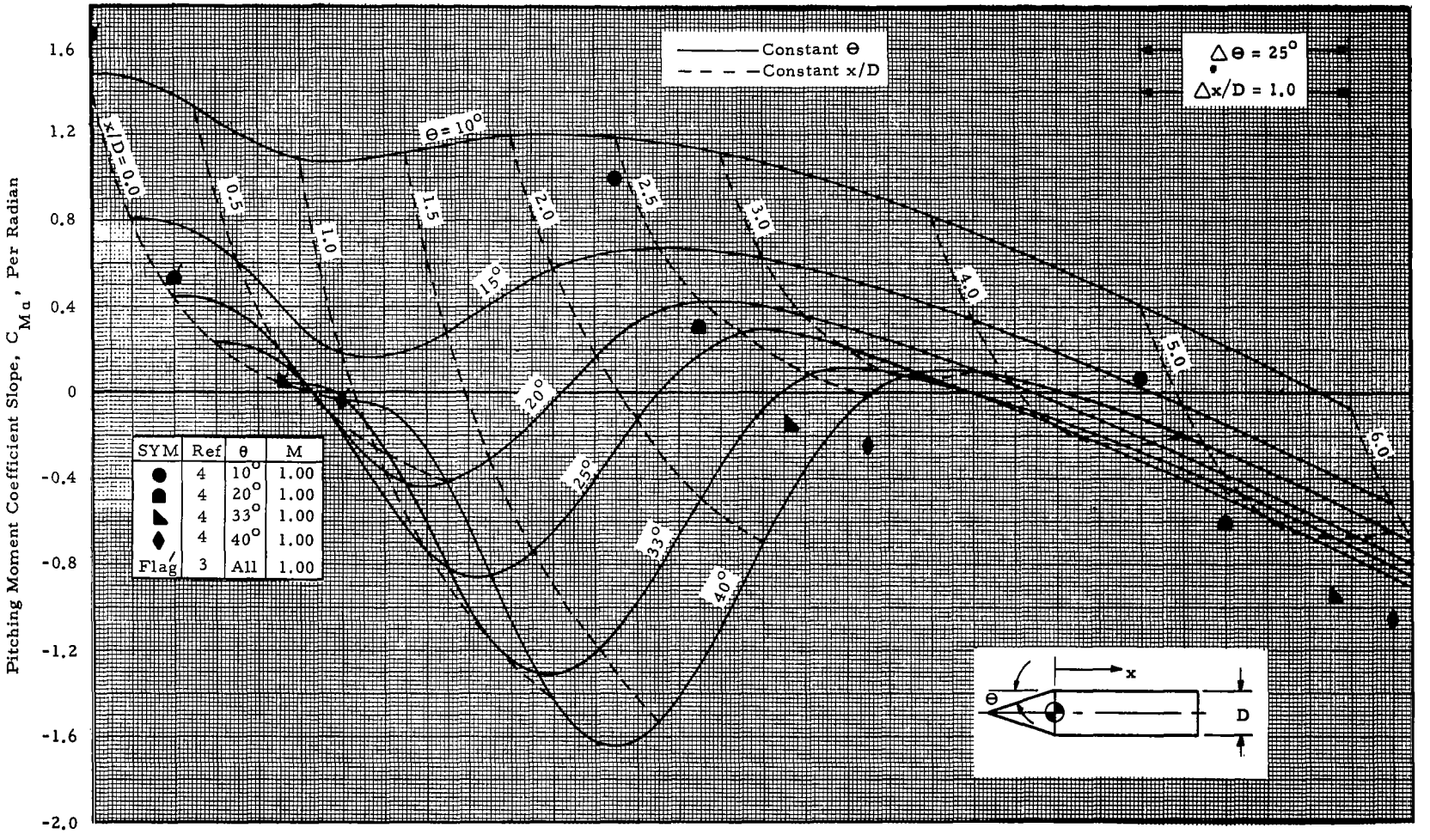

(e) M = 1.0

Figure 8 - The Effect of Cone Angle on Cylinder Pitching Moment Slope Buildup for Cone-Cylinders (Cont'd)

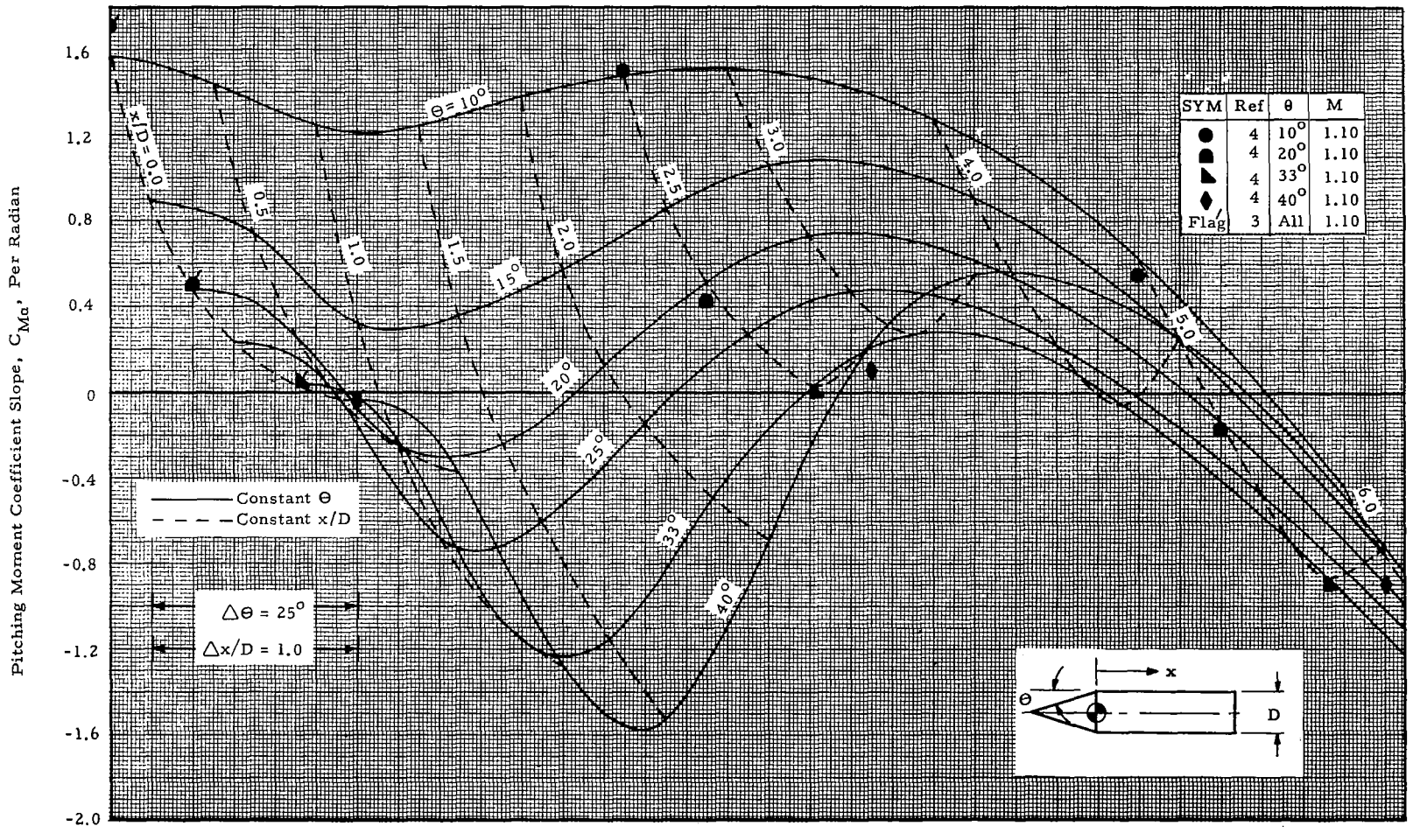

(f) M = 1.1

Figure 8 - The Effects of Cone Angle on Cylinder Pitching Moment Slope Buildup for Cone-Cylinders (Cont'd)

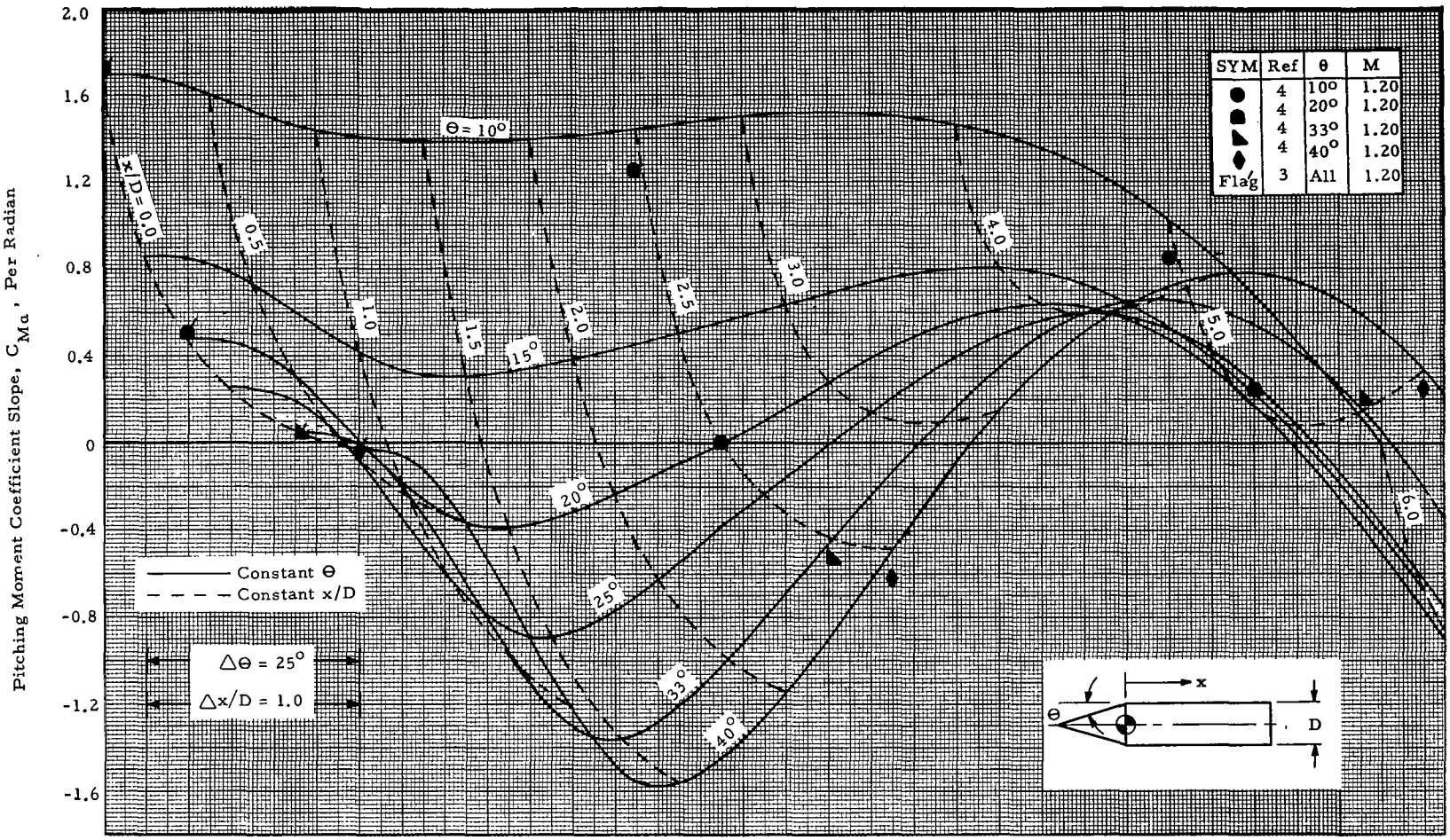

(g) M = 1.2

Figure 8 - The Effects of Cone Angle on Cylinder Pitching Moment Slope Buildup for Cone-Cylinders (Cont'd)

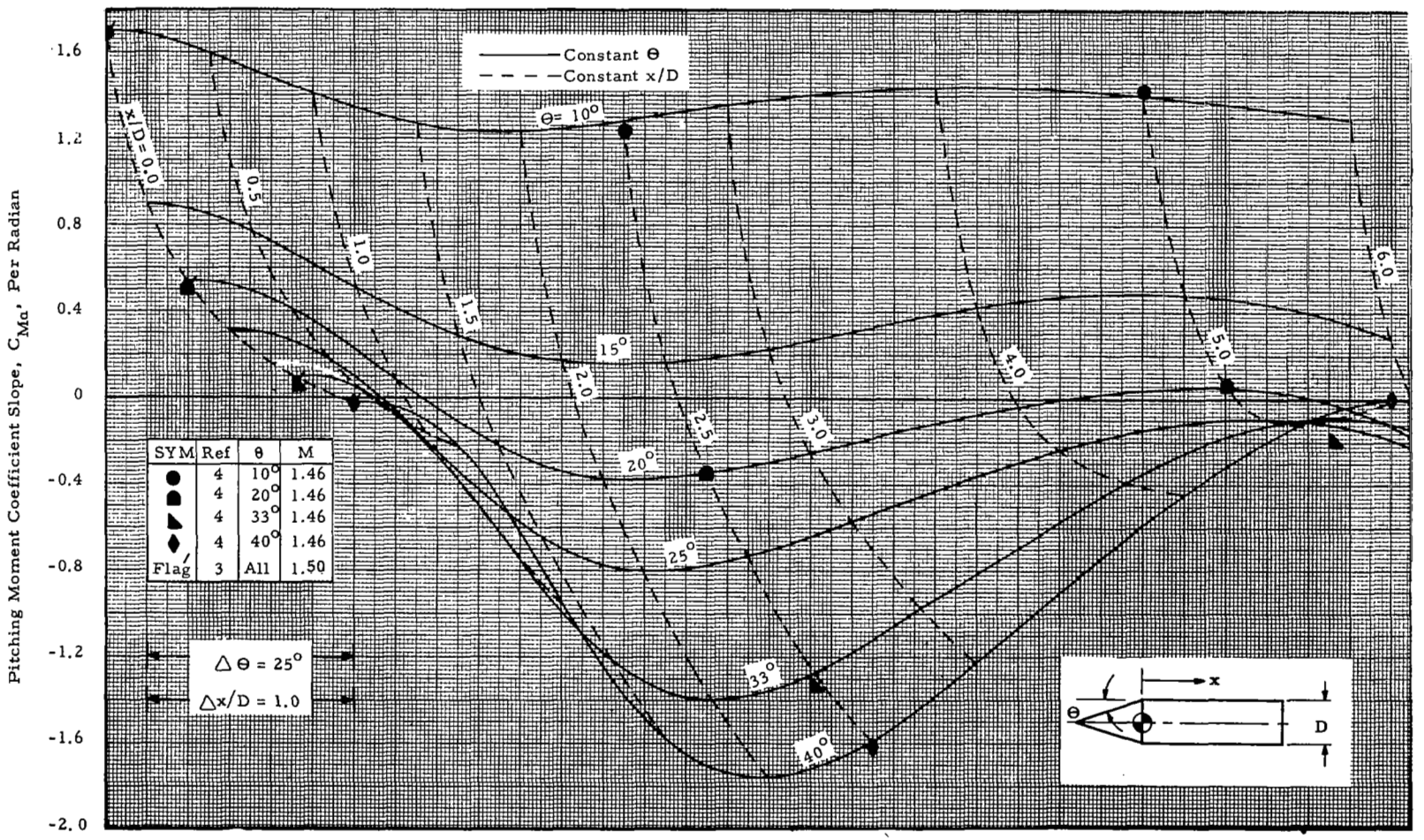

(h) M = 1.5

Figure 8 - The Effects of Cone Angle on Cylinder Pitching Moment Slope Buildup for Cone-Cylinders (Cont'd)

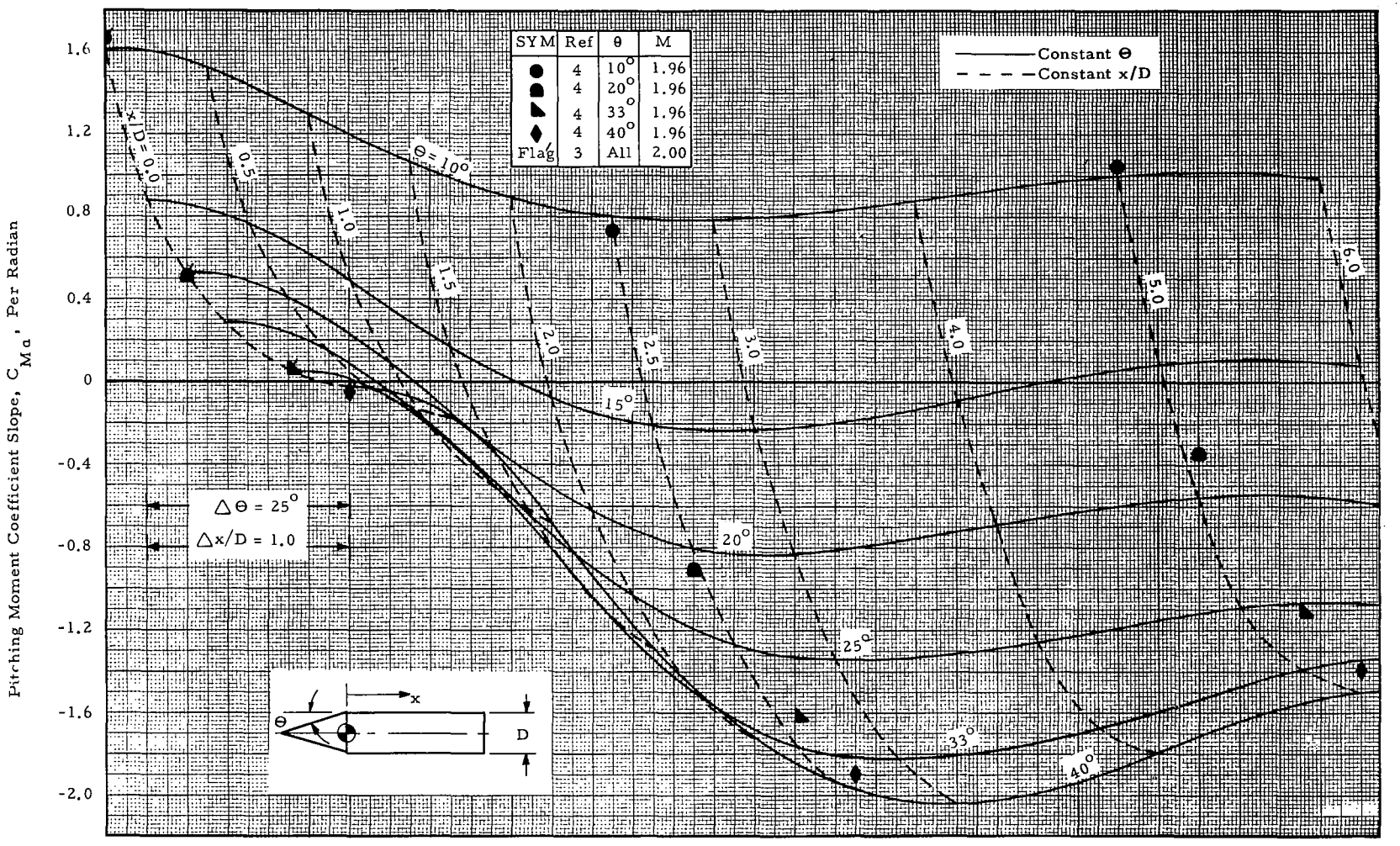

(i) M = 2.0

Figure 8 - The Effects of Cone Angle on Cylinder Pitching Moment Slope Buildup for Cone-Cylinders (Concluded)

APPENDIX A

CARPET PLOT EXPLANATION

The following explanation is included to familiarize the reader with the method of data presentation in the present report.

Suppose a parameter F is dependent upon x and y; that is,

$$F = f(x, y).$$

We introduce the parameter

$$u = k_1 x + k_2 y,$$

where k_1 and k_2 are arbitrary constants. For carpet plots, F is plotted versus u, k_1 and k_2 being suitably chosen to reflect the desired scale and relative importance of x and y. (This requires a "feel" on the part of the analyst.)

For the purpose of demonstration, let us assume that F = x-y and choose $k_1 = k_2 = 1$. We obtain

$$F = x - y, \quad u = x + y.$$

The graphical result is illustrated by Figure A-1. By holding y = 0, we arrive at F = x = u which is represented by a straight diagonal line through the origin. By allowing y to assume other constant values, a family of parallel lines is generated. Now holding x = 0 we have F = -y = -u which also is a straight diagonal line through the origin, but normal to the curve F = u. Then as x assumes other constant values, another family of parallel lines is generated.

For any pair of values for x and y, the function, F, is defined graphically by the intersection of two corresponding curves. Intermediate values may be read by constructing additional curves; in practice, this can be done by connecting corresponding points on each curve. It can be seen that for reading purposes, the horizontal scale may be omitted. Furthermore, it is obvious that either x or y varies linearly in the horizontal direction as

opposed to a linear variation along the curve. (In this example, both are linear.)

It can be noted here that a choice of k_1 different from k_2 would have generated two families of lines not perpendicular. Also, it should be mentioned that the choice of a function F different from the simple linear case chosen would have yielded two families of curves neither straight nor parallel (in the general sense).

As a more practical example, consider Figure 3a of the main report. Pressure coefficient, C_p, is plotted as a function of cone angle, θ, and station. Along any solid line station varies, but cone angle is held constant. To illustrate, along the curve for $\theta = 30^o$ as one moves from the point, $x/L_1 = 0.6$ to the point $x/L_1 = 0.8$, he traverses 2.0 centimeters in the lateral direction. This corresponds to a station increment of 0.5. Conversely, as one moves along the curve for $x/L_1 = 0.6$ from the point $\theta = 25^o$ to the point $\theta = 30^o$, he traverses 2.5 centimeters in the lateral direction, corresponding to a cone angle increment of 5^o.

For any pair of values for θ and x/L_1, a point on the graph is defined from which a C_p value may be read. For example, at $\theta = 30^o$ and $x/L_1 = 0.6$, C_p is read as 0.36 opposite the point of intersection of the two corresponding curves. For a station of 0.7 and $\theta = 30^o$, one moves along the curve $\theta = 30^o$ to the right a lateral distance of one centimeter. The C_p value at that point is 0.277. If this procedure is followed for each constant θ curve, there is found a C_p value on each curve at $x/L_1 = 0.6$. A faired curve connecting these points then produces a $x/L_1 = 0.6$ curve along which intermediate values for θ can be located. Similarly, a point for any combination of θ and x/L_1 can be located, and C_p subsequently determined.

There are three main advantages in employing the carpet plots:

1. Correlation is possible with scattered points where two parameters are allowed to vary.
2. Nonlinear interpolation of curves can be achieved directly from the graphs presented.
3. It results in a minimum of data plots adequate for satisfactory presentation.

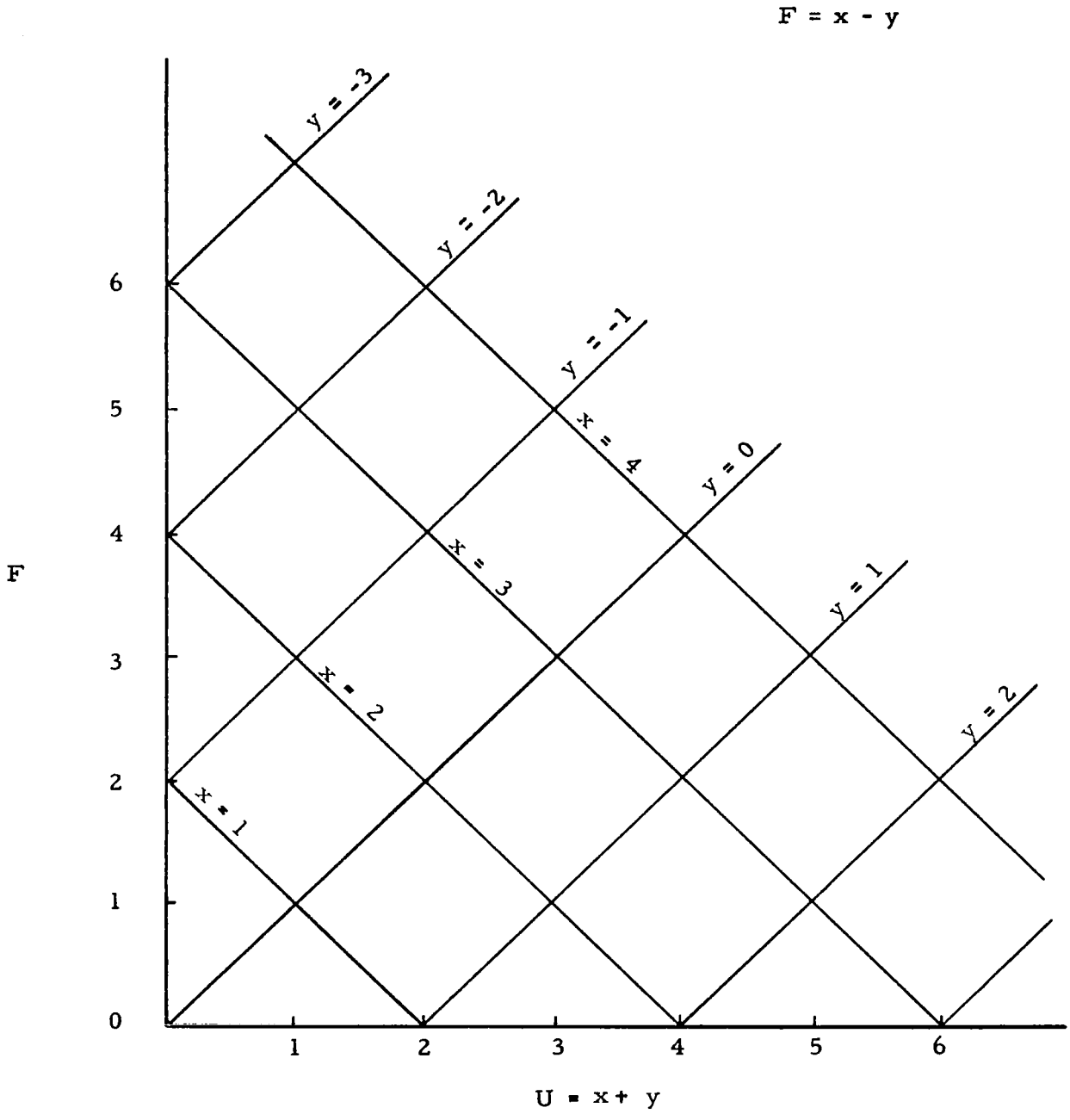

Figure A-1 - An Example Carpet Plot